Breaching of Concrete Masonry Unit Walls due to Direct Shear when Subjected to Blast Loading

by

Daniel Glenn Brannon

A master's thesis submitted to the Graduate Faculty of
Auburn University
in partial fulfillment of the
requirements for the Degree of
Master's of Science

Auburn, Alabama
May 7, 2011

Keywords: concrete masonry units, direct shear, partially grouted
finite element modeling, breaching shear, quasi-static, LS-DYNA

Approved by

James S. Davidson, Chair, Associate Professor of Civil Engineering
Robert W. Barnes, James J. Mallett Associate Professor of Civil Engineering
Justin D. Marshall, Assistant Professor of Civil Engineering

Abstract

This report details the steps needed to formulate an engineering design equation to address the potential for breaching of concrete masonry walls in between grout cells when subjected to blast loading. Prior to the beginning of this research effort, large-scale dynamic tests were performed by Air Force Research Laboratory. These tests were used to verify finite element models created using LS-DYNA. A comparisons of finite element models and testing were performed to help verify the finite element model analysis. A short suitability study was carried out to understand the cause of the breaching shear in concrete masonry walls. Two analytical models were created to provide an understanding of the mechanics of the breaching. A comparison of the FEM and analytical models were carried out. Finally, a design shear equation was formulated, and a maximum pressure for partially grouted construction was found.

Acknowledgments

I would like to thank Dr. James Davidson at Auburn University for taking me on as a research assistant and for providing funding for furthering my education; he also provided technical and professional advising, as well as, focusing my research efforts. I would like to acknowledge the efforts of the researchers in the Air Force Research Laboratory, Mechanics and Explosives Effects Research Group based at Tyndall Air Force Base in Florida for performing dynamic testing of several concrete masonry walls. I also would like to thank Dr. Jun Suk Kang at Georgia Southern University for providing technical advising that was fundamental to creating finite element models for the project. I am appreciative to all the men and women who have kept me on the straight and narrow, who have taught me what how to be a true man and a true man of God. I thank my parents for providing an infinite amount of support, financially and emotionally, over the last twenty-four years and who have always been loving and accepting of everything I wanted to do. You are my rock which without I would have long been pulled under. Finally, I express gratitude to the Father, the Son, and the Holy Spirit for providing me new life, new strength, and infinite joy; you have provided me the ability to accept any situation thrust upon me and are the only reason I am here.

Table of Contents

List of Tables

List of Figures

CHAPTER 1

INTRODUCTION

1.1 Overview

Starting in World War II when bombs and explosives began to be used as conventional weapons, researchers began to look into ways to mitigate the forces caused by blast. In the Cold War, the threat of large scale nuclear bombs lead to research in whole system structural response to blasts. However, the Oklahoma City Bombing and World Trade Center Bombing in the 1990s showed the damaging effects of more localized blasts. The usage of improvised explosive devices following 9/11 has given an importance to research on localized response and local phenomenon.

Blast loading is a dynamic load. A dynamic load is loadings that changes over time and can cause increased deflection and higher accelerations relative to a static load of the same intensity. However, unlike forces resulting from wind and earthquakes, blast loading cannot be readily transformed into equivalent static forces. This requires that the structure to be modeled as a dynamic system. Blast loading, like earthquake, is not typically expected to be endured without damage. Blast could cause varying levels of damage, from a few cracked windows to complete collapse; therefore, the primary objective of blast design criteria focuses on the preservation of life, instead of a preventing damage. One of the main concerns is that the loading can produce breaching

of the cladding leading to high velocity fragmentation or allowing the blast wave to enter into the structure. Both can cause loss of life.

A common type of building material is masonry. Masonry has been used for millennia as a building material. The first buildings were crude stacks of natural stone; this eventually transitioned into manufactured stone with mortar and into brick and mortar. Starting in the 1800s, concrete masonry units (CMU) began to be used for a wide range of building applications. In modern society, CMU is being used as shear walls to resist lateral loads or as cladding on the exterior of structures. This is because this wall type is relatively inexpensive, is easily and quickly constructed, and provides insulation for the structure. However, unreinforced CMU walls are weak in flexure and must be grouted and reinforced to handle flexural loading. Since grouting every cell of the CMU can be costly, owners and contractors often only grout cells that have reinforcement running in them.

Unified Field Criteria (UFC) 3-340-02 *Structures to Resist the Effects of Accidental Explosions* (UFC, 2008) allows the use of partially grouted CMU walls along as the wall is still designed to meet the flexural demand. However, a recent study (Davidson et al., 2011) on partially grouted walls has shown that blast loading can cause localized stress and cause fracturing leading to loss of life. Therefore, partially grouted walls can behave similar to unreinforced masonry walls. Therefore, the overall objective of the work represented by this thesis was to define the situations in which it is safe to use partially grouted CMU walls.

1.2 Objective

The overall objectives of the research were (1) to develop an understanding of the causes of breaching of partially grouted CMU walls subjected to blast loading by using finite element modeling and (2) to develop an engineering-level design equation to predict direct shear and breaching in partially grouted CMU walls.

1.3 Scope and Methodology

In order to complete the objectives, several different tasks had to be performed which included a literature review, development of finite element models, a suitability study, and development of a resistance equation. The finite element models were created and visualized in LS-PrePost; and analyzed using the LS-DYNA finite element solver. Full-scale static and dynamic testing results were used to verify the modeling approach. The testing was performed as part of a previous study by the Air Force Research Laboratory (Davidson et al., 2011) for evaluating minimally reinforced partially grouted walls. The resistance equation was derived by examining the behavior of the finite element models, and structural dynamic and quasi-static models of CMU were created to approximate the breaching behavior.

1.4 Organization of Thesis

The thesis is broken into five chapters. Chapter 1 consists of an introduction, objectives, scope and methodology, and organization of the thesis. Chapter 2 provides a literature review including a brief look at the literature on blast loading, concrete masonry units, mortar, and finite element modeling. Chapter 3 provides an overview of the full-

scale dynamic testing, a summary of the finite element methodology, a verification of the finite element modeling, and a suitability study of the breaching phenomenon. Chapter 4 discusses the breaching and shearing behavior of CMU due to blast loading and details the development of the shear design equation. Chapter 5 summarizes the thesis and gives recommendations for designers and researchers.

CHAPTER 2

LITERATURE REVIEW

2.1 Overview

With the increase in terrorist activity across the world, there has arisen a focus on making structures more resistant to blast loading. Several researchers have looked at a vast array of materials including steel, reinforced concrete, and masonry. Since masonry, especially CMU, is a common type of building material for exteriors walls, many researchers have looked into improving the performance of masonry subjected to blast loading.

Since masonry has very low tensile strength, the wall performs poorly in flexure unless a ductile reinforcement is added into the assembly. In order to do this, reinforcing steel is added into hollow sections of the CMU. To provide composite action between the steel and CMU, grout, a flowable concrete mixture, is placed in the cell. If grout is placed into every cell (with or without reinforcing steel), the wall is said to be fully grouted. To minimize costs, many contractors and owners prefer to only add grout to cells that have steel in them. If this is done, the wall is said to be partially grouted.

Over the years, a great deal of work has gone into modeling masonry walls that are unreinforced, reinforced, or fully grouted; several researches have also looked at catcher systems and energy absorption systems. However, there is a general lack of research into partially grouted, reinforced walls and the difference in their failure mechanics. This

thesis focuses on the phenomenon where there is a direct shear failure that occurs between the grout columns; this type of failure is called breaching. The direct shear or breaching shear causes shear cracks to form in the block.

2.2 Concrete Masonry Units

2.2.1 Flexural Behavior

The flexural behavior of CMU has been researched thoroughly. The masonry section of Unified Field Criteria (UFC) 3-340-02 (UFC, 2008) states that "the method of calculating ultimate moment of [combined joint and cell reinforced masonry] is the same as that presented in [the chapter on concrete]." UFC then gives the ultimate moment capacity, M_n, for a concrete beam or non-load bearing wall as

$$M_n = A_s f_{ds}(d - a/2) \tag{2-1}$$

where A_s = area of the reinforcement, f_{ds} = dynamic yield strength of the steel reinforcement, d = distance between the centroid of the tension reinforcement and extreme compression fiber, and a = the depth of the equivalent rectangular compressive block. UFC 3-340-02 makes no differentiation between fully grouted and partially grouted walls. This is because research has shown both types of grouting works well if the wall is designed properly. Other sections of UFC 3-340-02 go into detail establishing rules and guidelines for damage levels from "lightly damaged" to "collapse" and the design of slabs for one-way and two-way actions.

Davidson et al. (2011) tested several partially grouted CMU walls under uniform static pressure in vacuum chambers. These walls were made of 8-in and 6-in CMU with minimum reinforcing and only the reinforced cells being grouted. The walls were loaded

only by pressure and self-weight; the pressure was the same along and across the wall and increased to failure. These walls first cracked along the bed joint at the course nearest to mid-height of the wall. These walls were able to carry additional load with increased cracking and deflection. Eventually, the walls failed in flexure due to self-weight and did not show any signs of shear failure, conventional or breaching. Plots of midheight deflection versus applied pressure were created; these showed that the resistance of the wall can be described by three behavioral regions. The first is linear-elastic resistance until cracking. This is followed by a nonlinear resistance caused by changing progression of cracking and straining of steel, and the last section is a ductile displacement under a constant load until the wall's failure. In a linked study, Davidson et al. (2011) tested three of the identically constructed panels using blast loading. In several of the walls, the failure mechanism changed from a ductile failure in flexure to a brittle failure in breaching. The breaching occurred between the grouted cells, typically occurring at the interface between grouted and ungrouted blocks. Davidson et al. (2011) was used as the primary driver for this work and data from this report was used to validate this work.

Burrett et al. (2007) tested many large scale CMU walls when subjected to impact. In their research, they developed finite element models to model the impact and resulting damage and found analytical resistance models of unreinforced, ungrouted walls. In their analytical modeling, they performed a parametric study to find the key components of the resistance functions.

Gilbert et al. (2002) developed a rigid-body mechanism analysis of unreinforced masonry walls. In this analysis, rocking, sliding, and a combination of rocking and

sliding were analyzed for impact. Five wall-failure mechanisms were found as analysis tools for the prediction of failure and displacement. The analysis allows for the prediction of the peak displacement to within a ten percent upper and lower bound. Analysis correlated well with the displacement for all failure modes, except one.

Sudame (2004) developed a finite element modeling approach that predicts the overall resistance of ungrouted walls subjected to blast loading. Moradi (2008) further developed on Sudame's work by providing modeling of retrofits. The paper develops resistance functions for three different retrofits. These were compared to data of walls subjected to real blast loading for verification.

2.2.2 Shear Behavior

In *Masonry Structures Behavior and Design* (Drysdale and Hamid, 2008), the nominal shear strength, V_n, is generalized by

$$V_n = V_m + V_s \tag{2-2}$$

where V_m = strength provided by the masonry, and V_s = strength provided by the steel reinforcement. The strength provided by the masonry also takes into account the effects of frictional forces caused by the axial load on the wall. In American Concrete Institute (ACI) 530-11 (ACI, 2011), the nominal shear capacity provided by the masonry, V_m, of a reinforced masonry wall using strength design provisions is given by

$$V_m = \left[4.0 - 1.75\left(\frac{M_u}{V_u d_v} \right) \right] A_{nv} \sqrt{f'_m} + 0.25 P_u \tag{2-3}$$

where M_u = the ultimate factored bending moment on the section, V_u = the ultimate factored shear on the section, d_v = the depth of the member in the shear direction, and P_u

= the ultimate factored axial load on the section. The nominal shear capacity provided by the transverse steel, V_s, for a reinforced masonry wall using strength design provisions is

$$V_s = 0.5\left(\frac{A_v}{s}\right) f_y d_v \tag{2-4}$$

where A_v = the area of the transverse steel, f_y = the yield stress of the steel, and s = the spacing between layers of transverse steel. Since most walls do not provide transverse steel for out-of-plane bending, the shear contribution attributed to the steel is zero.

UFC 3-340-02 states, "Cell reinforced masonry walls essentially consist of solid concrete elements….Shear reinforcement for cell reinforced walls may only be added to the horizontal joint similar to joint reinforced masonry walls." The shear capacity for joint reinforced masonry, V_u, is

$$V_u = \frac{\phi f_y A_v A_n}{bs} \tag{2-5}$$

where ϕ = strength reduction factor equal to 0.85, A_n = the net area of the section, and b = the width of the wall. For walls without joint reinforcement, the shear capacity is zero according to UFC 3-340-02.

UCF 3-340-02 provides no additional details in the masonry section on direct or breaching shear. However, in the concrete section, it gives a minimum area of steel to be provided at supports, A_d, for a beam as

$$\mathrm{A_d} = \frac{V_s b - V_d}{f_{ds} \sin(\alpha)} \tag{2-6}$$

where V_s = the shear at the support of width b, V_d = the direct shear capacity of the concrete, b = the width of the member, f_{ds} = the dynamic design stress of the steel, and α = the angle formed by the plane of the diagonal reinforcement and the longitudinal

reinforcement. The section applies to masonry walls only when they are fully grouted. In addition, a proposed update to UFC 3-340-02, Oswald et al. (2010), states that no direct shear be designed for in wall with expected blast exceeding a standoff of 3 ft/lb$^{1/3}$ and that only fully grouted walls be used for standoffs less than 3 ft/lb$^{1/3}$. There are no comments on how to design for between grouted section breaching.

Psilla and Tassios (2009) evaluated several design shear strengths and several other research shear equations. The authors then developed shear strength equations using "tensile strength and compression strength of masonry, masonry to masonry friction, and pullout force." The equations predicted three failure modes, 1.) diagonal cracking, 2.) disintegration of web, and 3.) diagonal compression failure and were calibrated using experimental data on the ultimate shear load. The shear equations were compared to several design equations and found to better match experimental data than design equations given in American Concrete Institute, New Zealand Standard, and Canadian Standard Association.

2.3 Mortar Properties

Since mortar is inherently weak in tension, it is a major contributor to the failure mechanism of CMU walls in bending and shear. Therefore, the mortar's properties must be defined. One of the major contributors to the strength of the mortar is bond strength. Drysdale states "bond is perhaps the most critical factor because it influences both the long term strength and the serviceability of the finished masonry." He later says "mortar should have sufficient bond for water tightness and to resist tensile stress due to external loads" (Drysdale and Hamid, 2008). The bond contributes to both the tensile and shear

strength of the mortar. The bond strength is affected by properties of the masonry block, mortar type, workmanship, water-cement ratio, and curing conditions. Most of these parameters are not fixed and are determined in the field by the mason. Also, bond usually has no fixed limits. Therefore, bond strength of the mortar can have a wide range with few known values.

In order to quantify the mortar's bond properties, researchers have looked into the tensile bond strength. Hamid and Drysdale (1988) looked into the tensile block arrangements. The modulus of rupture values are 30.5 psi (0.21 MPa) to 242 psi (1.67 MPa) for failures normal to bed joints; the values are 120 psi (0.83 MPa) to 290 psi (2.00 MPa) for failures parallel to bed joints. To limit the variables, only values for non-grouted sections were used. The range of ungrouted arrangements is 30.5-128 psi (0.21-0.88 MPa) for normal to bed joints; the range of ungrouted arrangements for parallel to bed joints is 120-216 psi (0.83-1.49 MPa). The median values are 49.3 psi (0.34 MPa) for ungrouted normal failures and 168 psi (1.16 MPa) for ungrouted parallel failures. ACI 530-11 (ACI, 2011) provide values for modulus of rupture for different mortars (M, S, and N); these are provided in Table 2.1. These values are not in the ranges found by research; this would be because ACI 530-11 gives conservative values for modulus tension failures.

Table 2.1. Modulus of rupture values from ACI 530-11

Direction of Flexural	Masonry type	Portland or Mortar Cement (psi)		Masonry cement (psi)	
		M or S	N	M or S	N
Normal to bed joint	Ungrouted	33	25	20	12
	Fully Grouted	86	84	81	77
Parallel to bed joint	Ungrouted	66	50	40	25
	Fully Grouted	106	80	64	40

Several researchers have looked into the shear bond strength as well. Atkinson et al. (1989) performed direct shear tests on clay bricks and compared this to reported values for other clay bricks and concrete blocks. The Atkinson et al. also gave shear strength for concrete blocks ranges from to studies. These values range from 0 to 399 psi (0 to 2.75 MPa) for one study and 0 to 232 psi (0 to 1.6 MPa) for another.

2.4 Blast Loading

Blast loading occurs when a pressure wave caused by an explosion strikes an object. Since explosions are very destructive and very brief, little data can be obtained from each explosive test; however, with the proper equipment and some care, data, such as maximum deflection, pressure histories, and high-speed video, can be obtained. The data can provide a way to analyze a system's response to blast loading.

An explosion can be described as a sudden release of potential energy from a source; this release of energy develops into a thermal energy difference creating an air burst with high kinetic energy. The air burst causes an increase to pressure traveling as a spherical wave to the surrounding area. At the edge of the wave, there is a sudden increase of pressure from the atmospheric pressure; the difference in these two pressures is called the peak pressure. After the shock front passes, the pressure decreases in an almost linear fashion to atmospheric pressure. After atmospheric pressure is reached, the pressure continues to decrease until is reaches the peak negative pressure; at this point the pressure increases to atmospheric pressure. This portion of the loading is curved. It is called the negative phase and characterized by suction or negative pressure. In Figure 2.1, a idealized pressure loading profile is shown; this is characterized by a sudden increase to pressure with a linear decrease to zero and a linear negative phase with the

maximum negative pressure occurring at a quarter of the negative time. The idealized curve is created using table in UFC 3-340-02 and using a scaled standoff specified as the distance the object is from the blast source compared to the weight raised to the 1/3 power.

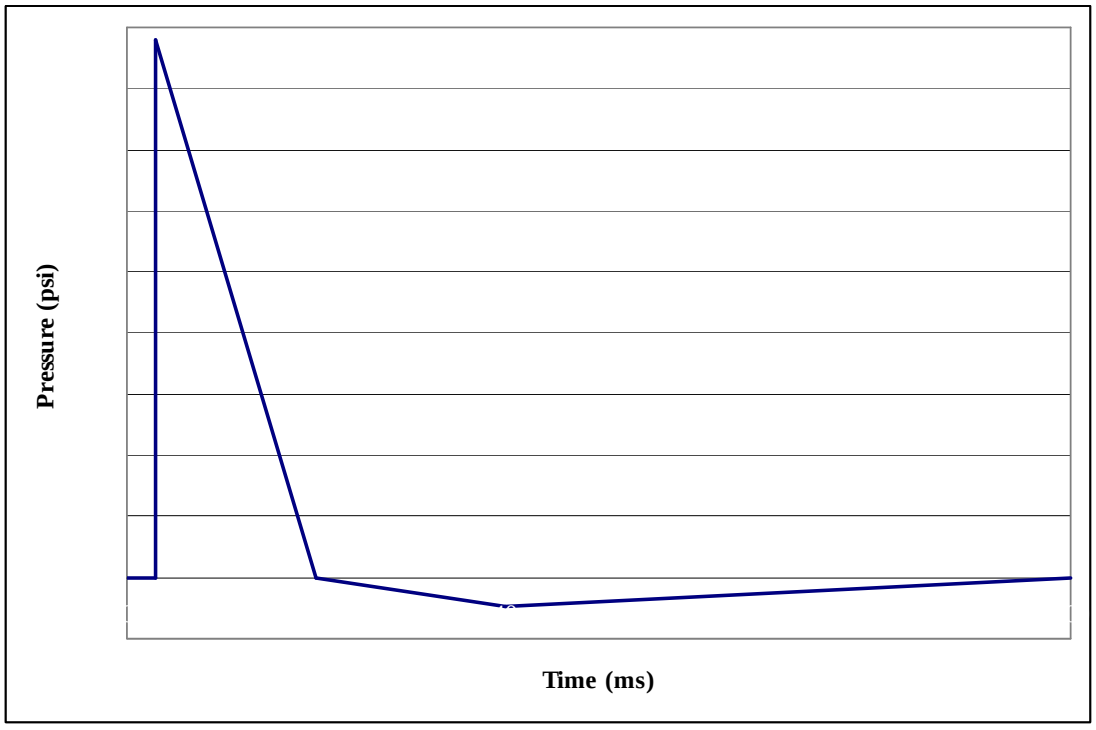

Figure 2.1. Pressure loading profile

As the pressure wave travels outwards, it strikes objects creating a reflected pressure wave. The reflected pressure causes an increase of the pressure above the air burst pressure and is usually the pressure that all structures are designed to resist. The present work uses UFC 3-340-02 because it is the design standard for most building in the United States when an explosion can occur at a facility.

There are many sources of explosions. Since different explosions have very different characteristics, a generalized way of describing different explosives has been developed. Any explosive can be compared to trinitrotoluene (TNT); TNT is used to

describe explosive effects because its properties and resultant pressure wave are well-defined. The above discussion and figure are based on the properties of a TNT explosion. UFC 3-340-02 gives the following equation to find the equivalent weight of TNT, $W_{EQV,}$ as compared to a given weight of an explosive.

$$W_{EQV} = \frac{H^d_{EXP}}{H^d_{TNT}} W_{EXP} \tag{2-7}$$

where H^d_{EXP} = heat generated by the explosive, H^d_{TNT} = heat generated by TNT, and W_{EXP} = weight of the explosive. This equation allows for the scaling of an explosive where design guides can be used.

2.5 Finite Element Modeling

2.5.1 Constitutive Models for CMU

Since concrete components are essential in almost all buildings, finite element models have been developed to model different structures in different environments. These FEMs are primarily concerned with the performance of individual components of a structure, especially the failure of components.

In order to better simulate the failure and cracking in concrete structures, several models have been developed. Listed in the LS-DYNA User's Manual, Volume I (2009), there are 26 different material models that are described as being suited for soil, concrete, or rock. The wide selection can be attributed to the many tests and properties needed to clarify the behavior of concrete. Also, several models have been developed to help modelers by providing simple inputs and parameter generation algorithms.

Davidson and Moradi (2008) looked at five material models (Soil and Foam, Soil and Foam with Failure, Brittle Damage, Pseudo Tensor, and Winfrith Concrete) in order to find the best model for CMU subjected to blast. In order to test these models, a blast test was set up with single blocks at various standoff distances. The results were compared to finite element simulations ran in LS-DYNA. It was concluded that the Soil and Foam model best matched the test.

Magallanes et al. (2010) mentioned that CMU acts like lightweight concrete and stated that the LS-DYNA material model Concrete Damage Release 3 "can provide excellent results if properly calibrated for these materials." Very few others have looked directly at modeling and determining the best model for CMU.

2.5.2 CMU Models

While there is little information on constitutive models for CMU, there is much more information on performing finite element modeling of CMU. Most of the work focuses exclusively on modeling walls.

Martini (1997) developed a one-way masonry wall model to help in the investigation of rebuilding of Pompeii following an earthquake in 62 A.D. In the model he proposed a block-interface model where the mortar is not modeled, but the interface between blocks retains the failure condition of the mortar. This model matched well with the work published on static tests of one-way walls. Martini (1998) used the same block-interface model to model two-way bending of masonry walls. The model showed that as deflection of a wall increases the reaction changes from the base carrying almost all the reactions to the base only carrying vertical reactions and the side supports carrying lateral

reactions. He also noticed the blocks created moment couples along the edges. Finally, he noticed the failure pattern matched well with yield line pattern of the reinforced concrete slabs and created a method to apply the yield line analysis for masonry walls.

Burnett et al. (2006) performed finite element modeling on CMU walls subjected to low-velocity impacts. The authors detailed the creation of a discrete-crack model that employed tied interface contact definition with normal and shear interface failure stresses, dilatant friction, gravity loads, and viscous hourglass control. The modelers also developed a Mohr-Coulomb failure surface in the compression zone and a hemispherical cap in the tension zone. This model looked at impacts of a steel plate on CMU and brick walls and was used to determine wall failure modes, maximum displacement, and the influence of bonding pattern.

Dennis et al. (2002) developed a CMU model of a single strip of blocks in the vertical direction. The modeling approach used most of the same concepts as Burnett's model. In his model, he used both quasi-static pressure test and dynamic blast test to verify the model taking into account maximum out-of-plane deflection and failure analysis; the model was conservative by a slight amount but was not able to accurately predict all failures.

Eamon et al. (2004) developed a model similar to the one in Dennis et al.; however, his was able to accurately predict the failure modes. Their work showed that there were three different failure modes for out-of-plane bending, (1) two-segment arching with the block remaining intact at low pressures, (2) two-segment arching with increased deflection and boundary block rotation leading to failure at medium pressures; and (3) multiple segments being expelled from the wall at various velocities at high

pressure. The model also showed sensitivity to the material parameters; however, a change in failure type and a change in expolsion velocity were relatively insensitive to material parameters.

Browning (2008) modeled multi-wythe walls that were fully grouted and had a brick veneer filled with a foam cavity. In his model, he replaced the grout and CMU with a composite material with composite properties based on area. The brick veneer was not modeled directly, but its mass was added into the foam. The foam was not modeled directly because it was assumed to only provide energy damping. Using the model, he developed engineering-level equations for out-of-plane bending using single degree-of-freedom and multiple degree-of-freedom methods.

In addition to conventional CMU modeling, there has been some research into modeling CMU retrofits. Sudame (2004) built a model for CMU wall with a spray-on polymer retrofit attached to the interior side of the wall. In modeling the polymer, he used a rubber material model, a tied contact definition with tension and shear failures stresses, and a rupture failure definition. He also used a tied interface for the mortar joint with failure stresses. His research included a parametric study. Moradi's (2008) work is an extension of Sudame; he developed a CMU model based on the work of Sudame's model; Moradi's main focus was the development of a resistance equation for flexure which takes into account the effects of the retrofit.

CHAPTER 3

FINITE ELEMENT MODEL DEVELOPMENT AND METHODOLOGY

3.1 Overview

Since concrete masonry walls are nonlinear both in their geometry and their material properties, finite element modeling is a valuable tool for understanding the behavior of these walls. The drawback of finite element is that it can be complicated in developing a valid model for analysis; however, after the model has been validated, it can be used to perform a large number of virtual testing of complicated systems at a high efficiency. LS-DYNA produced by Livermore Software Technology Corporation is the finite element solver chosen because it is an advanced, general-purpose solver with the ability to run nonlinear, dynamic analysis. In order to do the preprocessing and post-processing, LS-PrePost, also produced by Livermore Software Technology Corporation, was used because of its compatibility with LS-DYNA. Any specifics in the following sections are given for input into LS-DYNA; these can be modified to model CMU for any appropriate finite element program, but these details should be viewed only as input for this one phenomenon and not as instructions to model CMU. In addition to the input detailed below, a typical keyword input file can be seen in the appendix.

3.2 Dynamic Testing Overview

Prior to the beginning of this analytical research, a series of full-scale dynamic testing on partially grouted CMU walls were carried out by Air Force Research Laboratory researchers at Tyndall Air Force Base in Florida. The full details of the testing can be seen in Davidson et al. (2011). Some of the methodology and the dynamic testing are shared here to help develop a finite element model and to show the suitability of the model; the details and model should not be seen as a way to understand anything other than the breaching phenomenon addressed in this paper; this includes using the details to understand the flexural response or non-localized shear response.

3.2.1 Test Set-up

In the testing, three individual blast tests were carried out at three different scaled standoffs. These are shown in Table 3.1.

Table 3.1. Scaled standoffs of the dynamic testing

Test	**Scaled Distance** $\left(\mathrm{ft}/\mathrm{lb}^{1/3}\right)$
1	8.0
2	6.5
3	5.2

In each test, three panels were tested, giving a total of nine panels; each test had one of the following panels: (1) a 6-in. CMU wall, (2) an 8-in. CMU wall, and (3) a multi-wythe cavity wall made up of an 8-in. CMU wall with a 4-in. clay brick veneer. Each panel was 112 in. wide by 136 in. high. The 6-in. walls and 8-in. walls were a single wythe thick; the multi-wythe cavity walls were two wythe thick with a 2-in. polystyrene rigid board

insulation and 1-in. air gap between the veneer and wall. Table 3.2 describes some of the panels' construction details. The 8-in. wall was the focus on this thesis and the finite element modeling. Figure 3.1 shows the general dimensions of the 8-in. wall; the grouting is shown as being shaded and the reinforcing bars runs through the center of grout. Figure 3.2 shows the construction detailing of the walls. Figure 3.3 shows one of the tests with all three panels in the reaction structures prior to testing.

Table 3.2. Details of wall construction

Panel	Block	Reinforcement	Veneer
1	6 inch CMU	# 3 bars – 36 in. avg., 40 in. max	None
2	8 inch CMU	# 4 bars – 52 in. avg., 56 in. max	None
3	8 inch CMU	# 4 bars – 52 in. avg., 56 in. max	4 in. clay bricks

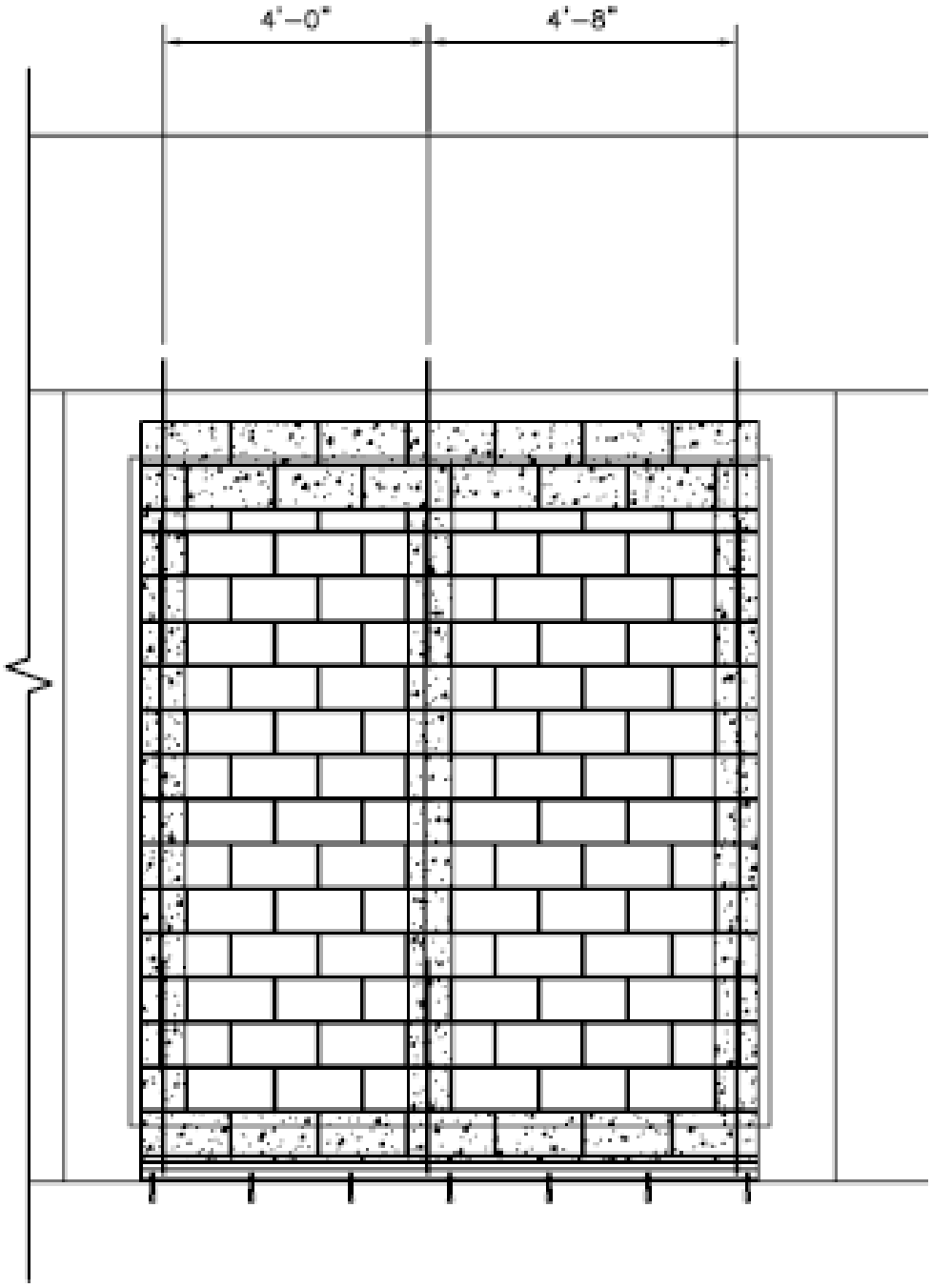

Figure 3.1. Front view of 8 in. CMU panel

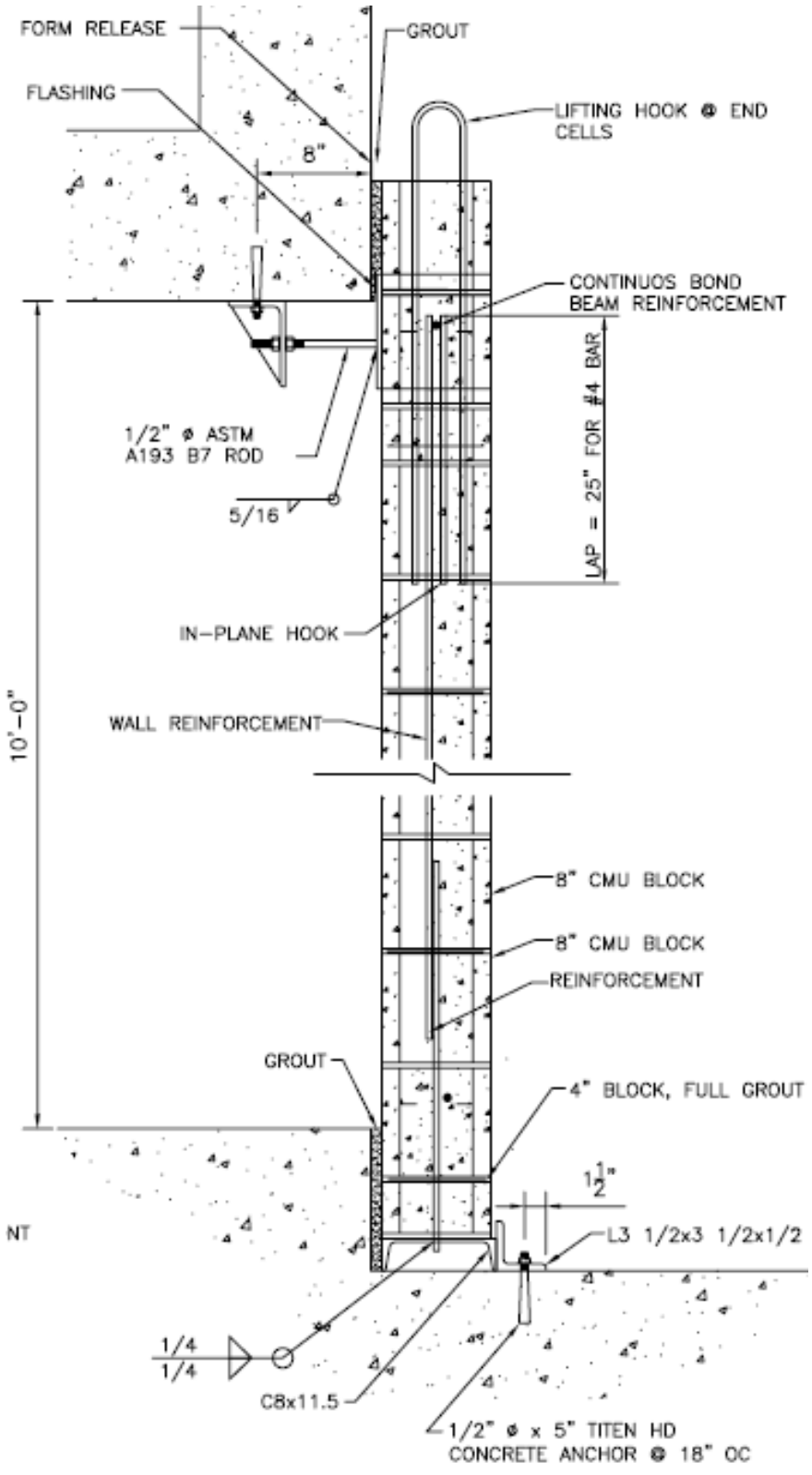

Figure 3.2. Details of construction and reinforcement of the 8-in. CMU wall

Figure 3.3. Panels in reaction structure prior to testing

Material testing was carried out according to ASTM Standards. The material properties can be seen in Table 3.3.

Table 3.3. Material properties

Material/Test	Value
Masonry Prism/ Compression Strength	Grouted: 6-in. CMU = 4870 psi 8-in. CMU = 4270 psi Hollow: 6-in. CMU = 2080 psi 8-in. CMU = 1290 psi Clay Brick = 4460 psi
Masonry Block/ Density	Density: 6-in. CMU = 112 lb/ft^3 8-in. CMU = 101 lb/ft^3 Clay Brick = 138 lb/ft^3
Mortar/ Compression Strength	3190 psi
Grout/ Compression Strength	7520 psi
Rebar/ Tensile Strength	Yield: #3 bars = 73900 ksi #4 bars = 66800 ksi Ultimate: #3 bars = 113000 ksi #4 bars = 106000 ksi Max. Strain: #3 bars = 0.141 #4 bars = 0.143

Additional details of the walls' construction or detailing can be seen in Davidson et al. (2011).

3.2.2 Test Results

The tests' purpose was to investigate the flexural response of minimally reinforced, partially grouted walls subjected to blast loading. In order to understand the flexural response, data on deflection and pressure were taken; high-speed cameras were also used on the outside and inside of the structure to capture the response. This data was analyzed and compared to existing single degree-of-freedom analysis tools used for blast design by industry. It was found that the wall's flexural response was considered conservative compared to the analysis tools. However, in testing the walls, it was found that large sections of the walls were breached between the grouted columns. Figure 3.4

and Figure 3.5 show typical breaching for the walls during testing. Figure 3.4 is a time progression of the breaching during the testing.

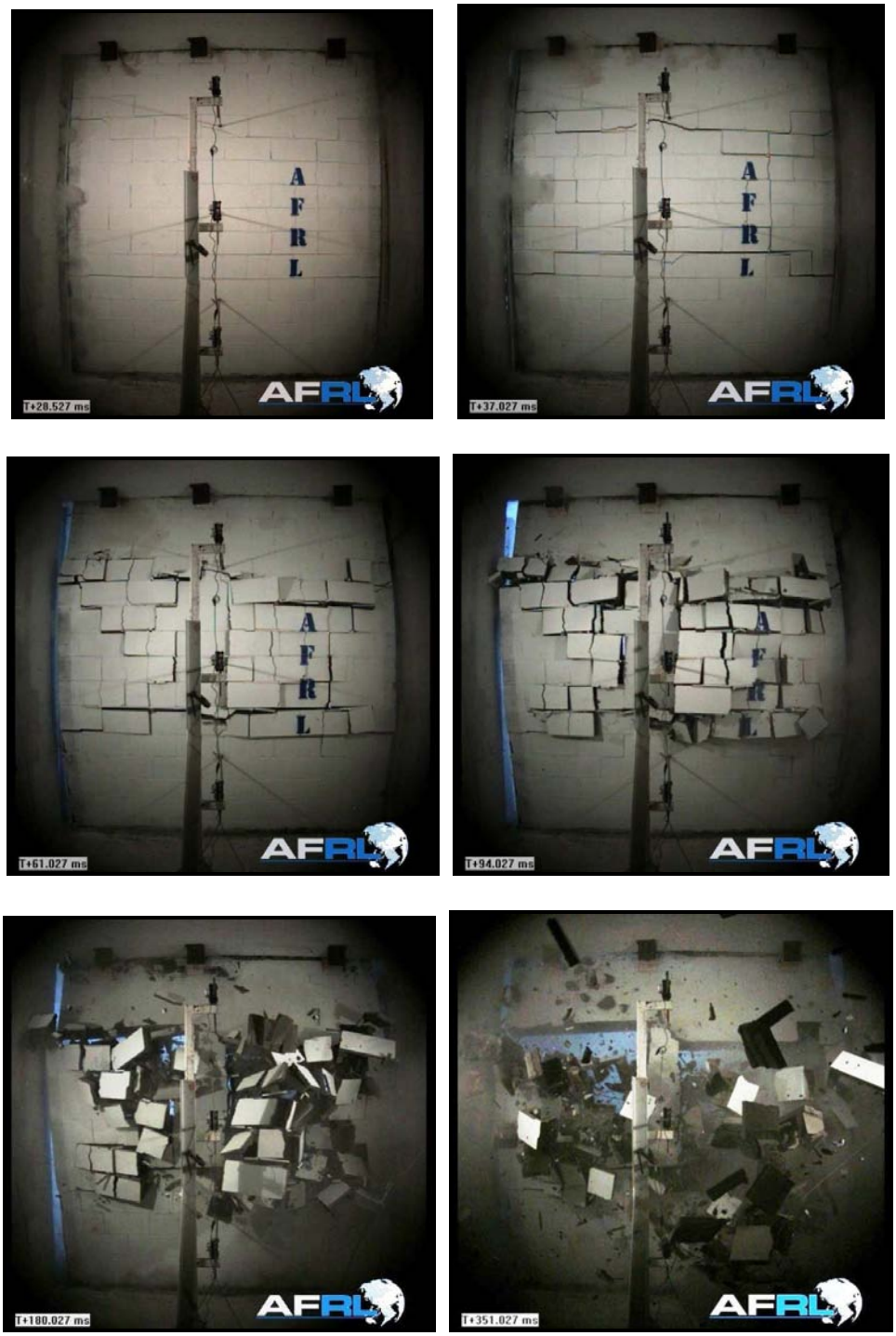

Figure 3.4. Breaching of 8-in. CMU wall during to test 2

Figure 3.5. Breaching of 8-in. CMU wall after test 2

In a linked study, these walls were also tested in a static pressure chamber and failed in flexure around midheight (Salim et al., submitted 2011). Since the walls were designed to fail in flexure, the shear breaching failure mode of the walls under dynamic loading was unexpected. In the recommendations of the report by Davidson et al. (2001), the researchers stated "additional testing and analysis of the between-column breaching phenomenon is needed." They also suggested that all walls that might be subjected to blast loading be fully grouted until a better diagnostic tool for breaching can be developed.

A better understanding of the testing methodology, resulting analysis, and conclusions and recommendations can be seen in Davidson et al. (2011). Also, the report goes into more detail on the flexural response of the wall than will be discussed in this thesis. Finally, this thesis will only use data and figures from Davidson et al. (2011) to demonstrate the suitability of the finite element models.

3.3 Unit System

LS-DYNA does not use units explicitly. It instead makes the modeler consciously express every input in consistent units. U.S. Customary units for force, length, and time were used in the model. All other units that are used are a derivation based on the units for force, length, and time. These are shown in Table 3.4.

Table 3.4. Unit system

Metric	Unit
Force	pound (lbf)
Length	inch (in.)
Time	seconds (s)
Mass	lbf-s^2/in.
Density	lbf-s^2/in.^{4}
Stress	lbf/in.^{2} (psi)

As a note, the unit millisecond (ms) will be used in this thesis because it is convenient to discuss and display data in that unit for blast loading instead of thousandth of a second.

3.4 Geometry and Meshing

Most masonry finite element models found in literature only used a single column of block in either running or stack pattern; this is a simplification that can be used for ungrouted or fully grouted walls because the walls are assumed to be well represented by a single column of blocks and to be homogeneous and the response is assumed to be dominated by one-way flexure. Since the phenomenon of breaching occurs between the grouted columns in partially grouted walls, the entire wall section had to be modeled; this is further complicated by using running bond pattern which means each successive course is offset by a half-block's length. Therefore, geometric discrepancies had to be employed to facilitate the modeling. These are discussed in the following sections.

3.4.1 Concrete Masonry Units

The typical 8-in. CMU is nominally 16 in. long by 8 in. wide by 8 in. high; in reality the block is 15.625 in. by 7.625 in. by 7.625 in. The 0.375 in. difference is to allow for mortar joints. With the addition of running bond, this forced the model to use a slightly different geometry than the one of typical CMU blocks. Figure 3.6 shows a comparison of a typical 8-in. CMU against a model 8-in. CMU used in modeling. As can be seen, the width and height of the section is the same in both models; however, the overall length of the members is reduced to 15.5 in. instead of 15.625 in. The outer webs are 1 in. wide in both blocks, but the center web for the FEM is 1.5 in. wide instead of 1 in. This causes the overall volume of the FEM block to be 432.2 in^3, instead of 415.1 in^3; the overall volume increased of area is 1.041%. This additional material is compensated for by reducing the mass density in the material modeling and will be discussed later. In addition, the CMU blocks have corner fillets while the FEM block has squared corners. The fillets have two effects. They change the mass of the block, and they cause less of a stress concentration at these corners.

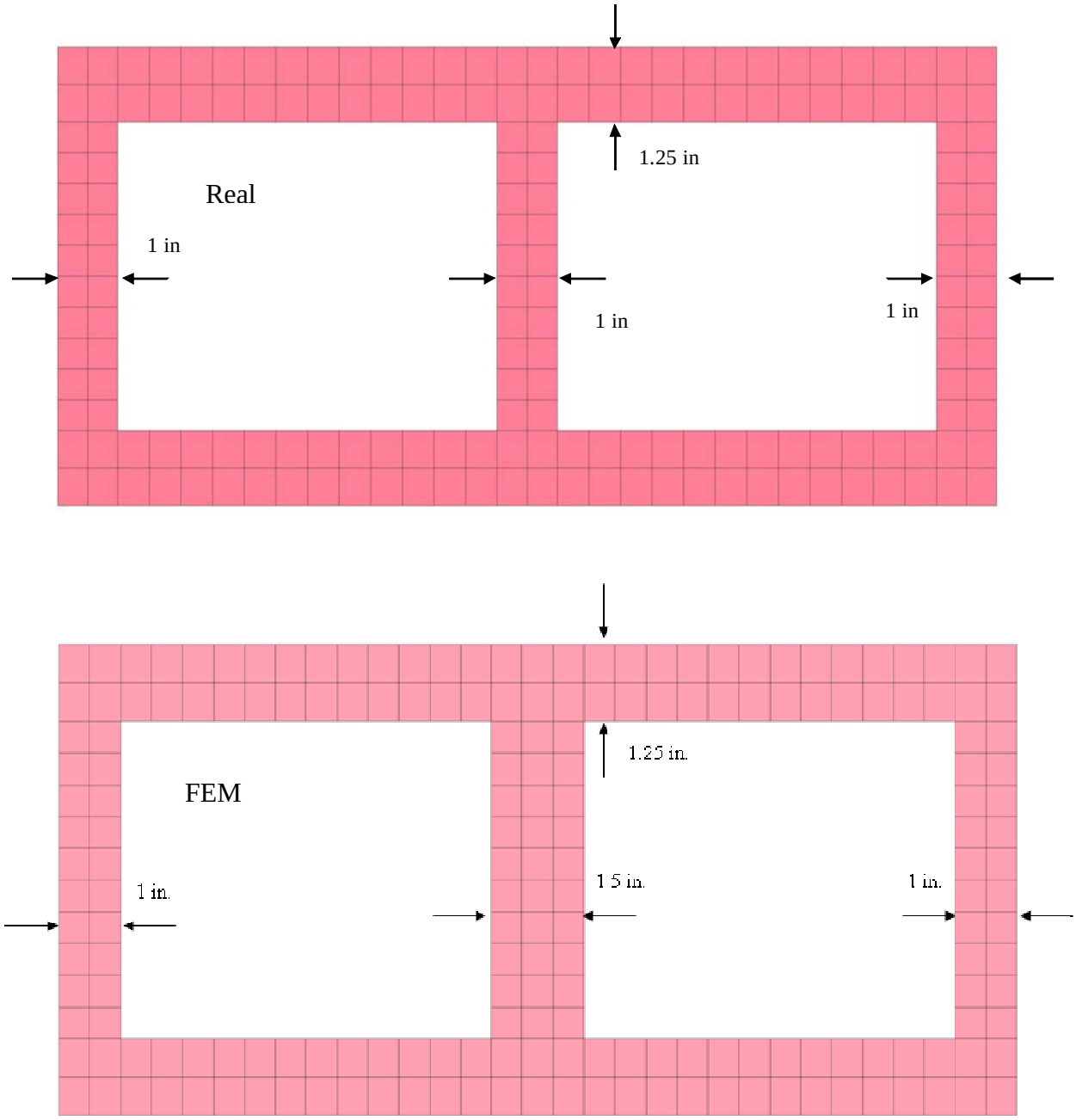

Figure 3.6. Comparison of real CMU and FEM CMU

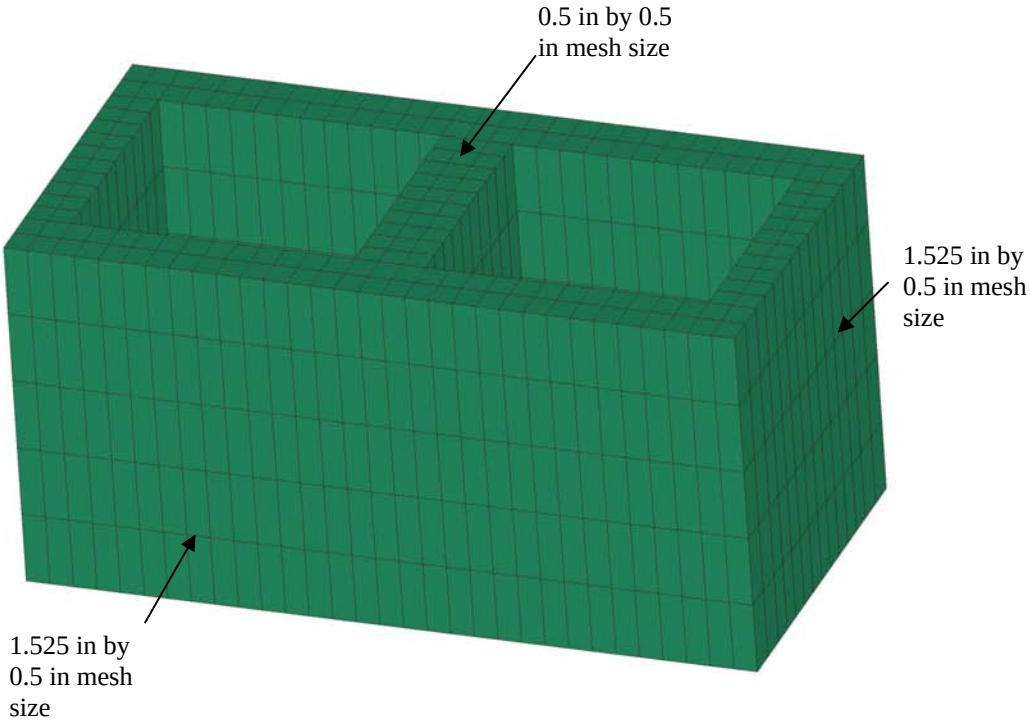

Figure 3.7. 3-D view of normal block

Figure 3.7 shows the three dimensional element size for the block is 0.5 in. by 0.5 in. by 1.525 in. This element size was used for all block. The size was chosen to provide two elements through the thickness of the faceshells and because analyses demonstrated that five elements through the height was efficient and accurate.

The model also employed U blocks and half-high blocks. U blocks are the same as the normal blocks except that the webs are removed to allow for continuity of grout in the bond beams. U blocks are modeled the same as normal CMU except the webs only consist of the lowest line of elements for the webs. The half-high blocks are only half the height of a normal block or 3.625 in. The half-high blocks only use 3 elements through the height at 1.21 in. A U-block can be seen in Figure 3.8; a half-high block can be seen in Figure 3.9.

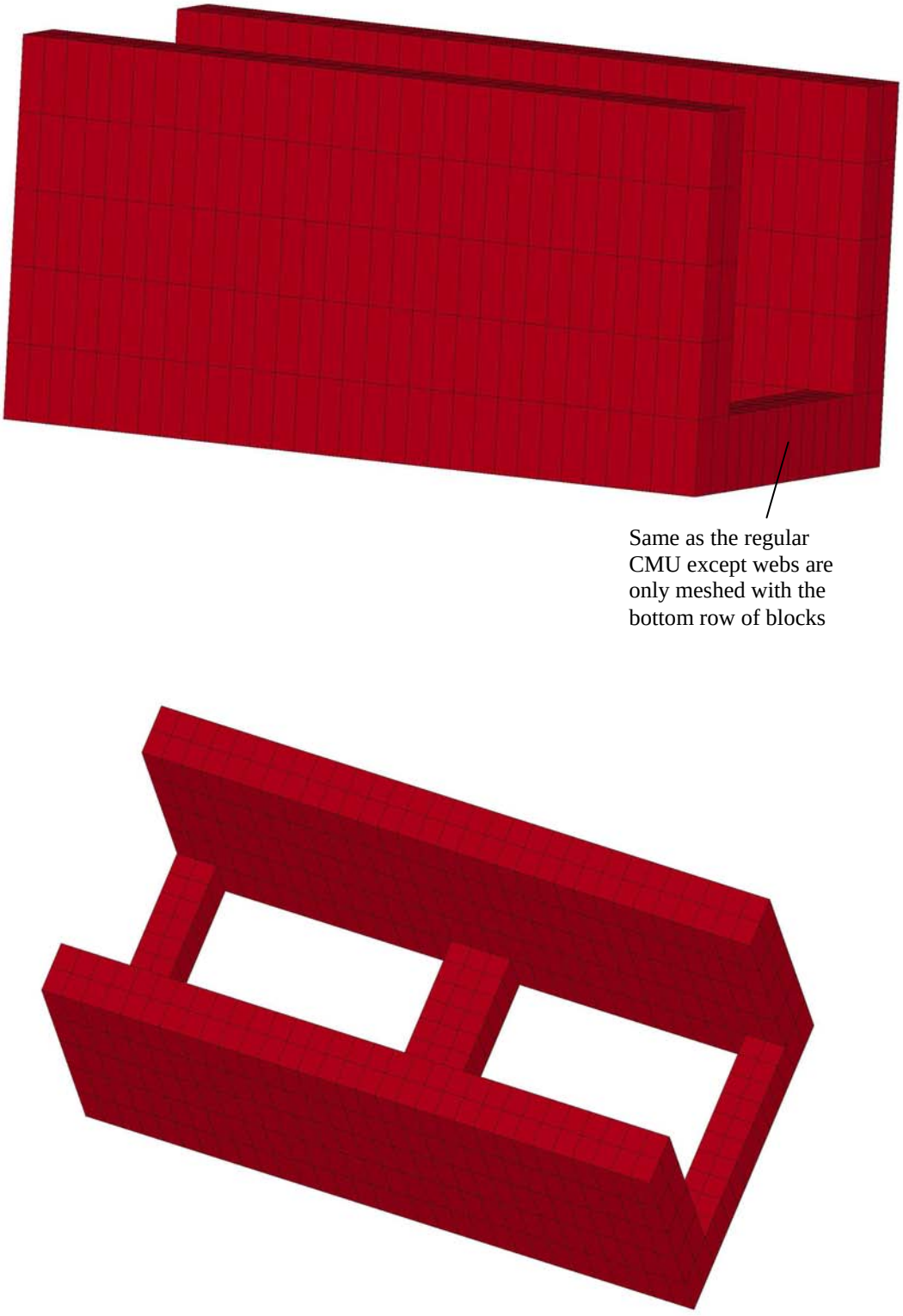

Figure 3.8. U-block used in FEM

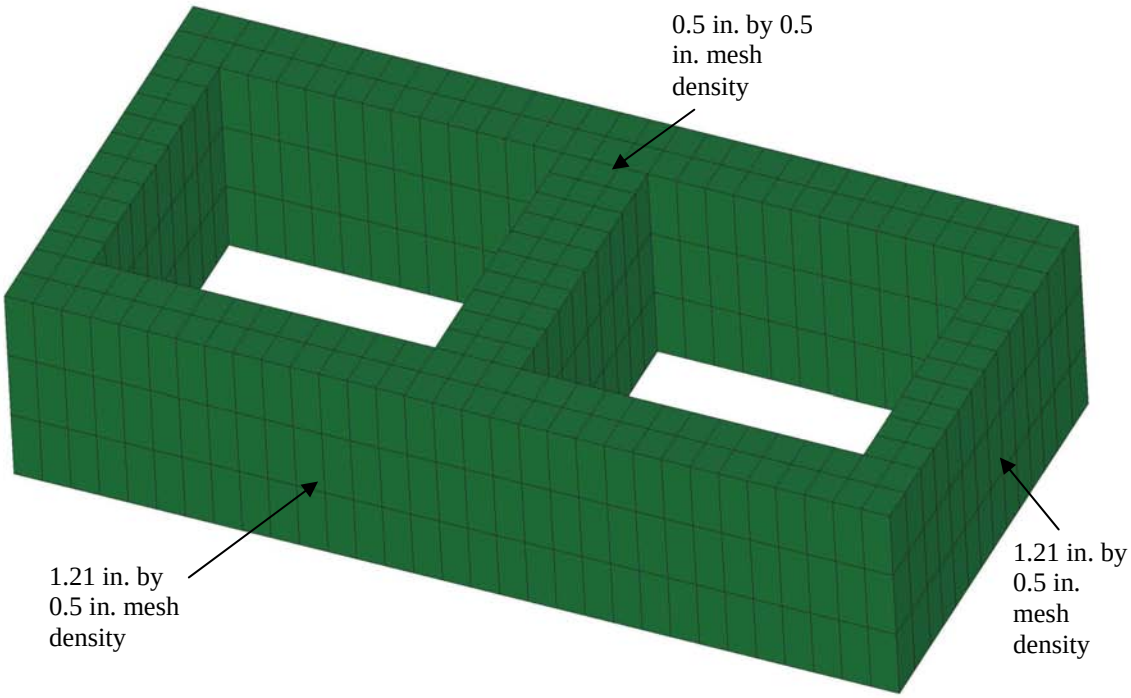

Figure 3.9. Half-high blocks used in FEM

3.4.2 Mortar and Grout

The running bond also caused challenges in meshing the mortar joints. Each head joint was modeled as 0.5 in. thick instead of the customary 0.375 in. This was done to facilitate the running bond pattern. The bed joints were 0.375 in. thick. Mortar was only simulated on the face shells as common in construction.

The mortar was modeled with the same element size as the CMU it is attached to (either 0.5 in. by 0.5 in. for bed joints or 1.52. in by 0.5 in. for head joints). This was done to allow for appropriate tying of nodes together. The mortar was modeled with one element through its thickness.

The grout was slightly affected by the running bond as the column was not necessarily straight. In some of the columns, the grout zigzagged following the slight

offset of each block from the one below it. The bond beams were not affected by the running bond. The element size of the grout for columns and bond beam matched the concrete block it is attached to (0.5 in. by 0.5 in. by 1.52 in. for normal blocks). This was done to allow the exterior nodes of the grout to share nodes with the CMU it was adjacent to and allowed a connection of the two. Figure 3.10 shows an 8 in. CMU with mortar for the bed and head joints and with one cell grouted. Figure 3.11 shows a grouted column without blocks encasing it; Figure 3.12 shows a bond beam with the bottom layer of blocks shown.

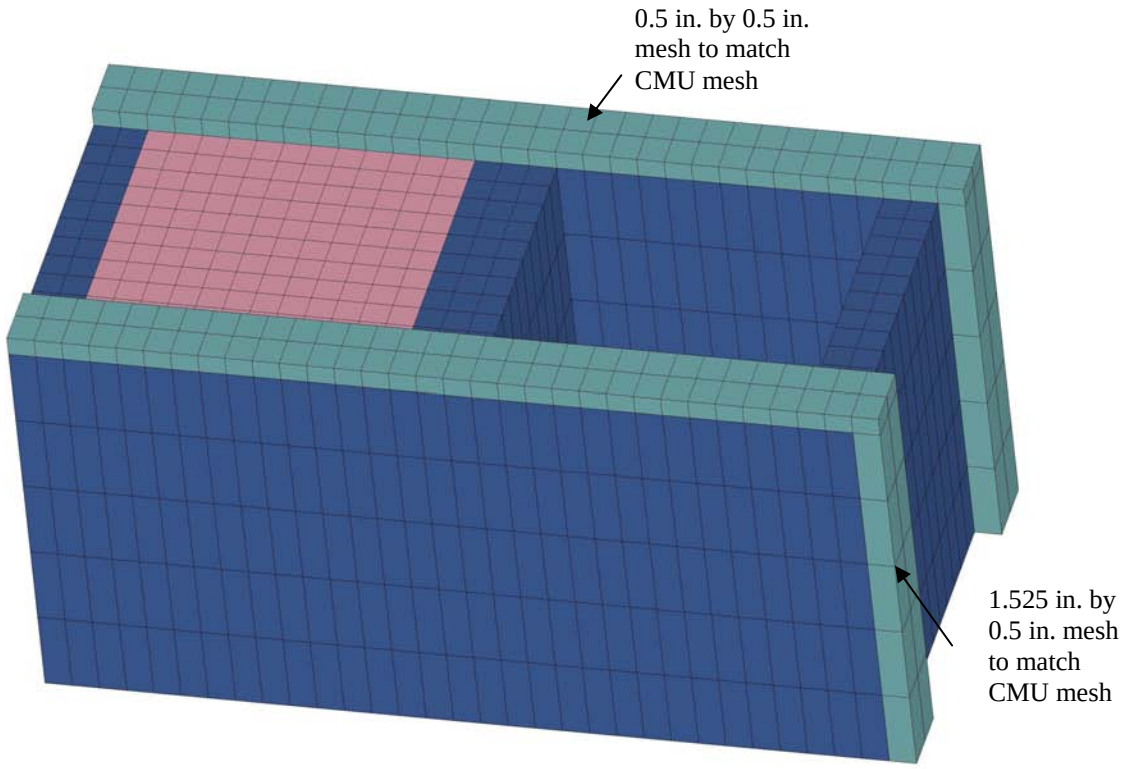

Figure 3.10. Mortar and grout meshing

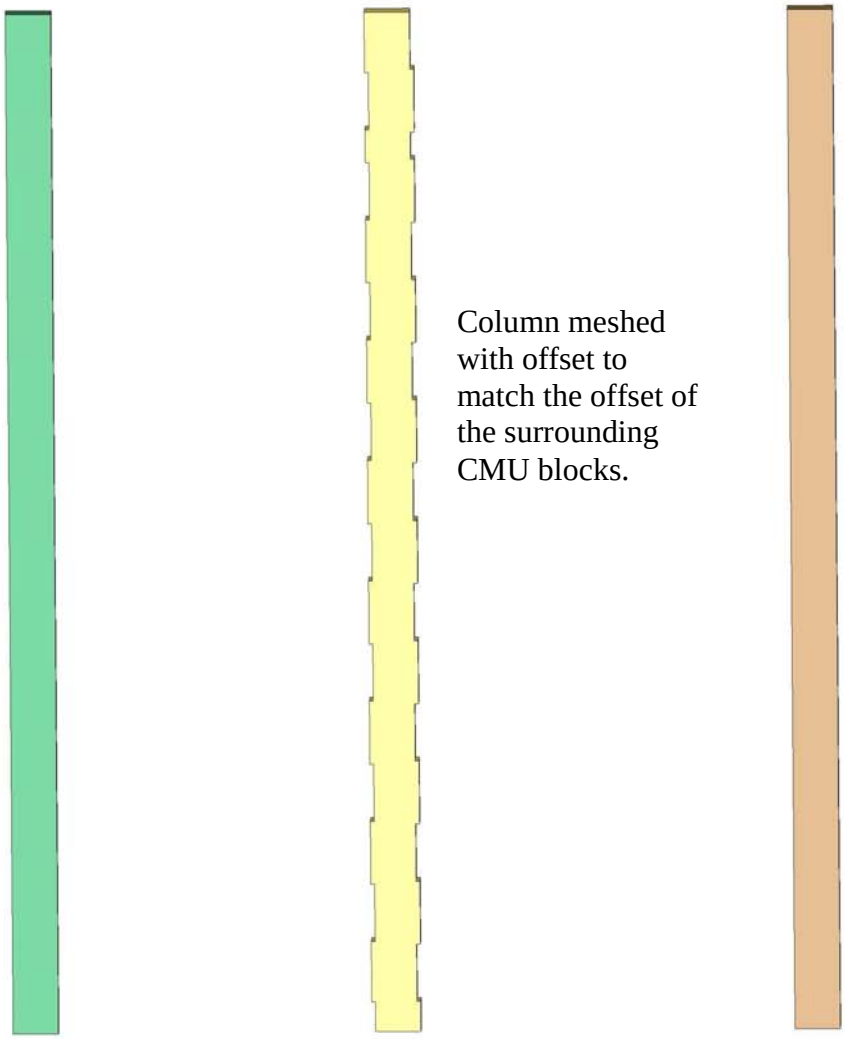

Figure 3.11. Grout columns

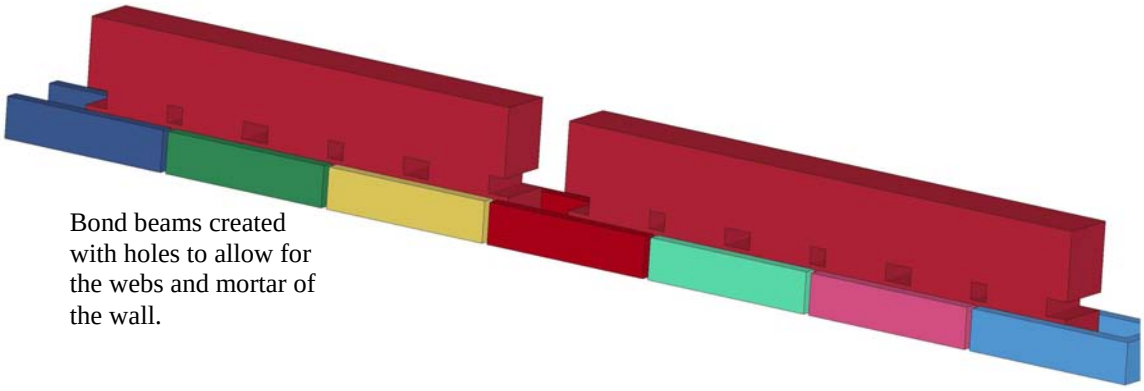

Figure 3.12. Bond beam and blocks

3.4.3 Steel Reinforcing

The steel reinforcing was meshed using one-dimensional beam elements. These were placed in the center of the cell for columns and the center of the bond beams. The main focus for modeling the beams was to make sure the beam shared a node with the surrounding grout elements; in order to do this, beam elements were generated for every grout section, and each beam was divided into sub-beams to attach at every grout node in the same location. The nodes of the beam shared the nodes with the grout elements. This was done to ensure compatibility between the steel and grout and thus to cause the beam elements to be properly stressed. Figure 3.13 shows reinforcing coming out of the grouting.

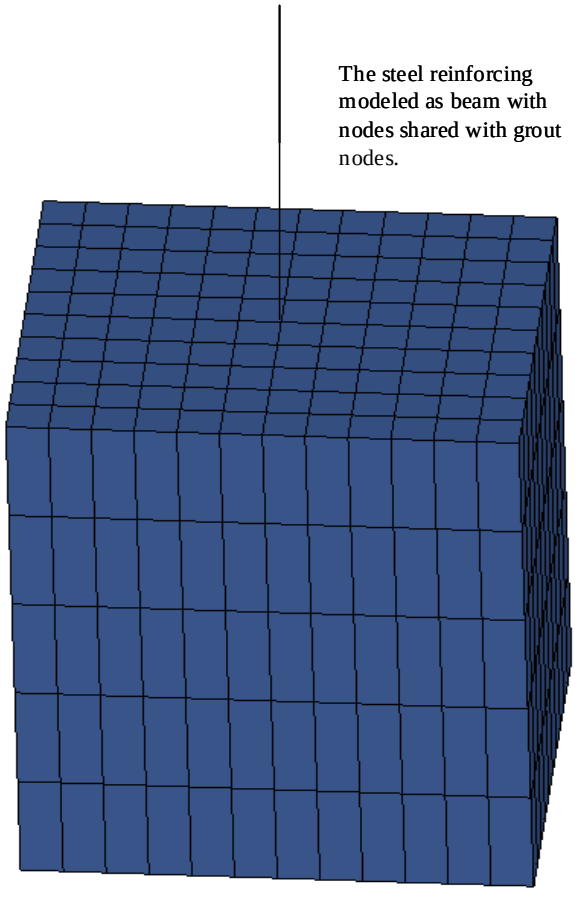

Figure 3.13. Beam embedded in grout

3.5 Material Modeling

LS-DYNA has a library of over 200 different material models that can be used for many different applications. The material models used for this work were chosen because they produced favorable results for similar research efforts or because the literature review highlighted these models as being a good approximation for the actual materials used. The following sections summarize the material models used in the model.

3.5.1 Cementitious Material Model

As mentioned earlier, there are 26 material models that have been developed for geological and cementitious materials; six of these models were determined to be appropriate for the present work. Table 3.5 shows the six models that were considered and the advantages and disadvantages of each model. All of the models would have been appropriate to model CMU with proper validation and material testing. At present, there is little literature on the properties of a single CMU block except in uniaxial compression. In addition to uniaxial, unconfined compression testing, Schwer (2001) list hydrostatic compression, triaxial compression/extension, and uniaxial strain as being necessary to properly characterize geomaterials. Since this data is not readily available and is needed in calibrating Mat 5 and Mat 14, these models were not used. The input of Mat 84 and Mat 85 is complicated and is built around reinforced concrete; therefore, these were eliminated. Mat 72 R3 requires minimum input with model generation; this model was developed to provide generic material and volumetric parameters around a 6610 psi (45.6 MPa) normalweight concrete. This material model was initially used because the input

was simple under the circumstances; however, upon running a few models it was determined that model's parameter generation did not fit CMU modeling because the model assume homogeneity and normalweight concrete. The model with the full-scale testing material inputs was too conservative giving deflections that were too low. Mat 96 is built around reinforced concrete section with several inputs just for reinforcing. However, Mat 96 allows for tensile and shear damage and was used in previous CMU wall modeling. The LS-DYNA Keyword User's Manual Version 971 Release 4 says that the model is "an anisotropic damage model…[admitting] progressive degradation of tensile and shear strengths across smeared cracks…under tensile loadings."

Table 3.5. CMU material model selection

Mat. Model	Pros	Cons
5 Soil & Foam	Many inputs for accurate modeling	First geomaterial model; primitive
14 Soil & Foam w/ Fail.	Same as Mat 5 except has tension cutoff	
72 Con. Dam R3	Has the ability to generate material parameters; has many inputs	Parameter input is based on reinforced concrete and has not been validated for CMU
84 Win. Con w/ RE	Is smeared crack model	Built primarily for reinforced concrete section with many inputs for rebar
85 Win. Con.	Same as Mat 85	
96 Brittle Dam.	Simple input model with both shear and tension damage modeled; has been used recently to model CMU.	Built primarily for reinforced concrete section with many inputs for rebar

The CMU properties used in the suitability analyses were a unit weight of 96.8 lb/ft^3 (or 1.450x10^{-4} lb-s^2/in.^{4}), Poisson's ratio of 0.20, and ultimate compressive strength (f'_m) of 1290 psi. The density was reduced from 101 lb/ft^3 from material testing in the full-scale testing to account for the added volume of the model CMU block where the overall mass would not be affected. The reduction factor was the ratio of the volume of an actual CMU compared to a model CMU. The modulus of elasticity was 1,163,000 psi based on 900 f'_m given by American Concrete Institute (ACI) 530 (ACI, 2011), the tensile strength was 181 psi based on $6.7\lambda(f'_m)^{0.5}$ given by ACI 318 (ACI, 2008), and the shear strength was $2\lambda\,(f'_m)^{0.5}$ based also on ACI 318 (ACI, 2008). The following shows an input for Mat 96 Brittle Damage.

*MAT_BRITTLE_DAMAGE

mid	ro	e	pr	tlimit	slimit	ftough	sreten
1	1.4450E-04	1.163E+06	0.2	181	53.9	0.8	0.03
visc	fra_rf	e_rf	ys_rf	eh_rf	fs_rf	sigy	
104	0	0	0	0	0	0	

where mid is the material ID number, ro is mass density, e is Young's modulus, pr is the Poisson ratio, tlimit is tensile limit, slimit is the shear limit, ftough is the fracture toughness, sreten is the shear retention, and visc is the viscosity of the concrete, and all other parameter are not used or default.

Grout and mortar were modeled using the Mat 96 with the ultimate compressive strength and mass density changed to reflect their material properties. The mortar properties were a unit weight of 125 lb/ft^3 and an ultimate compressive strength of 3190 psi; the mortar's modulus of elasticity was the same as the CMU since 900 f'_m was based on the prism strength, and the tensile and shear limits were left the same since these will be modeled more explicitly in the bond modeling. The grout properties were a unit

weight of 125 lb/ft^3 and an ultimate compressive strength of 7000 psi (f'_g); the grout modulus of elasticity was given by 500 f'_g based on ACI 530 (ACI, 2011), and the tensile and shear limits were based on normal concrete limits for lighter weight concrete from ACI. All properties were based on the material tests from Davidson et al. (2011) or on design standards.

3.5.2 Reinforcement Material Model

The steel material properties were assumed to be elastic-perfectly plastic without strain hardening. This was done for ease of modeling. Mat 3 Plastic Kinematic was selected because it allows elastic-perfectly plastic stress-strain modeling and because it works with beam elements. The steel was simulated as standard Grade 60 reinforcement. The properties of the reinforcement are a unit weight of 490 lb/ft^3, a yield strength of 60 ksi, a Young's modulus of 29000 ksi, and a Poisson ratio of 0.30. The material properties were based on the industry standards not on the material testing from the dynamic testing. The following is a sample of the input for the reinforcing steel.

*MAT_PLASTIC_KINEMATIC_TITLE

mid	ro	e	pr	sigy	etan	beta
7	7.34E-04	2.90E+07	0.30	60000	0	0
src	srp	fs	vp			
0	0	0	0			

where mid is the material ID number, e is Young's modulus, ro is mass density, pr is the Poisson ratio, sigy is the yield stress, etan is the tangent modulus, and all other values are not used in the model.

3.5.3 Boundary Material Model

The boundary was assumed to be infinitely rigid. This was also done where the boundary will not have any effect on the results. Mat 20 Rigid was specifically formulated to keep the material rigid. The boundary was assumed to be made of steel with a unit weight of 490 lb/ft^3, a modulus of elasticity of 29000 ksi, and a Poisson ratio of 0.30. The following shows a sample input for Mat 20 Rigid.

*MAT_RIGID_TITLE

mid	ro	e	pr	n	couple	m	alias
6	7.34E-04	2.90E+07	0.30	0	0	0	
cmo	con1	con2					
0	0	0					
lco	or	a1	a2	a3	v1	v2	v3
0	0	0	0	0	0	0	0

where mid is the material ID number, e is Young's modulus, ro is mass density, pr is the Poisson ratio, and all other inputs are not used.

3.6 Element Modeling

The model used two distinctive element types, solid and beam. The solid elements were used to model CMU blocks, mortar joints, grout, and boundary supports. The constant stress element formulation was used to model all solids for most runs. This formulation is an eight-node, hexagonal brick element with single point integration. This was done because it vastly reduces the computational time and costs; the drawback was the model was less accurate than the fully integrated solid elements. The fully integrated S/R solid formulation was also used in some smaller models to accurately capture the stress and strain gradient over the CMU. The CMU were the only elements with the fully integrated formulation. The following show solid element inputs. The first is for constant stress solid elements, and the second is fully integrated solid elements.

```
*SECTION_SOLID_TITLE
     secid          elform          aet
       1               1              0


*SECTION_SOLID_TITLE
     secid          elform          aet
       1               2              0
```

where secid is the section ID, elform is the element formulation specification, and aet is the ambient element type.

Beam elements were used to model the steel reinforcement. The Hughes-Liu beam element formulation was used. This formulation takes into account both bending and axial actions. Even though steel reinforcement is not necessarily used in design with its individual moment-resistance and moment of inertia, this formulation takes into account the full-effect of the steel internal forces. In addition, the steel then can respond in dowel action which is carried through axial straining of the beam as the grout bends. The following shows the Hughes-Liu beam input for the model.

```
*SECTION_BEAM_TITLE
     secid        elform          shrf        qr/irid         cst       scoor        nsm
       2             1              1             2           1           0          0
       TS1          TS2            TT1           TT2        NSLOC      NTLOC
       0.2           0              0             0           0           0
```

where secid is the section ID, elform is the element formulation specification, shrf is the shear factor, cst is the cross section type (1 is tubular), nsm is the nonstructural mass per unit length, TS1 is the outer diameter, TS2 is the inner diameter, and all other inputs are either not used or are defaults.

3.7 Load Modeling

In loading of the walls, there are two major loadings, gravity loading and blast wave. The effects are modeled through various ways using load keyword cards in LS-DYNA.

3.7.1 Gravity Preloading

The gravity preload was used to generate the initial conditions due to self-weight. This was done easily by adding a body load in the downward direction using Load Body with the direction being in the vertical direction. The following shows the gravity preload input for the model.

```
*LOAD_BODY_Z
      lcid          sf        lciddr          xc          yc          zc         cid
         1           1             0           0           0           0           0
```

where lcid is the load curve ID, sf is the load curve scale factor, and all other are not used in the model. In order to use Load Body card, a load curve had to be defined; this was done by using the Define Curve card. The following is a sample input for the gravity curve.

```
*DEFINE_CURVE_TITLE
      lcid          sidr         sfa         sfo        offa        offo      dattyp
         1             0           1       384.6           0           0           0
        a1            o1
         0             0
      0.02             1
       1.0             1
```

where lcid is the load curve ID, sfa is the scale factor for the abscissa value, sfo if the scale factor for the ordinate value, offa is the offset for the abscissa value, offo is the offset for the ordinate value, a1 are the abscissa values, o1 are the ordinate values, and all other are not used in the model.

The curve provided a gradual increase in the gravity effect to allow for smaller stress gradients in the initial loading. The dynamic relaxation algorithms were not explicitly used in the model; these algorithms would generate damping forces to remove any movement at the beginning of simulation; however, the algorithms would cause the model to take longer to run and be more costly. Another way to allow dynamic relaxation was to not start the blast wave until the base reaction under gravity loading reached a stable oscillation. In order to accomplish this, a ramp function was used to decrease the initial oscillations. Figure 3.14 shows interface force of the verification wall with gravity preloading on it. It can be determined that the base reaction met a normal oscillation at 20 ms; this was confirmed by research which recommended 20 ms as well. In addition, the overall axial stress at the base was less than 30 psi which was about 2% of the masonry prism's strength.

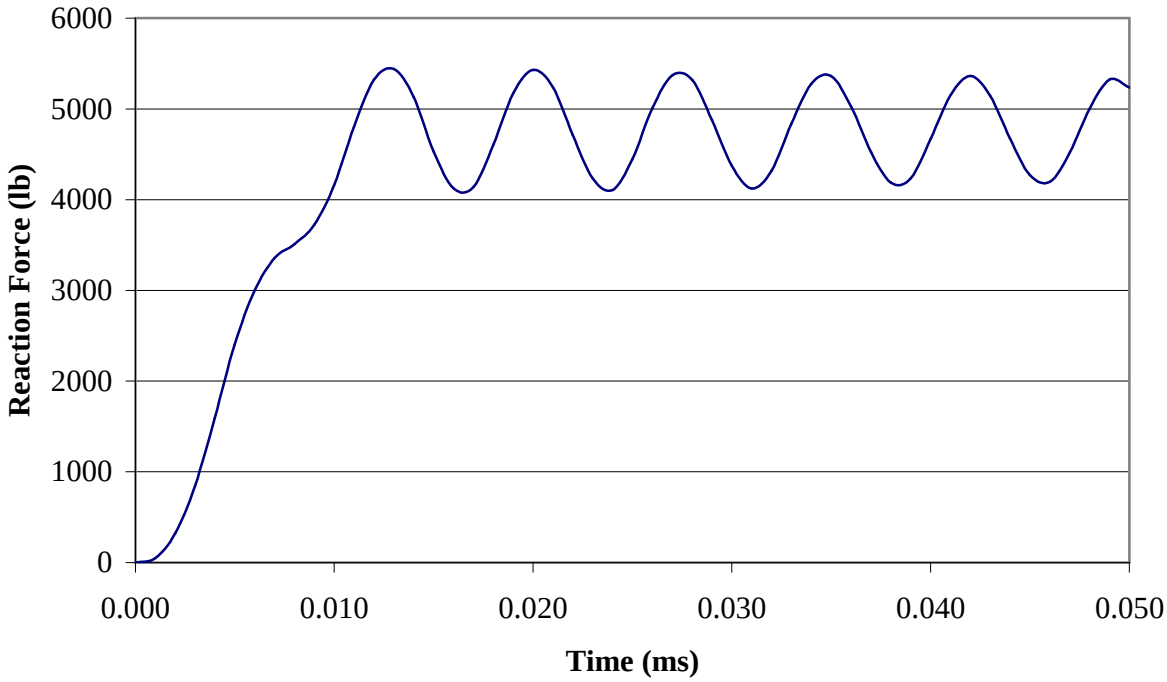

Figure 3.14. Base force of wall under gravity loading

3.7.2 Blast Loading

Blast loading can be applied in a few ways. The easiest is to use the Load Blast Enhanced card. This load card allows for simple inputs to generate a pressure-time curve that is applied on the wall. However, this method does not allow for direct control of the loading. The other way in which the blast loading can be carried out is by directly inputting the pressure values in Load Segment Set. This can be done to specifically control the pressure to match data from testing or to generate user specified loadings for analysis. A sample input of Load Segment Set is shown.

```
*LOAD_SEGMENT_SET
      ssid          lcid          sf          at
         1             3           1           0
```

where ssid is the segment set ID, lcid is the load curve ID, sf is the load curve scale factor, and at is the birth time of pressure.

3.8 Boundary Modeling

The boundary was modeled to allow one-way bending behavior of the wall; therefore, the boundary was modeled with rigid material model with all the degrees-of-freedom fixed; the rigid material model does not allow the boundary parts to deform. This prevents boundary's deflection from interfering with deformation of the wall. The wall rested on the boundary parts. Figure 3.15 shows the boundary members.

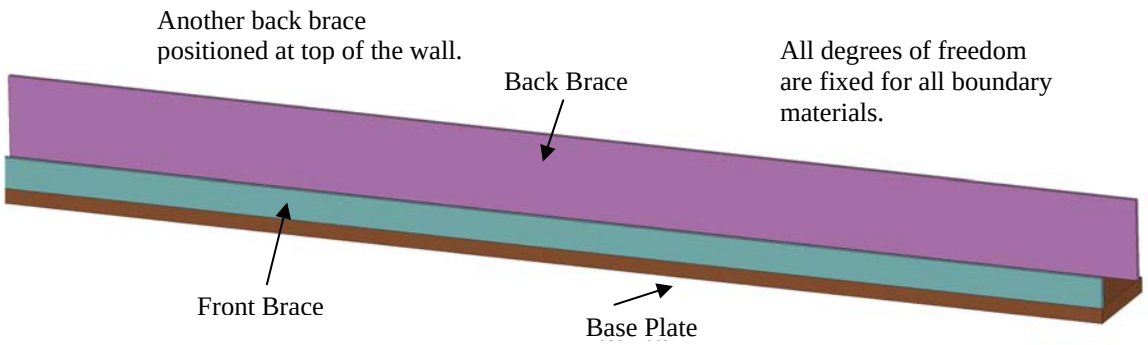

Figure 3.15. Boundary modeling

As can be seen in the figure, the boundary was simulated as a base plate and two braces, one at the top and one at the bottom. This was done in order to match the full-scale dynamic test as closely as possible. Two-way bending was not modeled as this would not provide any better understanding of the breaching phenomenon, and the common construction practice is to build the wall with only support at the top and bottom. The boundary restrains movement of the wall by causing added fixity at the bottom of the wall. This was done to keep the wall in the frame during the spring-back phase. The wall could freely rotate both at the top and bottom. The braces were offset from the wall by 0.05 in.; this kept the wall in the frame without causing problems with the calculations.

3.9 Contact Modeling

In order to accurately capture the response of a CMU, different contact definitions must be set-up. These include a mortar-block interface to properly represent the bond of the mortar to the CMU and a boundary-wall interface to properly contain the wall's movements. The following sections describe the modeling methods that were taken to properly model contact.

3.9.1 Mortar-Block Interface

The bond between mortar and blocks must remain intact until failure limits are reached. In order to do this, there are two modeling approaches. The first is to force the mortar and CMU to share nodes; in order to have bond failure, the mortar elements must have erosive properties built-in it to allow elements to be deleted when they reach limiting stress or strain values. The other way is to define a contact definition where nodes are tied together. The contact definition has a built-in failure criterion that allows the two surfaces to untie and slide independently of each other. Even though the former was cheaper and faster, the latter approach is used. This is because element erosion can change the mass of the system. Also, part of the shear resistance of the wall is provided by friction; therefore, even using the erosion method, a contact definition would have to be applied, and the contact surfaces would have to be adaptive to allow for erosion of elements.

LS-DYNA has several contact cards to allow for tying nodes together. Initially, Contact Tied Surface to Surface was used; however, this was changed to Contact Tiebreak Surface to Surface because it allows for friction sliding after ties are broken. Tiebreak Node to Surface was used because it allows for massively parallel processor runs. This contact definition allows for a Mohr-Coulomb failure surface characterized by

$$\frac{f_n^{NEN}}{NFLF^{NEN}} + \frac{f_s^{MES}}{SFLF^{MES}} > 1 \qquad (3\text{-}1)$$

where f_n = tension force in the model (if the stress is in compression, the value is zero.), $NFLF$ = tensile failure force, f_s = shear force in the model, $SFLF$ = shear failure force, and NEN and MES = exponent for normal force and shear force, respectively (normally

2). Once the equation is greater than one, the node is released and can slide. The tensile failure stress was the modulus of rupture for N Portland cement mortar from MJSC; the shear failure stress was a median stress from Atkinson et al. (1989). These stresses were multiplied by contact area of each element to transform the stress into a force. The contact definition allowed for friction. The static coefficient of friction between mortar and CMU was modeled as 0.8; the dynamic coefficient was 0.7. The coefficients of frictions are based on recommended values, and as shown in Browning (2008) the energy dissipation due to sliding was minimumal.

There were two mortar-block interfaces, contact at the head joints and one for contact at the bed joints; Figure 3.16 shows these contact surfaces. Each contact definition needed two segment sets, a master and a slave. The slave set for the head joints was the outer elements of the mortar that would be attached to the block in real construction; the master set was the heads of each block with the exception of the blocks on the ends that do not have mortar attached. The slave set for the bed joint interface was the bed joint mortar on one side; the master set was the top or bottom of the block that is on the same side of the slave set. The other side of the block and the mortar shared nodes; this removed the need for one more contact definition and made the models run quicker. A sample input of Contact Tiebreak Node to Surface is shown.

*CONTACT_TIEBREAK_NODES_TO_SURFACE

ssid	msid	sstyp	mstyp	sboxid	mboxid	spr	mpr
8	7	4	0	0	0	0	0
fs	fd	dc	vc	vdc	penchk	bt	dt
0.7	0.8	1	0	0	0	0	1.E+20
sfs	sfm	sst	mst	sfst	sfmt	fsf	vsf
1	1	0	0	1	1	1	1
nfls	sfls	nen	mes				
100	150	2	2				

where ssid is the slave set id, msid is the master set id, sstyp is the slave set type, mstyp is the master set type, fs is the static coefficient of friction, fd is the dynamic coefficient of frciton, dc is the exponential decay coefficient, bt is the birth time, nflf is the tensile failure stress, sflf is the shear failure stress, nen is the exponent for normal force, mes is the exponent for shear force, and all others are either not used or are default.

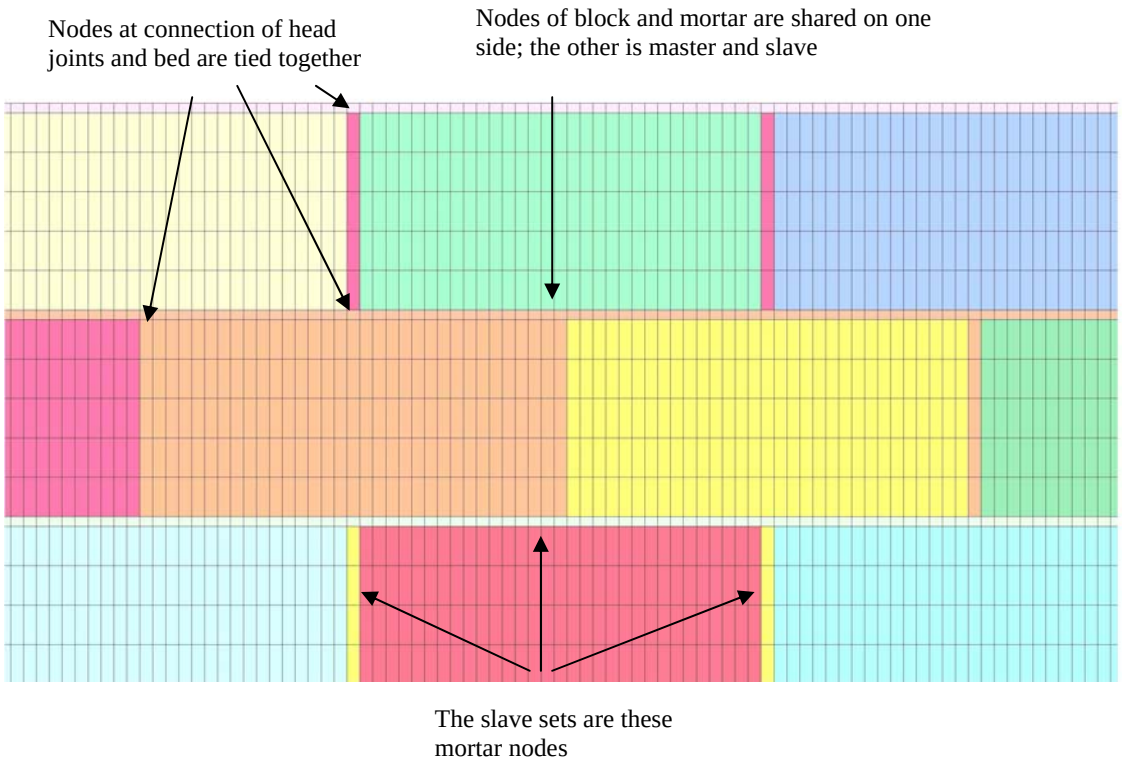

Figure 3.16. Mortar-block interface

3.9.2 Block-Boundary Interface

The interface between the boundary and the wall was necessary to allow the model to simulate the blast properly. This interface allowed frictional sliding and prevented penetration. Contact Automatic Surface to Surface allows for sliding without penetration. This contact definition also used segment sets, as well. The master surface

sets were the top of the base, the back of the bottom brace, and the front of the top brace. The slave surface set rested against the master sets; they were, in the same order as listed above, bottom of the bottom row of blocks, the back of the bottom row of blocks, and the back of the top row of blocks. A sample input for this contact definition is shown. Figure 3.17 shows the boundary-block interface.

*CONTACT_AUTOMATIC_SURFACE_TO_SURFACE_ID

ssid	msid	sstyp	mstyp	sboxid	mboxid	spr	mpr
8	7	0	0	0	0	0	0
fs	fd	dc	vc	vdc	penchk	bt	dt
0.8	0.6	1	0	0	0	0	1.E+20
sfs	sfm	sst	mst	sfst	sfmt	fsf	vsf
1	1	0	0	1	1	1	1

where ssid is the slave set id, msid is the master set id, sstyp is the slave set type, mstyp is the master set type, fs is the static coefficient of friction, fd is the dynamic coefficient of frciton, dc is the exponential decay coefficient, bt is the birth time, and all others are either not used or are default.

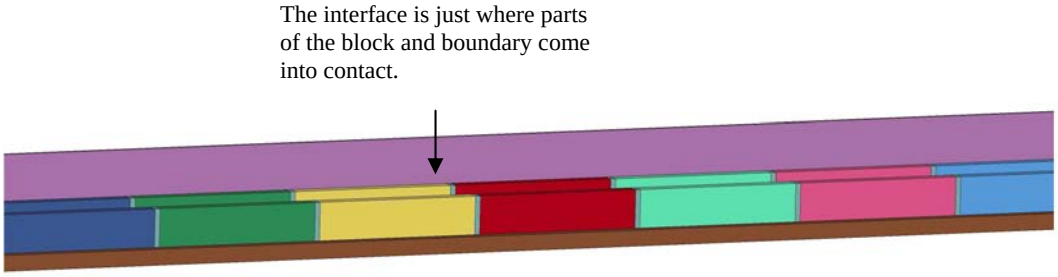

Figure 3.17. Boundary-block interface

3.10 FEM Validation

In order to trust the results of any of the finite element model, a standard had to be set. This standard is the response of Panel 2 from all three blast tests carried out by AFRL. This wall was built using 8-in. CMU laid with 7 blocks horizontally and 17

courses vertically; Figure 3.1 gives the wall layout including placement of reinforcing and grouting; in addition, Figure 3.2 gives detailed side view of the wall giving information on the support conditions, reinforcing, splicing, and other construction details. Figure 3.18, as seen below, describes the instrumentation used in the AFRL dynamic tests.

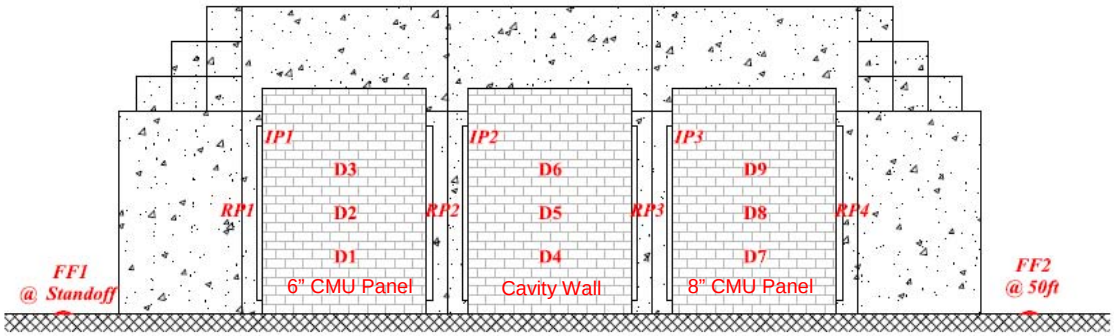

Figure 3.18. Test set-up and instrumentation position

During testing both free field (FF1 and FF2) and reflected pressures (RP1–RP4) were taken; the reflected pressure were averaged across the four gauges, and reflected impulses were calculated. Dynamic deflections gauges (D1-9) were used to find deflections at the mid-height and quarter-heights of the walls. The normalized pressures for Test 1 (T1), Test 2 (T2), and Test 3 (T3) can be seen in Figure 3.19, and the normalized impulse is shown in Figure 3.20.

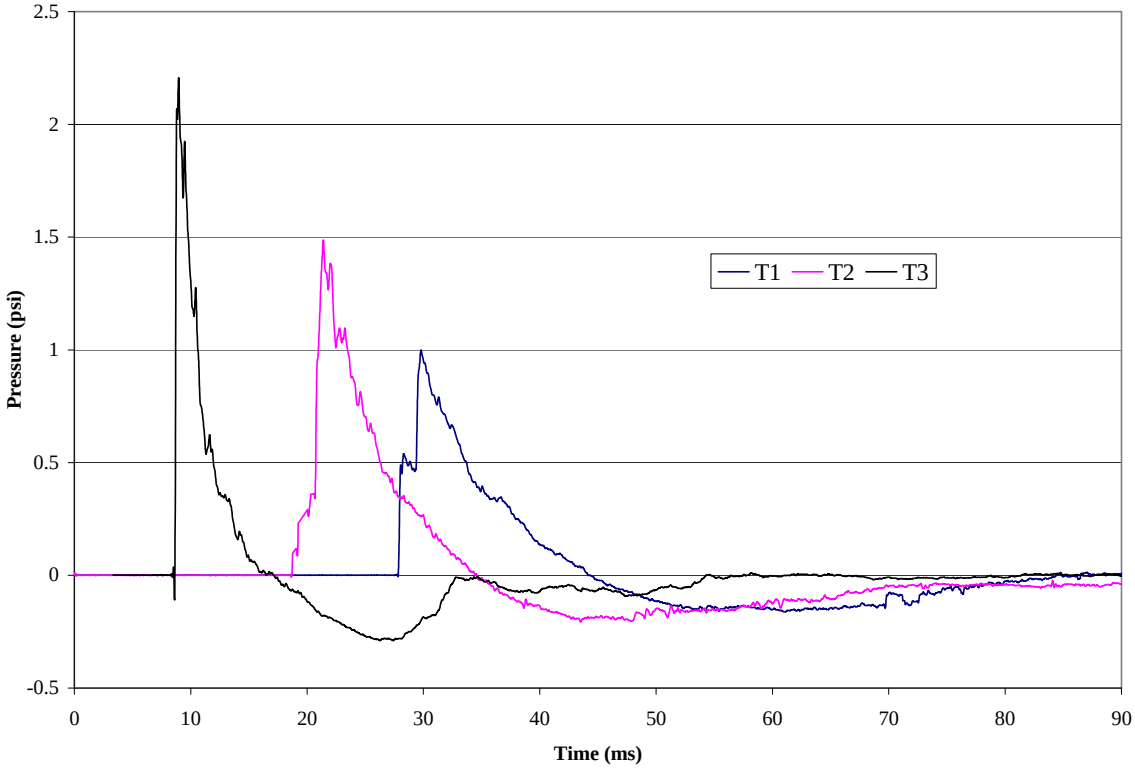

Figure 3.19. Normalized reflected pressure from dynamic testing

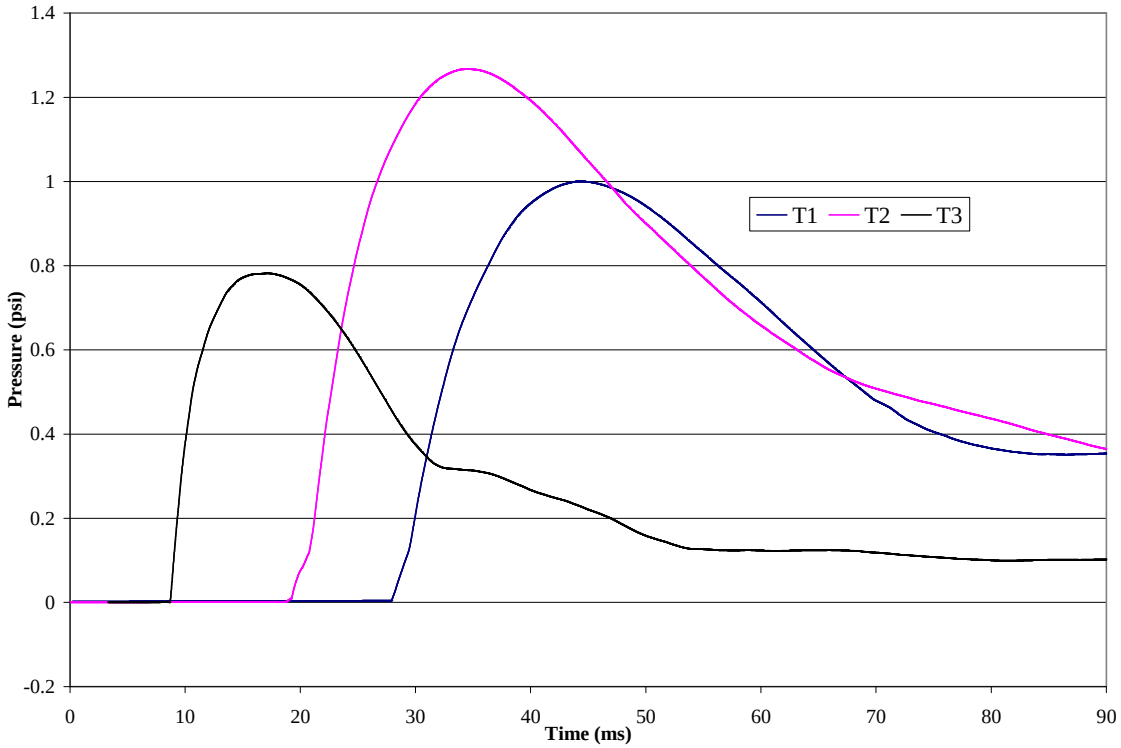

Figure 3.20. Normalized impulse from dynamic testing

The validation of the finite element model involved the model having similar deflected shape or breaching pattern within a desired error range, having a similar deflection-time response, and having matching breaching stress patterns. Having similar deflected shape is hard to compare since the testing occurs quickly without a true way to capture a good representation of deflected shape. As a substitute, high-speed footage from inside a blast chamber is used. Since the 8-in. CMU panel was used for comparison to finite element model results; the deflection of instruments D7, D8, and D9 are the only ones of interest. These points coincide with the quarter-points and halfway point on the wall.

Figure 3.21 shows several video captures of the dynamic testing from behind the wall of Panel 2 from Test 1. Figure 3.22 shows several screen captures of the finite element model run of Test 1.

a.) 

b.) 

c.) 

d.) 

Figure 3.21. Video captures of panel 2 during test 1 at a.) 10 ms, b.) 21 ms, c.) 41 ms, and d.) 84 ms after loading starts

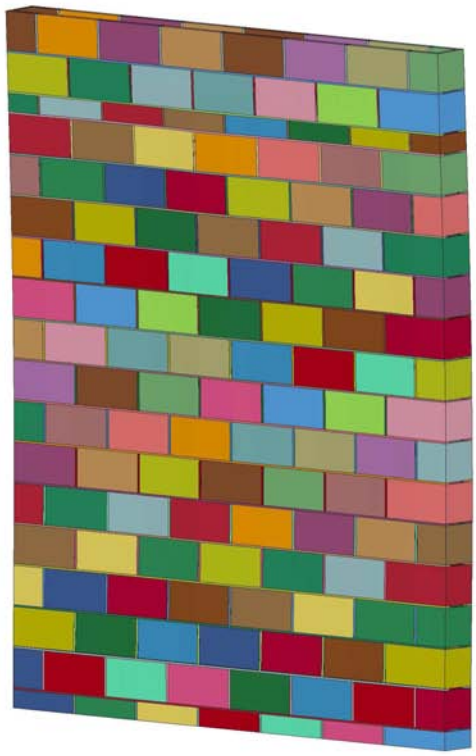

a.)

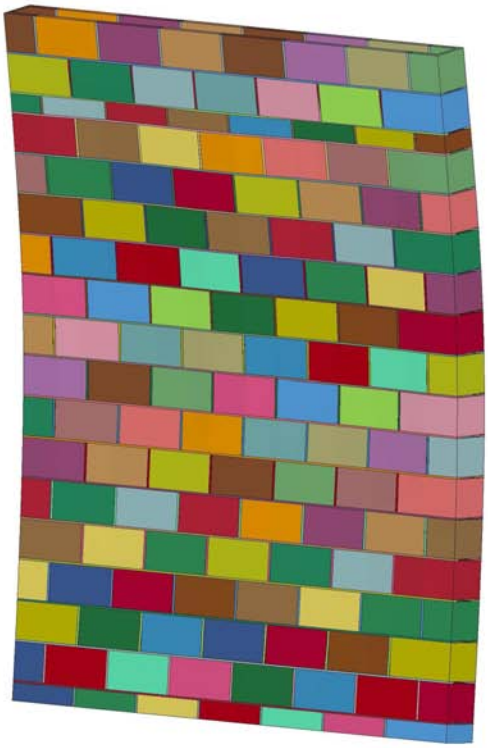

b.)

c.)

d.)

Figure 3.22. Screen captures of FEM of panel 2 test 1 at a.) 10 ms, b.) 21 ms, c.) 41 ms, and d.) 84 ms after loading starts

As can be seen, the deflected shape of the finite element model and the dynamic testing correlate well for Test 1. Both formed cracks around the mid-height of the wall and around the quarter-point of the walls. The wall from the dynamic testing did show signs of breaching; however, the breach was small and did not break all the way through the wall. The finite element pictures shown have some plastic strain in a fringe contour around the border of the grout columns, but this was minimal compared to other model runs. (Plastic strain is any strain that is not described by a linear elastic, stress-strain relationship such as yielding, rupture, or crushing.) Figure 3.23 shows the deflections-time graphs of the dynamic testing and FEM for the quarter-points and mid-point of the wall. The three deflections match up well between the FEM and the full-scale testing. The FEM is less stiff at the beginning of the test but tends to have greater stiffness later in the simulation. This difference in stiffness is accounted for by not correctly modeling the boundary conditions. However, the difference of overall maximum deflections between FEM and full-scale testing is low.

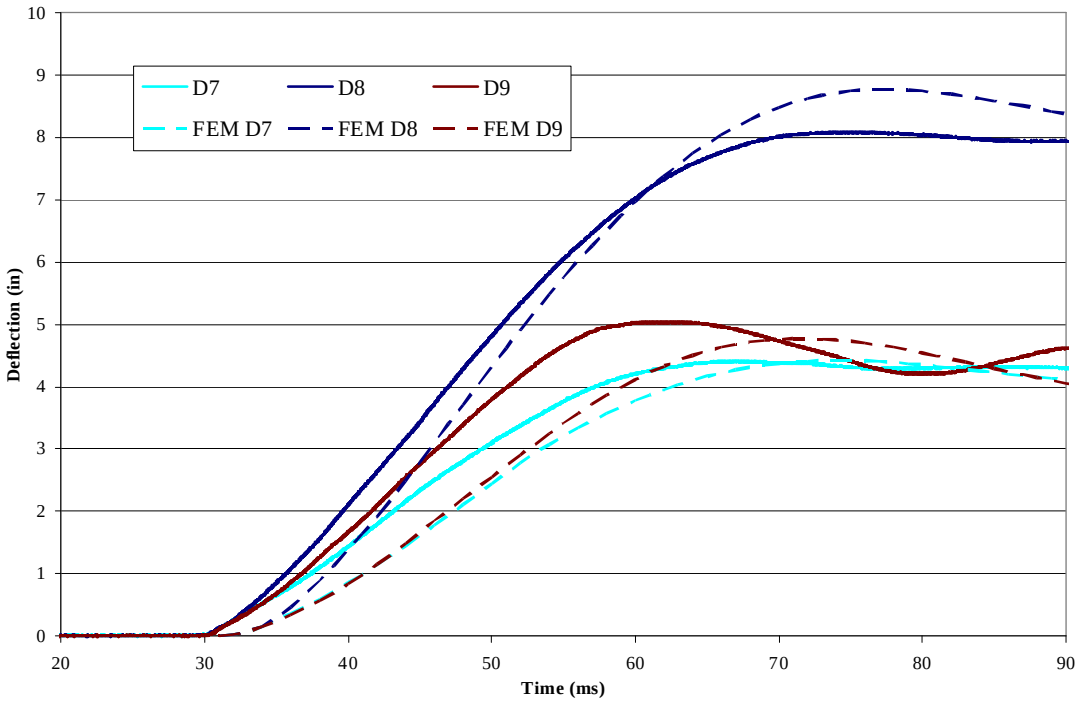

Figure 3.23. Deflection of panel 2 and of FEM from test 1

Figure 3.24 shows several video captures of the dynamic testing from behind the wall of Panel 2 from Test 2. Figure 3.25 shows several screen captures of the finite element model run of Test 2.

a.) 

b.) 

c.) 

d.) 

Figure 3.24. Video capture of panel 2 during test 2 at a.) 10 ms, b.) 19 ms, c.) 43 ms, and d.) 76 ms after loading starts

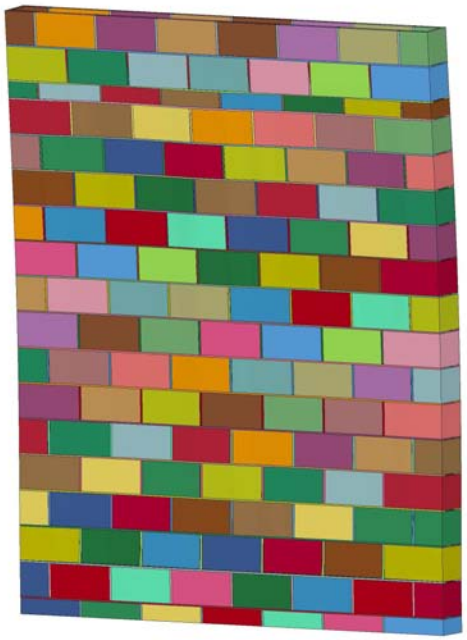

a.)

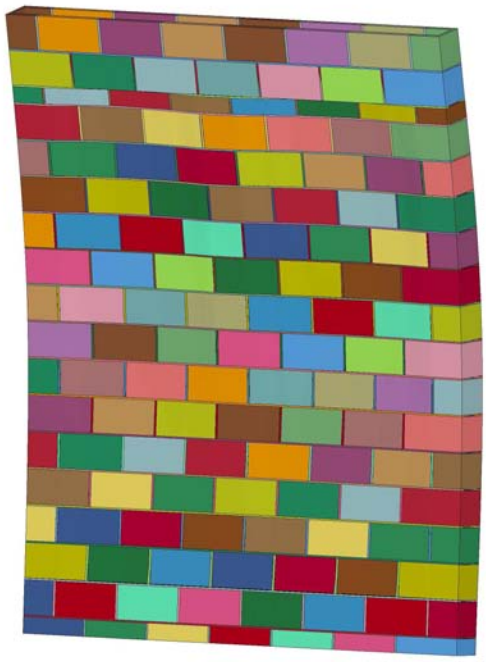

b.)

c.)

d.)

Figure 3.25. Screen captures of FEM of panel 2 test 2 at a.) 10 ms, b.) 19 ms, c.) 43 ms, and d.) 76 ms after loading starts

As can be seen, the FEM's deflected shape does not match with the deflection of the dynamic test. This is because the FEM does not breach, and the dynamic testing does. The model uses continuum elements that will not allow deletion of the element or cracking; the element does allow for plastic strain. This could have been forced by using erosive elements to model the CMU, but this would not have helped in the understanding of the breaching phenomenon. The breaching is captured in the FEM model by plastic strain. Shear hinges form at the boundary of the grout columns which would match cracking and breaching in a brittle material. (Shear hinges are an analytical tools used to understand when ductile material fail in shear; they allow for a constant strength while allow for progressive shear damage such as a plastic hinge in flexure.) Figure 3.26 shows a cross-section of the wall around mid-height 70 ms after the blast. Even though the cross section seems to show a flexural action of the faceshell, by this time in testing the block had sheared off. Also, the breaching pattern from the dynamic testing also is matched by the stress resultant in the FEM. Three stress contours occurring 1 ms after loading is shown in Figure 3.27. The element formulation did allow plastic strain. The plastic strain gradient right after the blast is also shown in Figure 3.27.

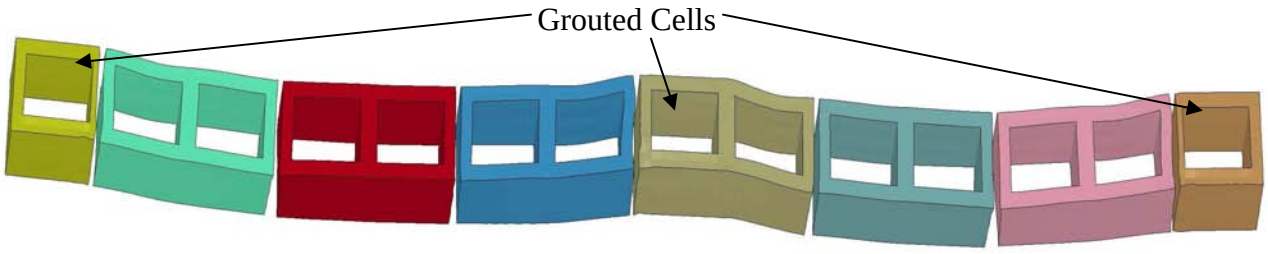

Figure 3.26. Cross-section of FEM

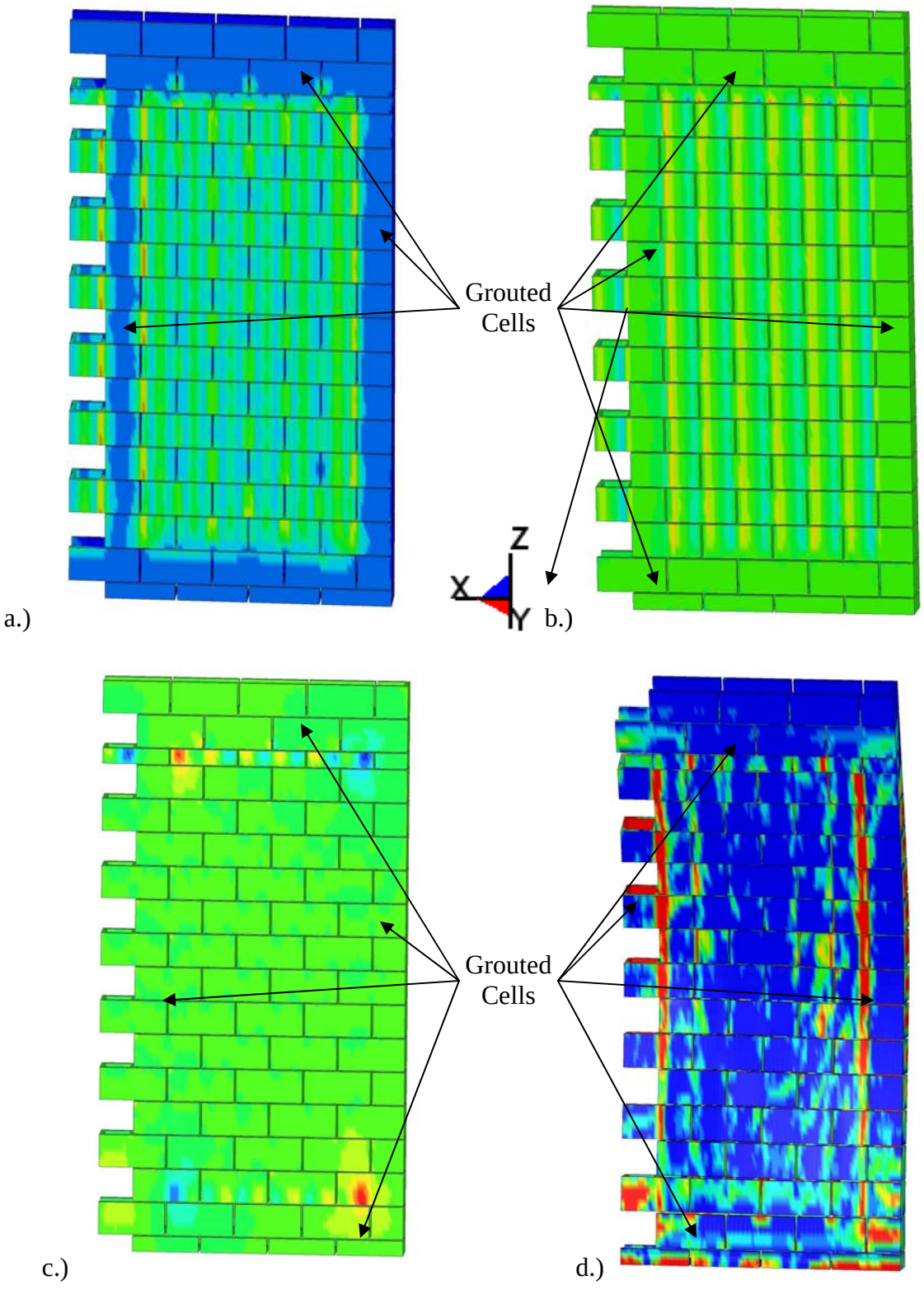

Figure 3.27. Stress Contours for FEM 1 ms after Loading: a.) Effective Stress, b.) XY-Shear Stress, c.) XZ-Shear Stress, and d.) Plastic Strain

Figure 3.27a shows the effective stress contour (Effective stress is stress combination based on von Mises stress calculations.) on the wall immediately following the blast wave hitting the wall. This contour plot shows there is a high concentration of stress along the boundary of grout columns. This is affirmed by the contour plot of xy-stress (b.), which also shows that there are high stresses along the web lines for blocks between grout cells. The high stress locations do not appear in the grout columns. The contour plot for xz-stress shows that there are also high stress localizations at the boundary of the bond beams at the top and bottom of the wall. These shear stress localizations caused the breaching in the full-scale test. Finally, the contour plot of plastic strain shows that there is plastic strain at the boundary of the grout columns. This plastic strain shows up as shear hinges in the FEM, as seen in Figure 3.26.

Finally, the deflection-time plot for the testing and FEM is shown in Figure 3.28.

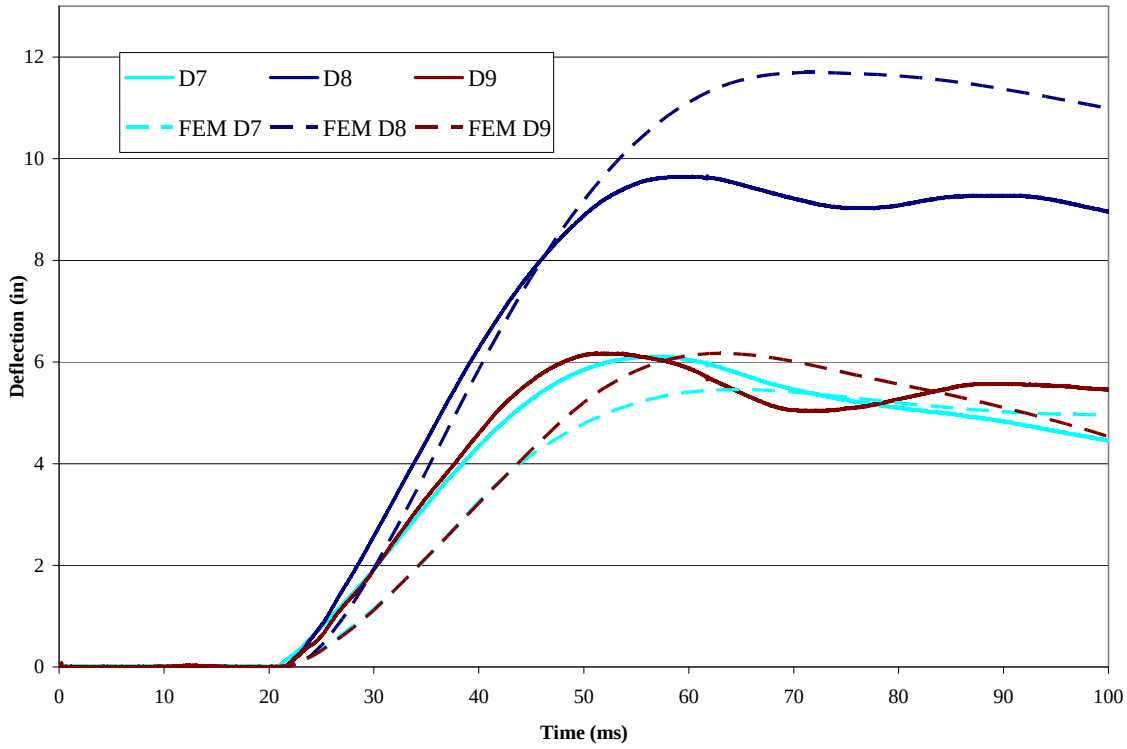

Figure 3.28. Deflection of panel 2 and of FEM from test 2

The FEM's deflection and full-scale test's deflection does and does not match. The maximum deflections for the quarter points of the wall are similar; however, at mid-height the maximum deflection of the FEM is higher. This was because the full-scale testing breached venting some of the pressure. Breaching also allowed the wall to dissipate the energy applied to the wall that the FEM cannot perform. The FEM model is stiffer than the full-scale test as well.

Panel 2 from Test 3 had very heavy damage with large sections of the wall blowing out breaching into the testing chamber. Since the FEM did not capture the breaching any better than the Test 2 model did, the video captures and screen captures are not shown. However, the FEM does show a better match of deflections. The deflections of the full-scale testing and dynamic testing are shown in Figure 3.29.

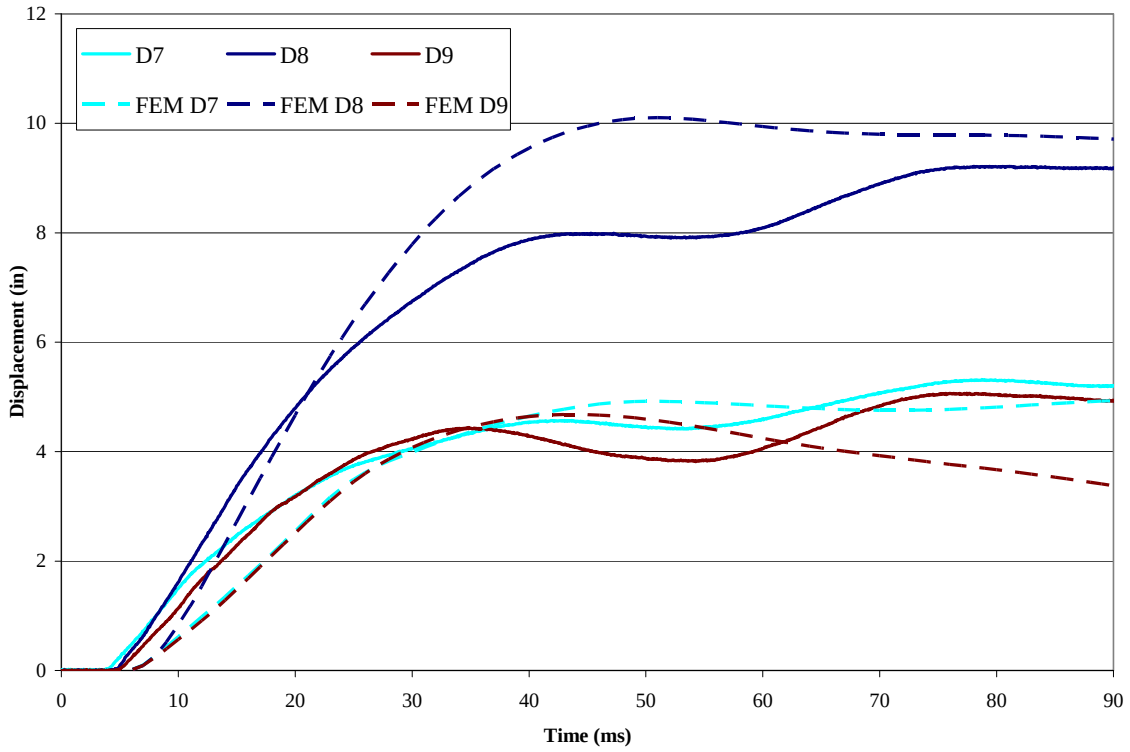

Figure 3.29. Deflection of panel 2 and of FEM from test 3

The deflection-time graph shows that the quarter points' deflection matched up well. However, the midpoint deflection for the FEM is much higher. This can be attributed to venting of the pressure caused by breaching as well as the energy dissipation caused by breaching. For all three data points, the FEM shows the same stiffness problems as in the other testing.

For all three comparisons, part of the difference between the deflections can be attributed to not modeling the boundary exactly the same as the full-scale tests. In the full-scale test, dowel rods inserted into the grout along the base of the wall provide a semi-fixed boundary condition. The FEM did provide a limited amount of fixity by having a front and back brace limit rotation of the bottom; however, this only occurred after the wall rotated. Another explanation for the differences is that basic design

material parameters were used instead of parameters established by material testing. With that in mind, Table 3.6 shows the maximum deflections for all three full-scale tests with a comparison to the appropriate FEM.

Table 3.6. Maximum deflection for test 2 and FEM

	Test 1			Test 2			Test 3		
	Full-Scale	**FEM**	**Percent Diff.**	**Full-Scale**	**FEM**	**Percent Diff.**	**Full-Scale**	**FEM**	**Percent Diff.**
D7	4.414	4.426	0.3%	6.121	5.459	10.8%	5.678	4.951	12.8%
D8	8.093	8.777	8.4%	9.663	11.694	21.0%	9.848	10.106	2.6%
D9	5.044	4.777	5.3%	6.179	6.170	0.1%	5.127	4.681	8.7%

Since there was less than 10% error for seven out of nine points of the deflections and less than 25% error for all, the deflections matches well between the FEM and full-scale testing. Since the breaching pattern is similar, the deflections are similar, and the deflected shape is similar, the FEM is valid for investigating the effects of shear breaching of CMU wall subjected to blast loading.

3.11 FEM Results and Suitability Study of Breaching

Having validated the modeling approach, a short parameter variability study was conducted to understand the variables in breaching of the CMU. In order to understand this, several FEM were created ranging from a single block to a full wall. The analyses were used to understand (1) time of response, (2) the change in the stress' magnitudes with a change in wall geometry, (3) a change in the stress' magnitude with a change in material properties, (4) a change in the stress' magnitude with a change with loading, and (5) a change in the stress' magnitude with the addition of grouting.

Analysis showed that the time of response for high local shear occurred in the first few milliseconds after the pressure is applied. This is shown in contour plots for out-of-plane (defined earlier as XY-Shear Stress) shear stress and effective stress for the verification wall (Figure 3.30 and Figure 3.31) and for a single block (Figure 3.32 and Figure 3.33). This wall and block was loaded using the pressures from Test 2. Figure 3.34 and Figure 3.35 shows a plot of out-of-plane shear stresses for the single block model over time. The stresses were found at the corners for both the backside and front-side of the front face.

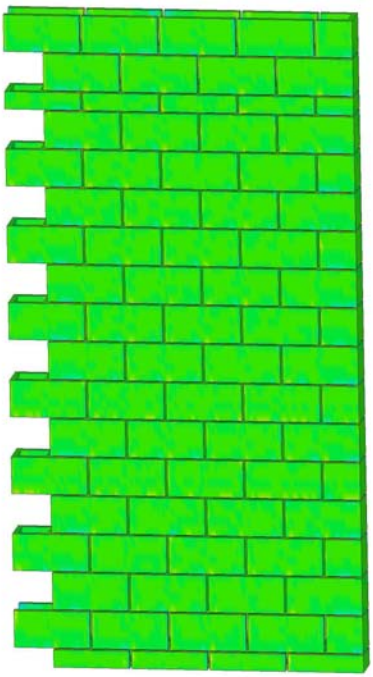

(0 ms after blast)

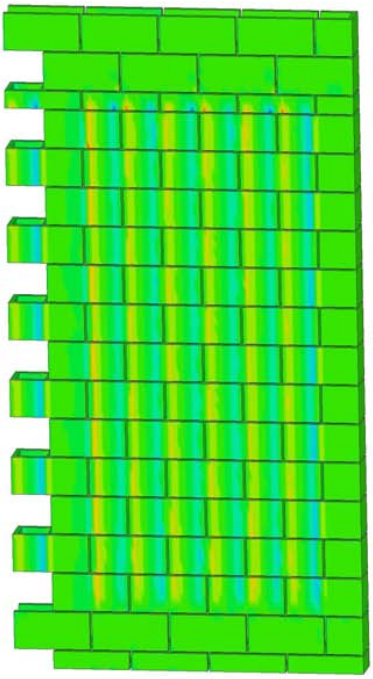

(1 ms after blast)

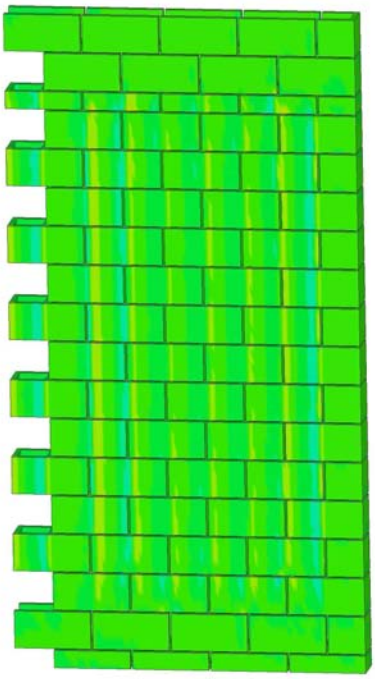

(2 ms after blast)

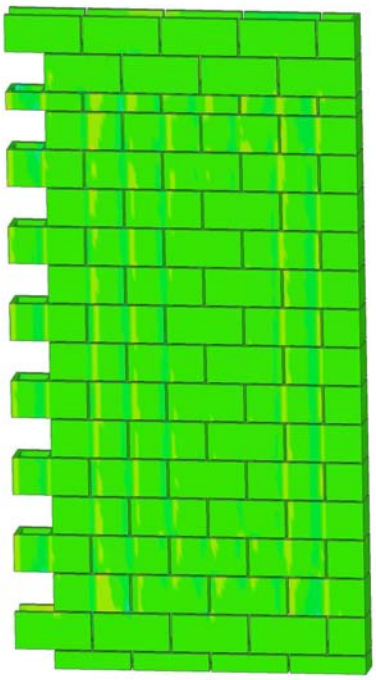

(3 ms after blast)

Figure 3.30. Contour plots of out-of-plane shear stress at various times

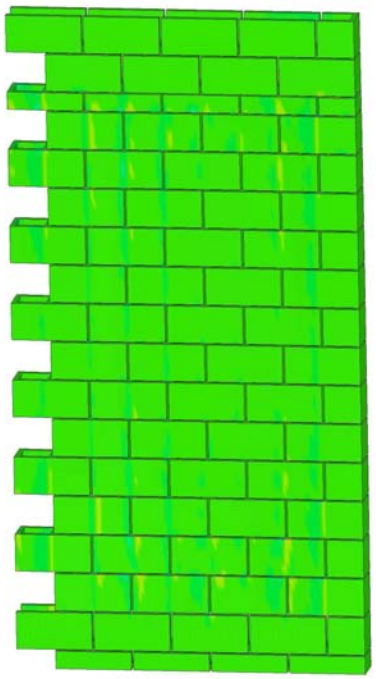

(5 ms after blast)

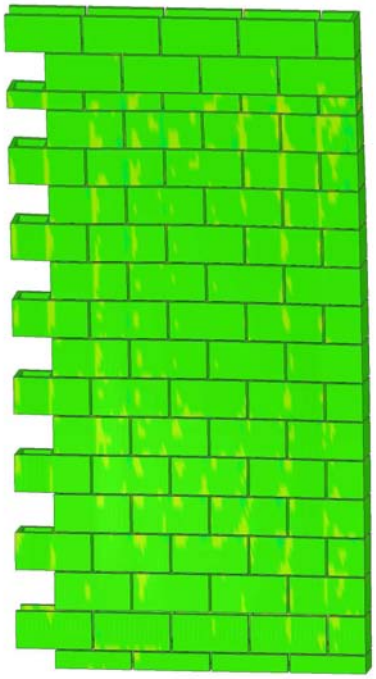

(10 ms after blast)

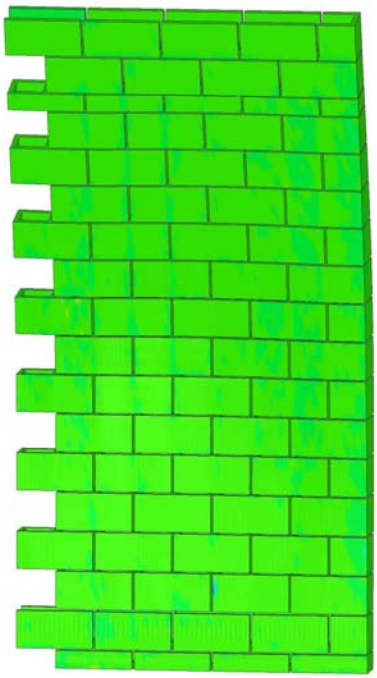

(20 ms after blast)

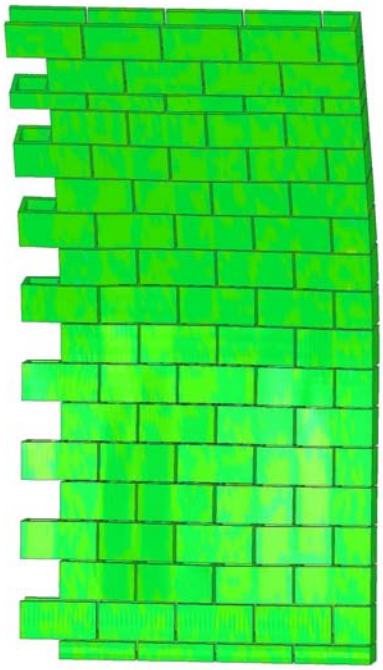

(50 ms after blast)

Figure 3.30. Contour plots of out-of-plane shear stress at various times

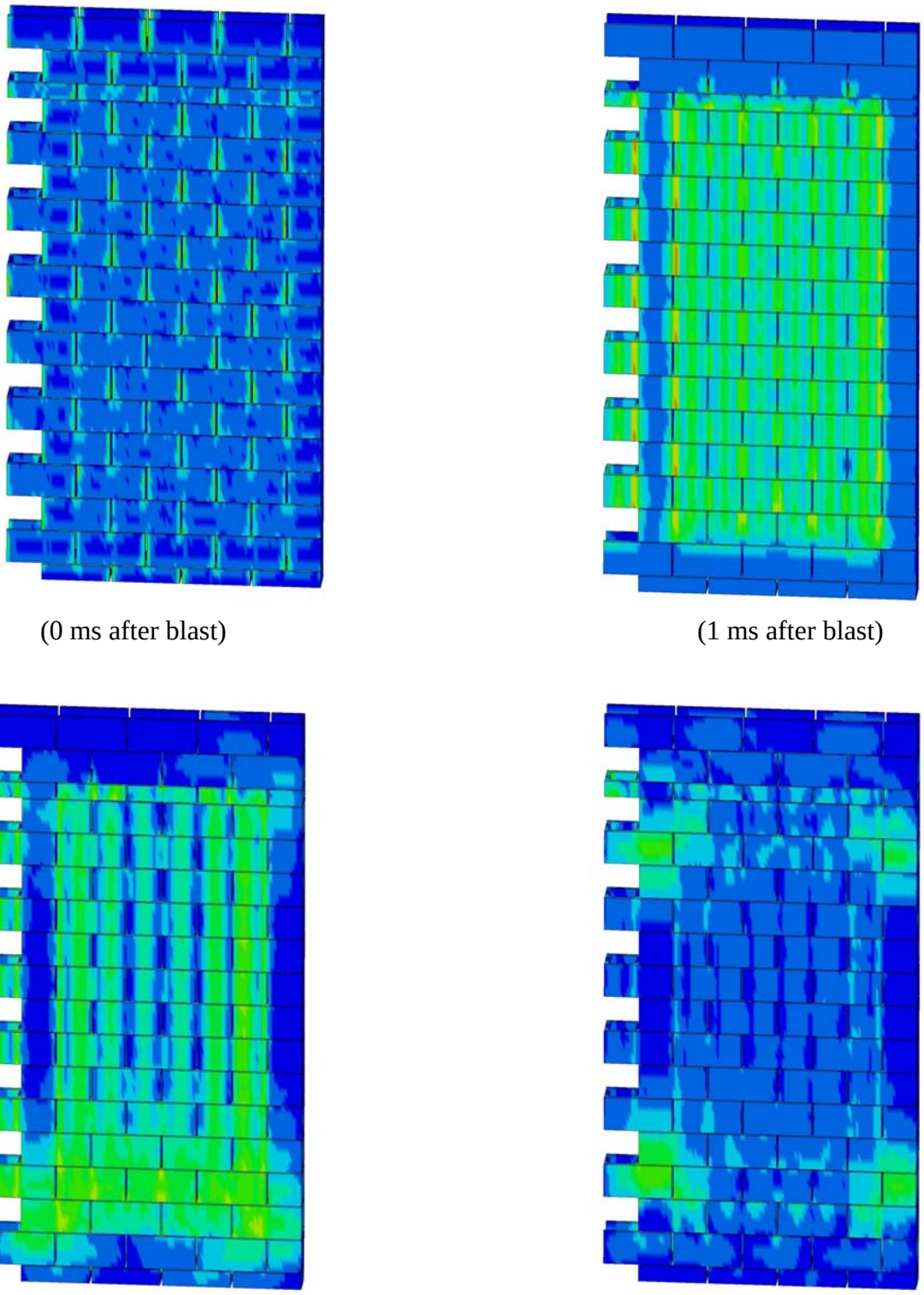

(0 ms after blast) (1 ms after blast)

(2 ms after blast) (3 ms after blast)

Figure 3.31. Contour plots of effective stress at various times

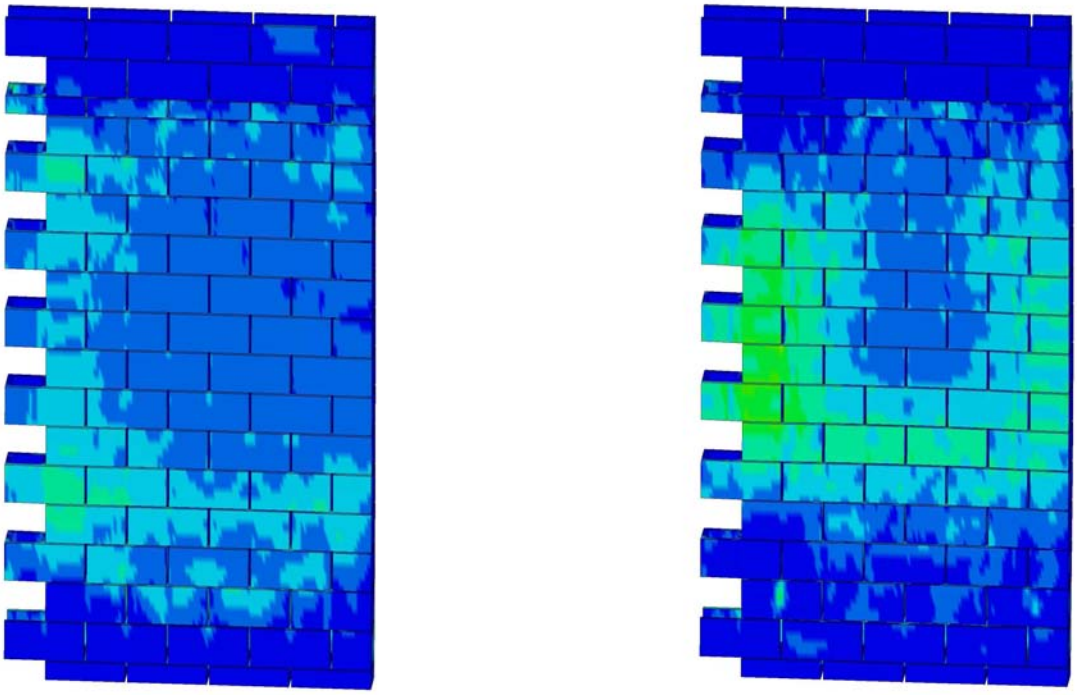

(5 ms after blast) (10 ms after blast)

Figure 3.31. Contour plots of effective stress at various times

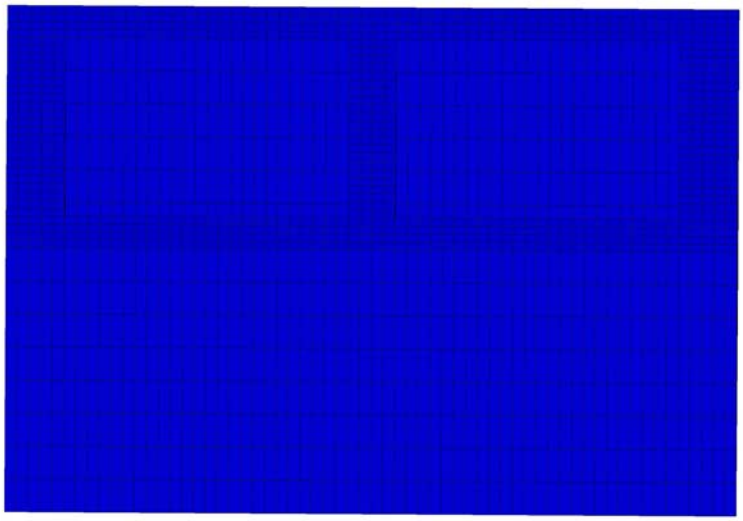

(0 ms after blast)

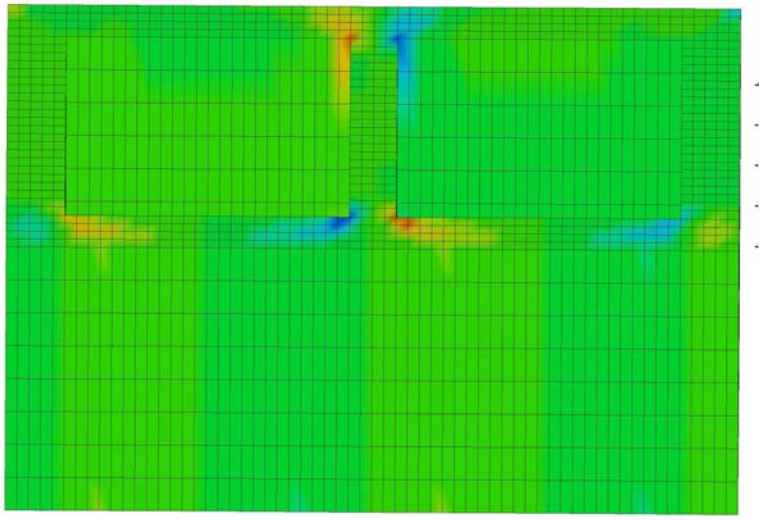

(1 ms after blast)

Figure 3.32. Contour plots of out-of-plane shear stress at various times

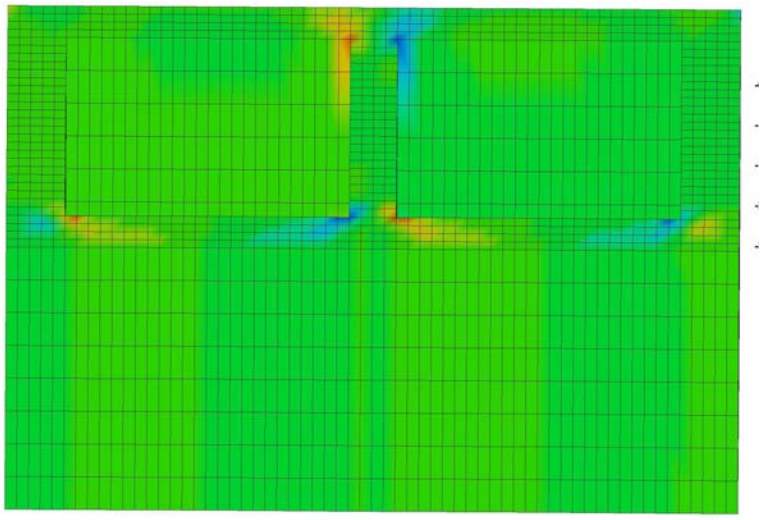

(2 ms after blast)

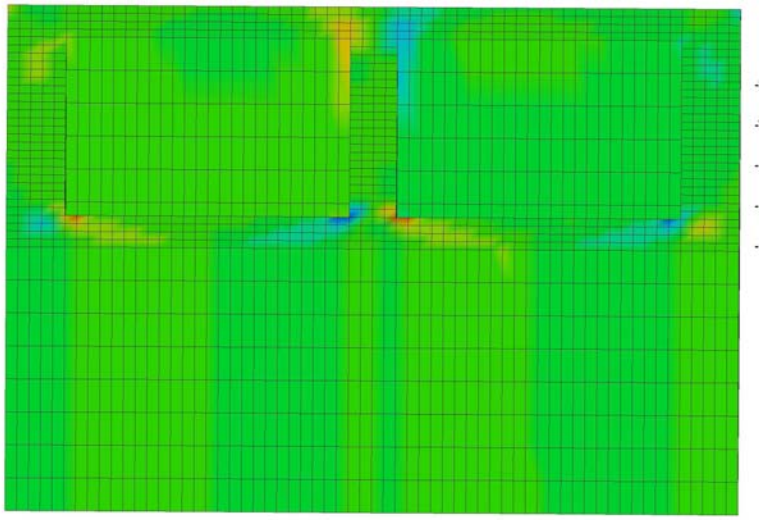

(5 ms after blast)

Figure 3.32. Contour plots of out-of-plane shear stress at various times

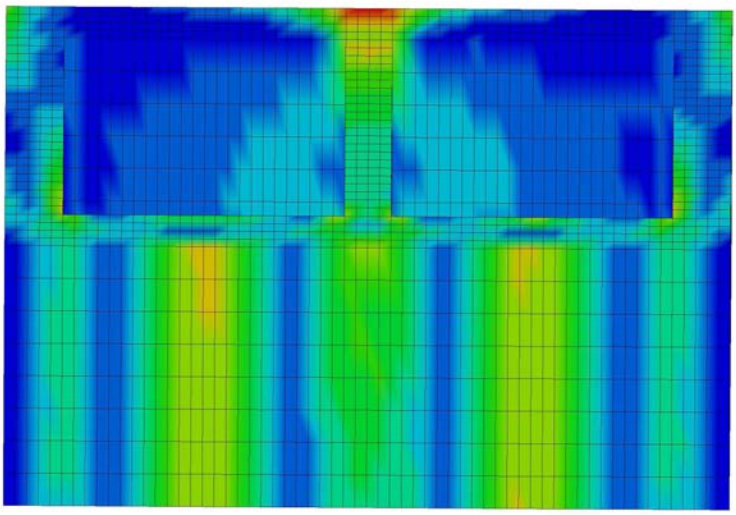

(1 ms after blast)

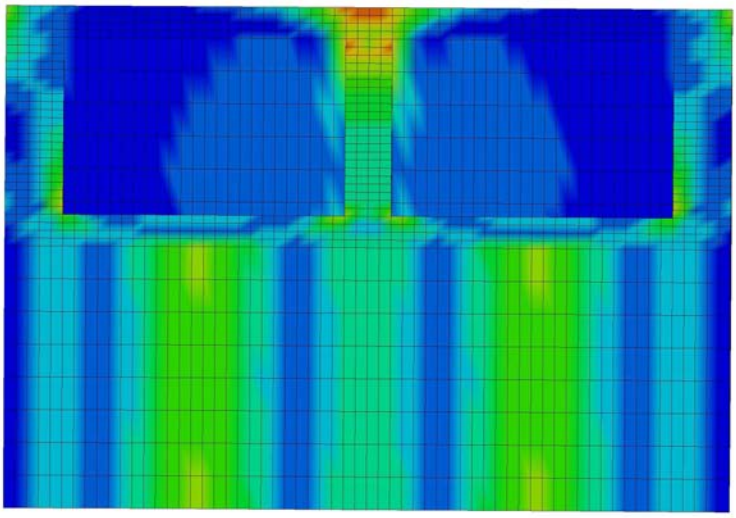

(2 ms after blast)

Figure 3.33. Contour plots of effective stress at various times

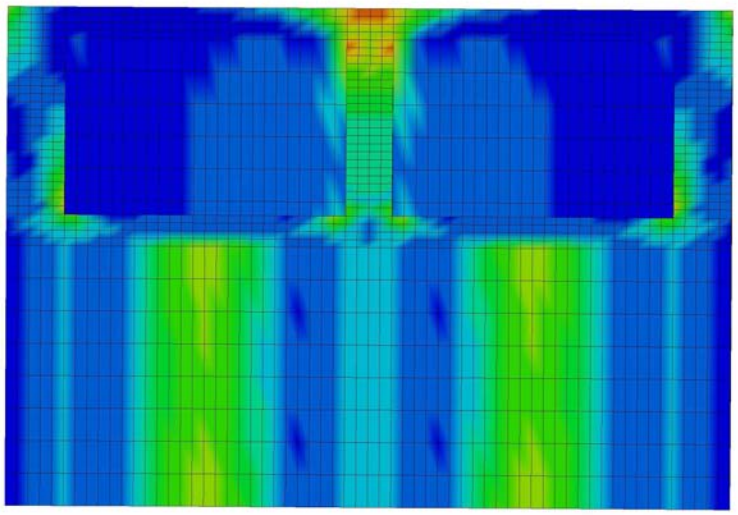

(3 ms after blast)

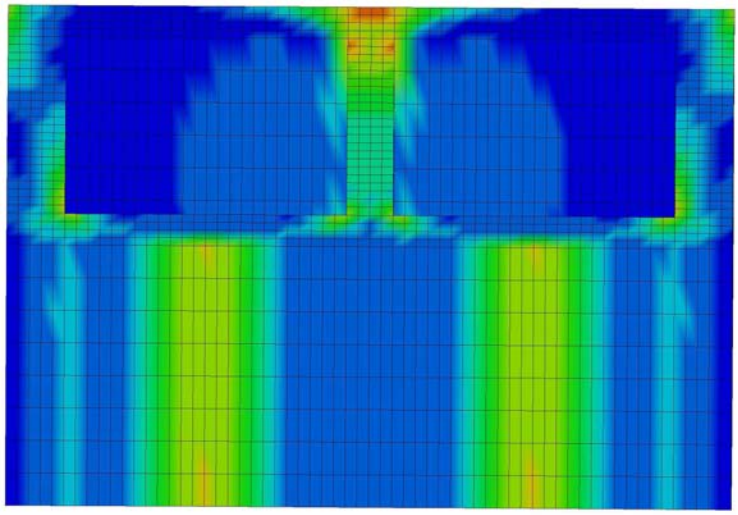

(5 ms after blast)

Figure 3.33. Contour plots of effective stress at various times

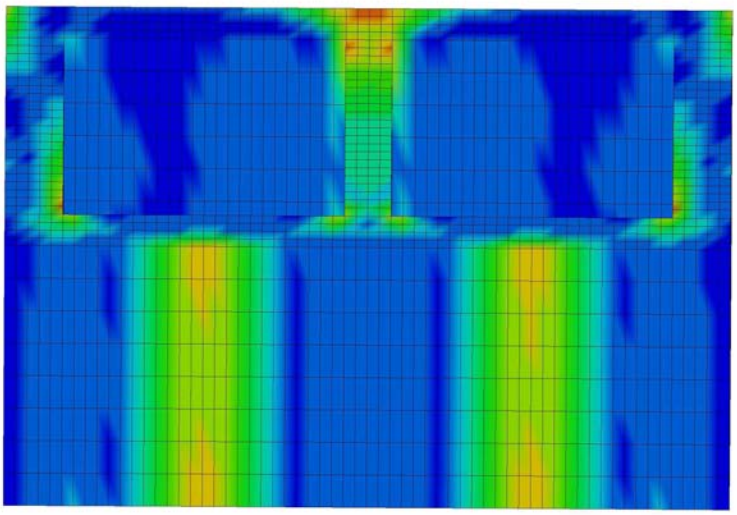

(10 ms after blast)

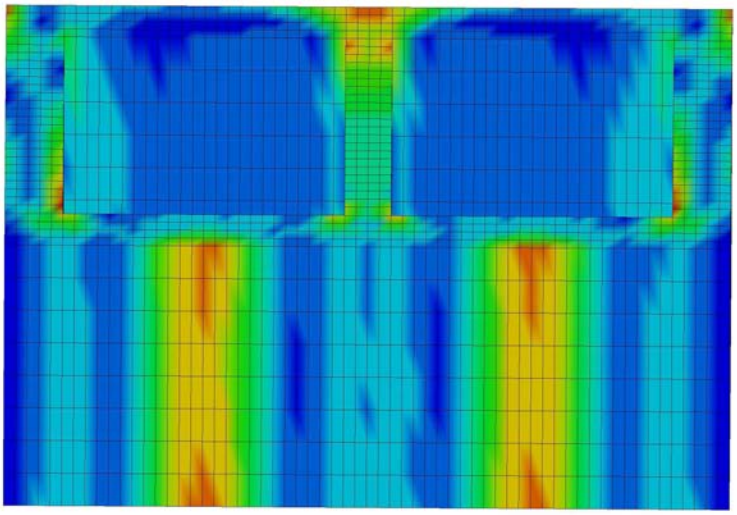

(20 ms after blast)

Figure 3.33. Contour plots of effective stress at various times

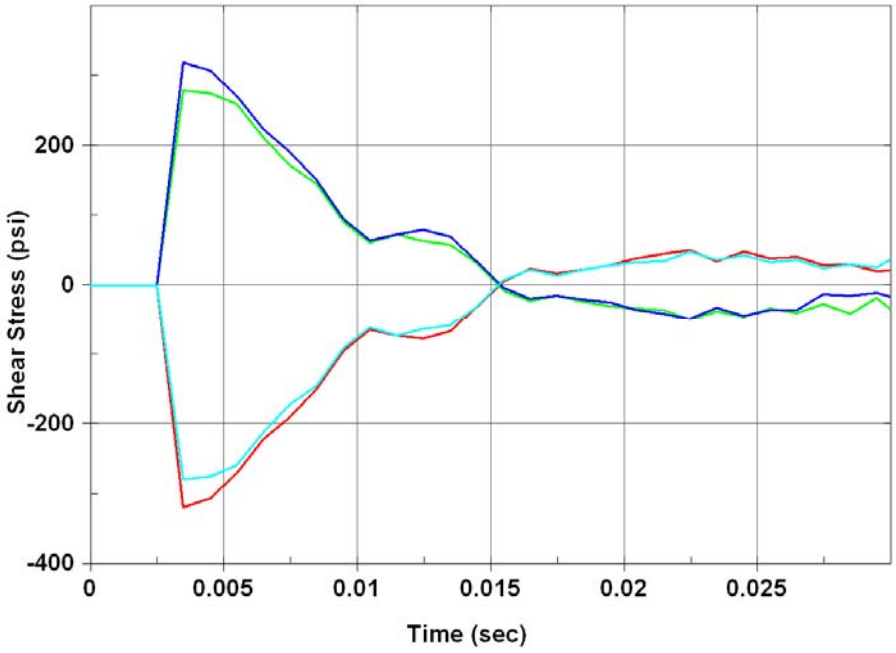

Figure 3.34. Plot of out-of-plane shear stress vs. time

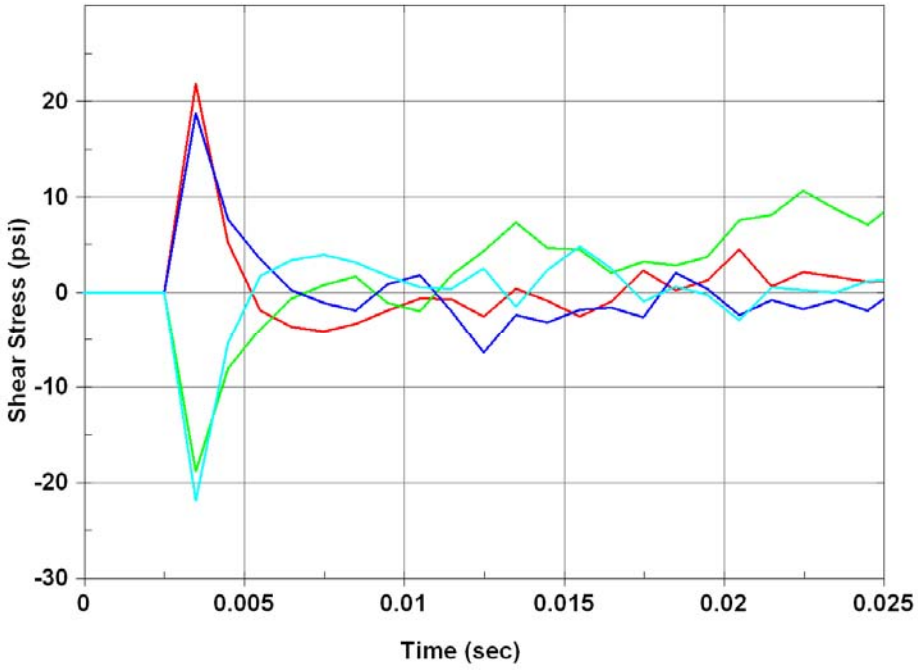

Figure 3.35. Plot of effective stress vs. time

The contour plots of a single block show that as the initial loading hits there was high shear localization at the reentrant corners of the blocks, and as the loading was continued the shear forces diminish as flexural response takes over. The flexural

response began to occur in 3 to 4 ms after the initial loading for the single block and fully develop over the rest of the testing as seen in the effective stress plots at 10 and 20 ms. The plots of the shear stress on the wall show the same response except the shear response lasts a little longer. The graphs show that as the blast wave hits the shear stress is high and almost instantly diminishes and never reaches the same magnitude. Therefore, the shear loading time of response occurs very quickly before any flexural response can occur; this is in the first 5 ms.

The next task was to find how the wall's overall geometry affects the location and maximum value for the shear stresses. In order to do this, several models were built starting with only one block and continuing building block by block to 10 rows and 10 courses. These models all implored rigid roller supports at the top and bottom. The peak pressure, loading duration, contact modeling, and material properties are the same for all models where the only variable is the wall's geometry. Table 3.7 and Table 3.8 display the peak out-of-plane stress and the peak effective stress for the loading time displayed in the contour plots. Figure 3.36 shows the out-of-plane stress the maximum stress of the reentrant corners of blocks over the period of the analysis. Figure 3.37 shows same as Figure 3.36 except it displays the effective stress for the models.

Table 3.7. Maximum out-of-plane shear stresses of various geometries of walls

		XY Stress (psi)						
		Columns						
		1	2	3	4	5	7	10
Rows	2	244	252	247	250	257	255	249
	3	252	276	251	252	252	252	252
	4	255	260	259	260	259	260	260
	5	255	280	259	258	254	254	255
	7	252	258	254	257	259	253	253
	10	255	266	259	259	259	259	259
	12	257	273	265	260	260	264	264
	15	260	280	270	261	260	270	269

Table 3.8. Maximum effective stresses of various geometries of walls

		Effective Stress (psi)						
		Columns						
		1	2	3	4	5	7	10
Rows	2	565	676	639	652	660	651	649
	3	584	645	634	634	646	653	660
	4	589	671	666	671	671	674	674
	5	588	662	640	638	647	658	664
	7	583	614	635	636	646	657	664
	10	588	700	668	668	671	670	670
	12	588	713	669	659	661	664	659
	15	588	706	645	636	64	645	645

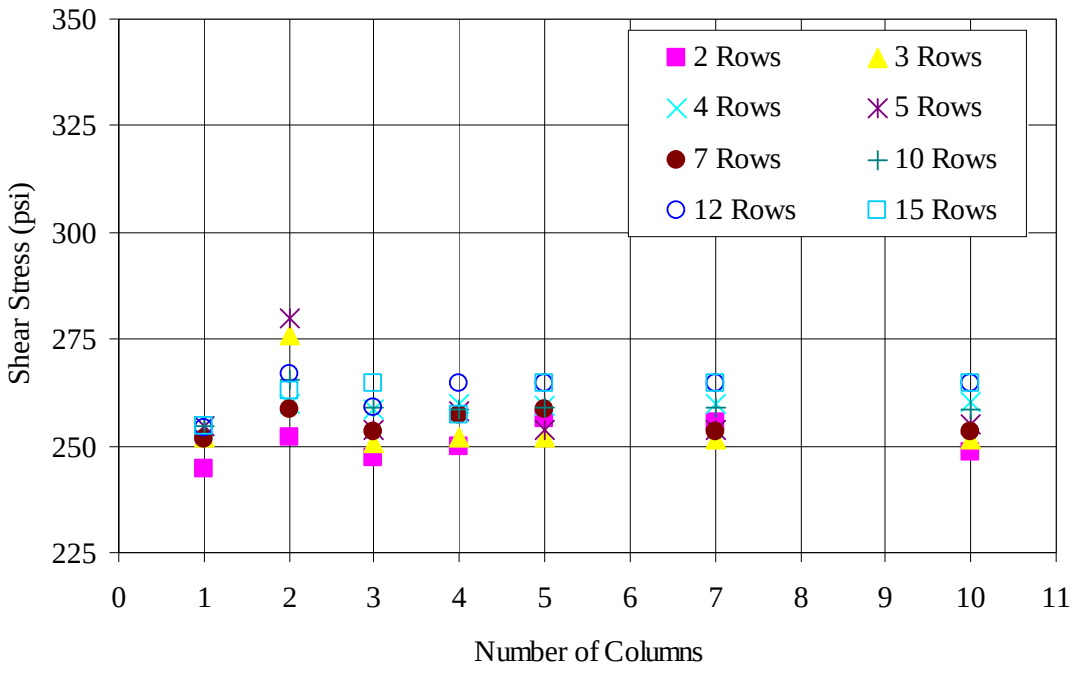

Figure 3.36. Plot of geometry vs. shear stress

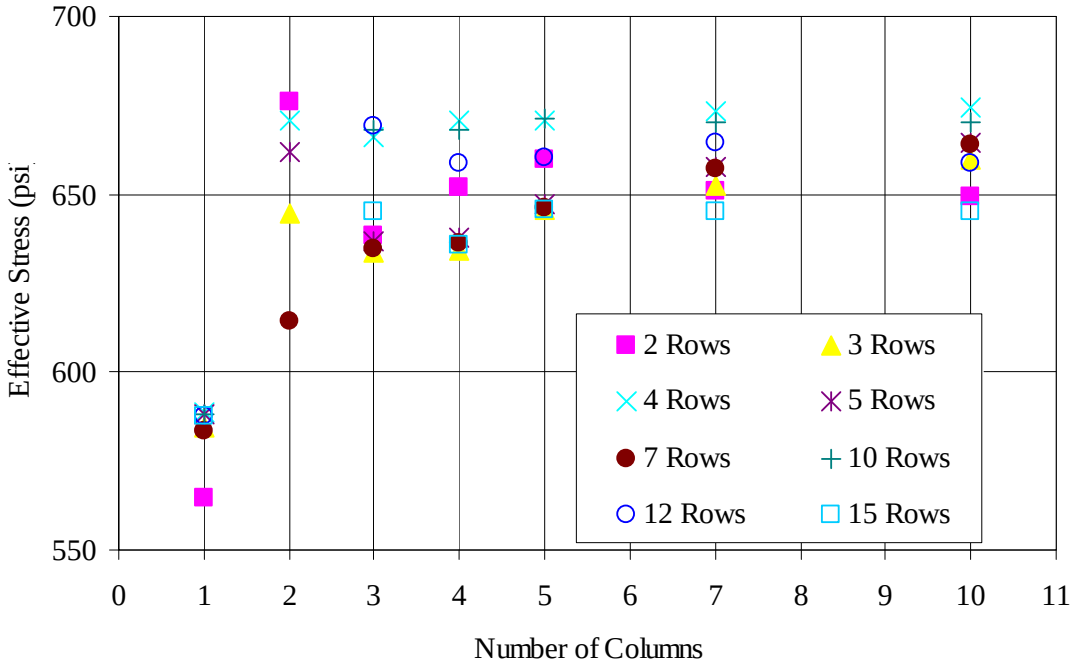

Figure 3.37. Plot of geometry vs. effective stress

The plot of the stresses versus number of blocks in a row demonstrates that there is no significant relationship between geometry and maximum breaching shear stress. These plots show that beyond a model of a single row or column, the geometry of the wall is independent of the stress experienced. The single column data is not a direct comparison because the wall section were modeled in stack bond pattern and the strength and stress have been reported to vary greatly from running bond pattern. The single row can be seen as extension of stack bond pattern since no blocks are above the bottom row.

Next, FEM were used to investigate the effects that material properties have on the shear stresses. In order to do this, one simple wall model was used; the model had 5 rows by 5 blocks in a row. The investigation examined the effects of ultimate compressive strength and unit weight.

Since most properties of cementitious products can be directly linked to ultimate compressive strength f'_m, this property was investigated first. The compressive strength was varied while keeping the load duration, the peak pressure, wall geometry, and all other properties constant. Since this property is connected with the modulus of elasticity, this quality will be changed as well. Table 3.9 shows the maximum values for the shear stress and effective stress obtained during the model-run. Figure 3.38 and Figure 3.39 show plots the data from Table 3.9.

Table 3.9. Stresses for compressive strength suitability study

Comp. Strength	Shear Stress (psi)	Effective Stress (psi)
1500	87	220
1750	97	221
2000	102	217
2250	99	226
2500	105	228
2750	103	225
3000	102	219
Average	99	222
Stand Dev	5.86	4.00

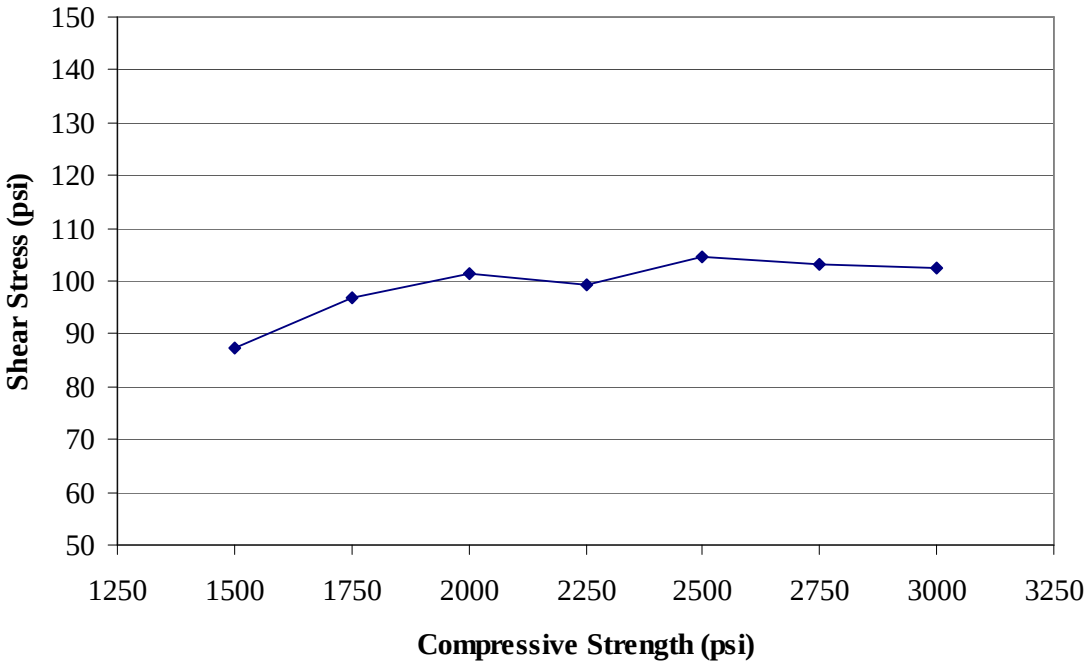

Figure 3.38. Plot of out-of-plane shear stress vs. compressive strength

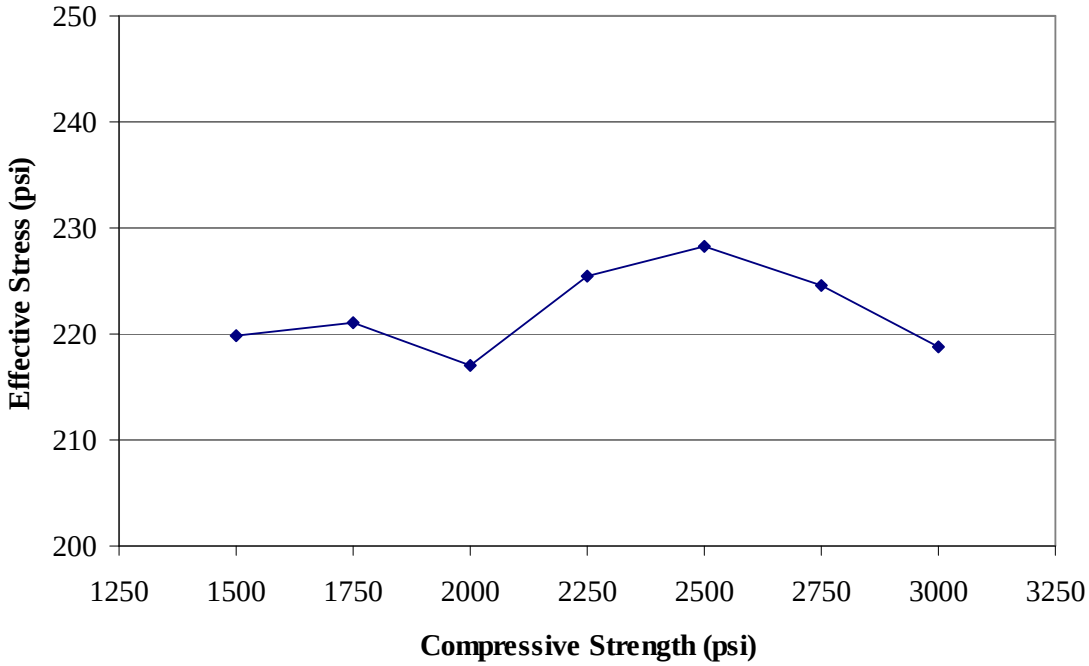

Figure 3.39. Plot of effective stress vs. compressive strength

Looking at the data in Table 3.9 and the following figures shows there is no direct connection between the ultimate compressive strength and the stresses experienced in the breaching shear response. If there is an effect caused by changing the ultimate strength of the masonry, this effect can be compensated by working the compressive strength into the resistance formulation.

The next property looked into was the unit weight of the CMU. The weight of the CMU makes up most of the mass of the wall. Since the loading is dynamic, a change in the overall mass or weight of the system should cause a change in the stress of the response. In order to do this, the same wall as used for the compressive strength suitability study was used and the unit weight is changed from lightweight concrete to middleweight concrete. Even though the modulus of elasticity is connected with the unit weight, the modulus of elasticity remained constant for these analyses. Table 3.10 shows the maximum values for the shear stress and effective stress of the suitability study over

the run-time of the model. Figure 3.40 and Figure 3.41 show plots of the data in Table 3.10.

Table 3.10. Stresses for compressive strength suitability study

Unit Weight (lb/ft^3)	Shear Stress (psi)	Effective Stress (psi)
85	103	221
90	100	222
95	102	222
100	99.1	221
105	100	220
110	100	220
115	101	219
120	103	218
125	102	217
130	104	217
135	104	216
140	102	216
145	100	216
150	100	216

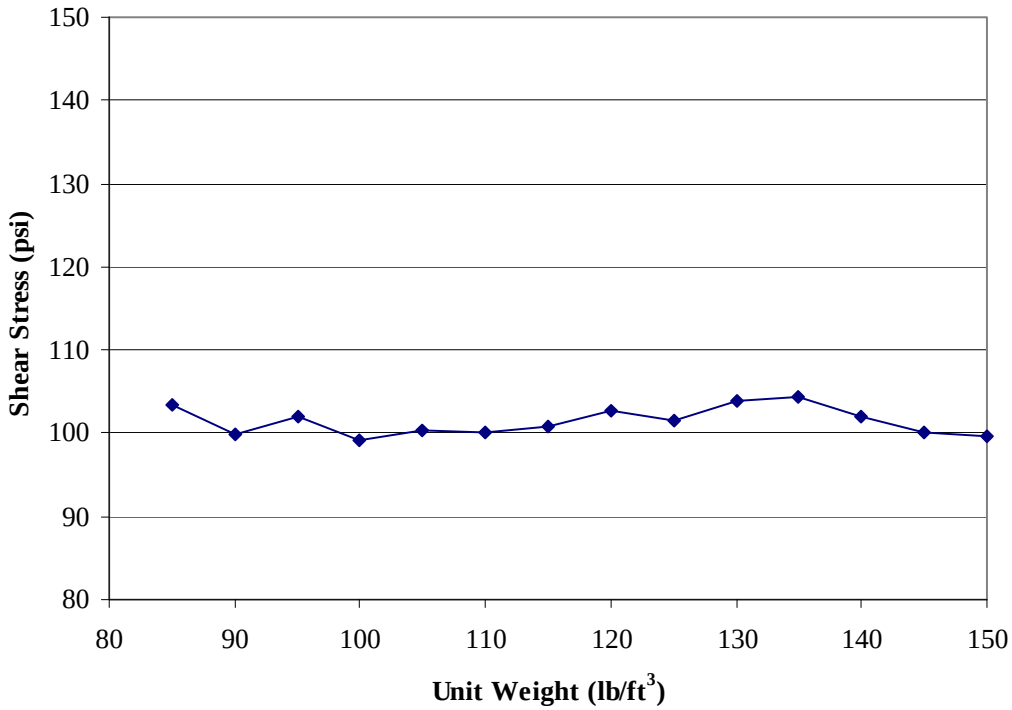

Figure 3.40. Plot of out-of-plane shear stress vs. unit weight

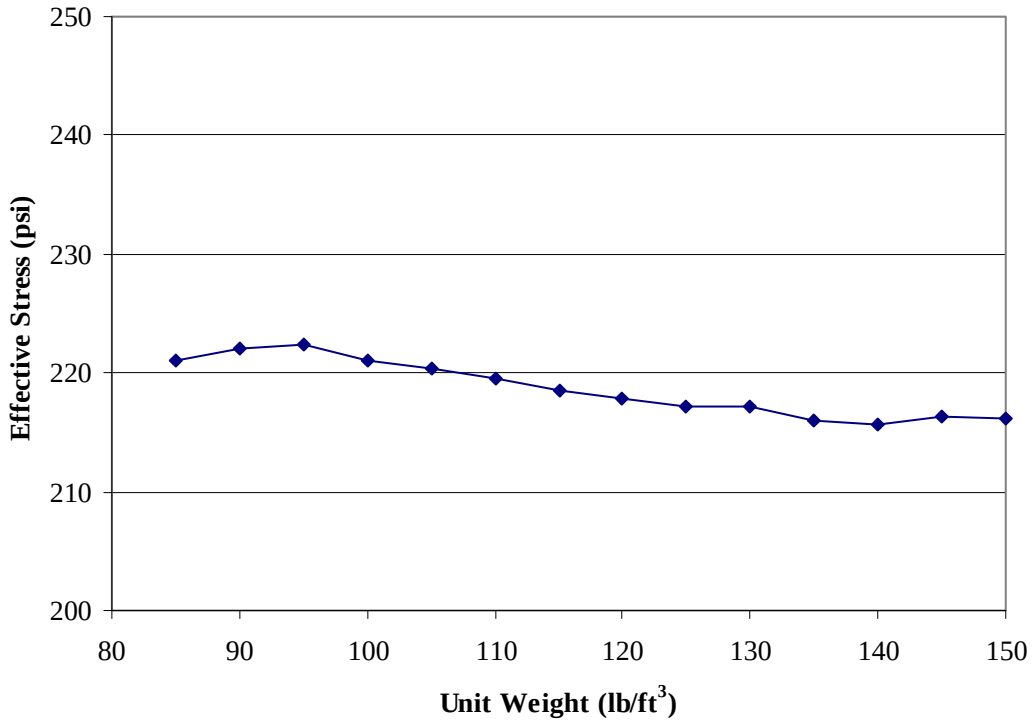

Figure 3.41. Plot of effective stress vs. unit weight

The effective stress plot demonstrates a downward trend of stress as the unit weight goes up. This is to be expected as an increase in unit weight gives an increase in mass of the system. However, the decrease is negligible over the range of unit weights. The other figures show that there is a uniform stress value for the same loading for all unit weights and that there is no direct relationship between breaching shear stress and unit weight.

Next, the effects of loading were investigated. The first investigation into loading was whether a change in impulse affected the magnitude of the shear stress. The loading shapes were the simplified triangular pulse load and rectangular load. The maximum loading pressure and loading duration were held constant, and only the shape was changed; therefore, the applied impulse for the rectangular loading was twice the impulse as the triangular loading. These loading shapes are seen in Figure 3.42. Various FEM's

from geometry testing were modified in order to analyze the loading shape's influence on the breaching phenomenon. Table 3.11 shows the out-of-plane shear stress and effective stress for the triangular pulse shape. Table 3.12 shows the average and the standard deviation.

Table 3.11 shows that there is a difference between the rectangular and triangular load in all stresses. The difference is as high 40.8 psi for the shear stress. However, for the most part, the difference in shear stress is less than 30 psi for 50 psi. This pattern is carried through effective stress. All data shows to have an average percent difference of less than 10% and a standard deviation of less than 10 psi. Therefore, this shows there is a slight difference in stress values with different loading shapes, but the difference is negligible. The data shows how the shear stress is not greatly affected by increasing the impulse, such as doubling the impulse.

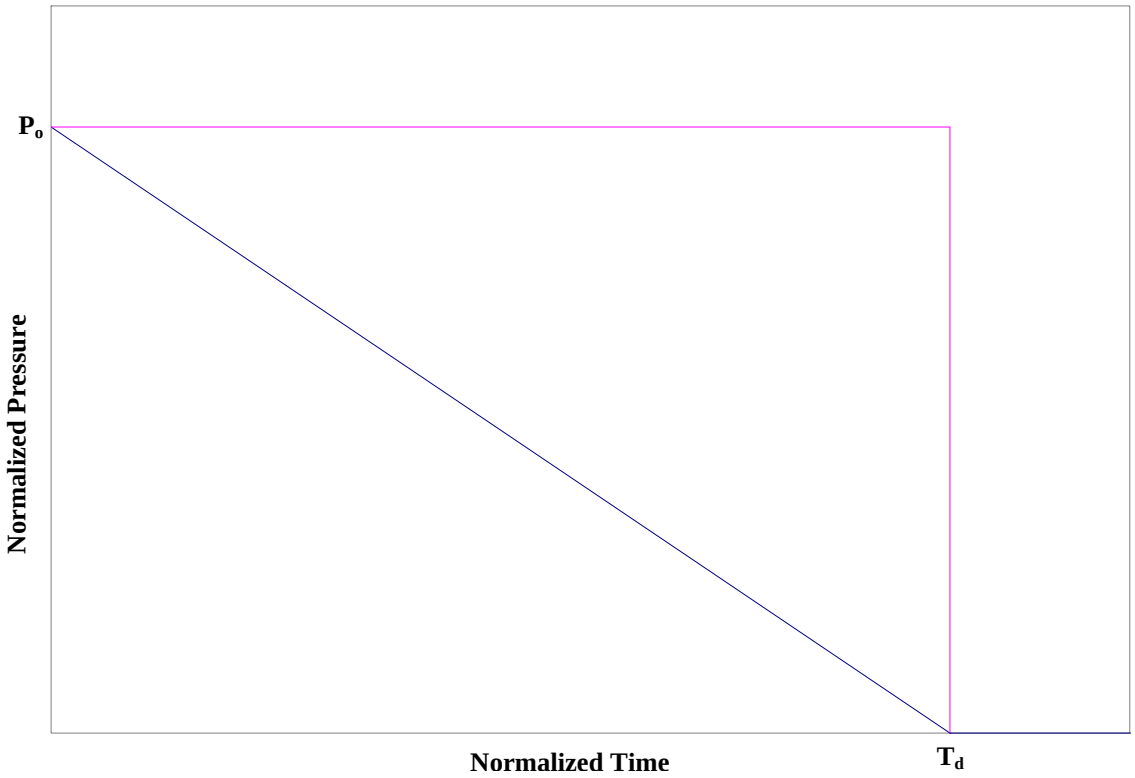

Figure 3.42. Plot of normalized loading

Table 3.11. Stresses from loading shape suitability study

Wall Geometry	Shear Stress (psi)		Effective Stress (psi)	
	Tri.	Rect.	Tri.	Rect.
3x3	267	290	646	695
3x5	284	307	668	715
3x7	267	290	647	694
3x10	252	290	660	694
5x3	265	288	646	693
5x5	282	306	671	718
5x7	265	306	646	718
5x10	282	306	671	719
10x3	265	288	657	713
10x5	265	288	659	717
10x7	265	288	665	715
10x10	265	288	659	716

Table 3.12. Statistical data on loading shape suitability study

Wall Geometry	Shear Stress (psi)		Effective Stress (psi)	
	Difference	% Diff.	Difference	% Diff.
3x3	23	8.5%	49	7.6%
3x5	22	7.8%	47	7.1%
3x7	23	8.6%	47	7.3%
3x10	38	15%	34	5.2%
5x3	23	8.7%	48	7.4%
5x5	23	8.3%	48	7.1%
5x7	41	15.4%	72	11%
5x10	24	8.4%	47	7.1%
10x3	23	8.8%	56	8.6%
10x5	23	8.7%	58	8.8%
10x7	23	8.7%	51	7.6%
10x10	23	8.7%	58	8.7%
Aver.	26	9.7%	51	7.8%

Also, the differences in peak pressure were examined to see if it caused any difference in magnitude of the shear stresses. Only three FEM's were used, and only the peak pressure in both triangular and rectangular loading shape was varied. Table 3.13, 3.14 and 3.15 show the data from the peak pressure suitability study for three different walls. Figure 3.43 and Figure 3.44 show plots of the data from Table 3.13, 3.14, and 3.15.

Table 3.13. Values of stresses for the 5x5 wall from the peak pressure suitability study

Peak Pressure (psi)	Triangular		Rectangular	
	Shear Stress (psi)	Effect. Stress (psi)	Shear Stress (psi)	Effect. Stress (psi)
5	54	133	61	152
10	102	217	112	244
15	122	321	135	344
20	140	359	151	384
25	149	374	162	411
30	163	421	178	458
35	190	485	208	520
40	223	546	243	589
45	254	616	273	658
50	282	671	306	718

Table 3.14. Values of stresses for the 10x3 wall from the peak pressure suitability study

Peak Pressure (psi)	Triangular		Rectangular	
	Shear Stress (psi)	Effect. Stress (psi)	Shear Stress (psi)	Effect. Stress (psi)
5	54.1	135.9	60.4	155
10	86.9	214	98.0	244
15	120	302.4	135	330
20	138	334.5	149	363
25	151	373.4	166	423
30	169	426.8	187	475
35	187	487.8	208	537
40	215	558.8	237	611
45	238	611.8	259	658
50	265	658.7	288	713

Table 3.15. Values of stresses for the 3x10 wall from the peak pressure suitability study

Peak Pressure (psi)	Triangular		Rectangular	
	Shear Stress (psi)	Effect. Stress (psi)	Shear Stress (psi)	Effect. Stress (psi)
5	54.2	134	54.2	134
10	94.7	209	94.7	209
15	122	320	122	320
20	137	370	137	370
25	159	388	159	388
30	196	407	196	407
35	201	477	201	477
40	218	536	218	536
45	240	599	240	599
50	252	660	290	694

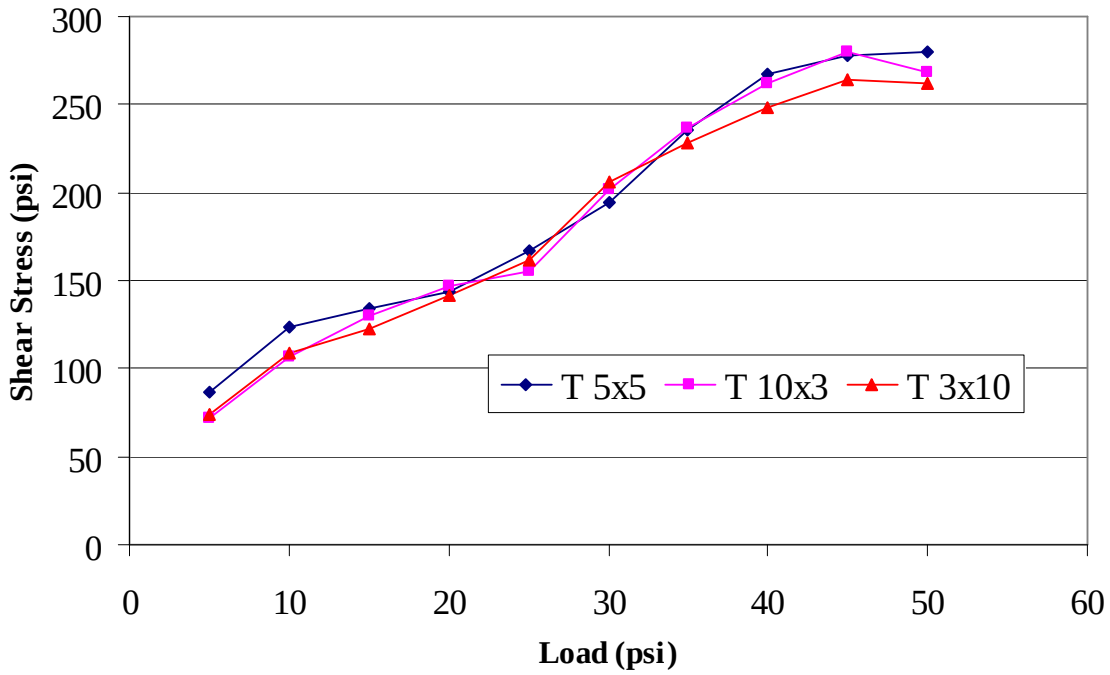

Figure 3.43. Plot o out-of-plane shear stress vs. peak pressure

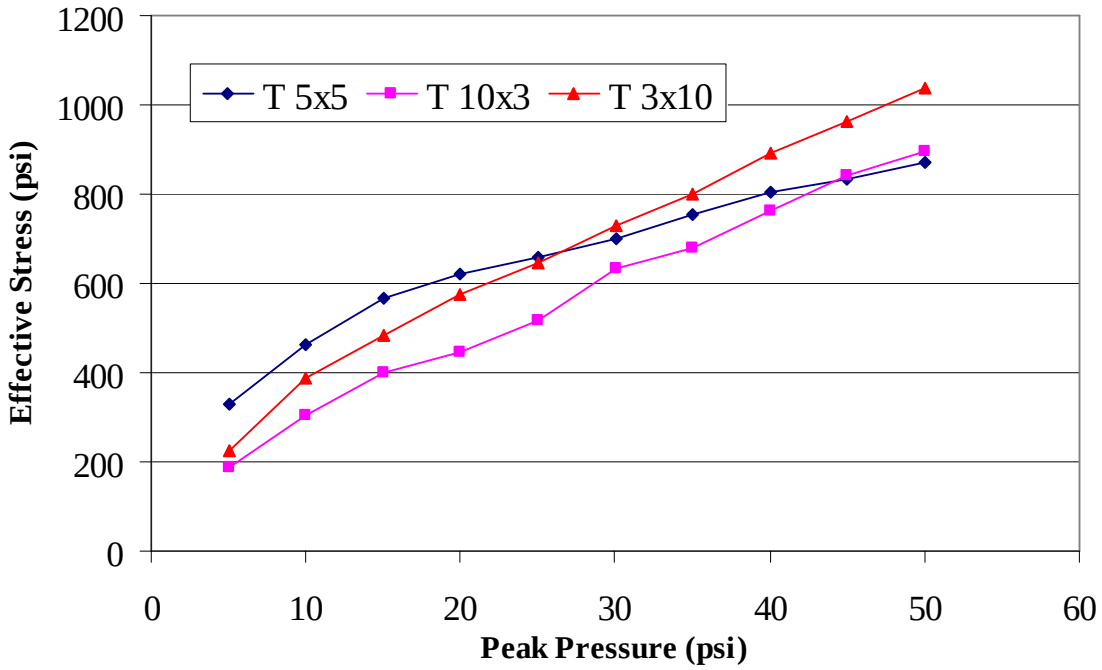

Figure 3.44. Plot of effective stress vs. peak pressure

The graphs and data show that there is a relationship between peak pressure and breaching stress values. The relationship is approximately linear. The R-squared values are all above 0.95 indicating a good fit for linear regression. Therefore, there is linear relationship between pressure and stress values; this is expected in shear stress since a simple structural analysis will result in the linear increase of shear forces with a given pressure or line load.

The final investigation looks at the effects of grouting. In order to do this, several wall models were created that include grout. All models using grout were partially grouted. Table 3.16 shows values for the maximum out-of-plane shear stresses for both grouted and non-grouted models occurring immediately after the blast wave hits the wall. Figure 3.45 and Figure 3.46 show graphical version of Table 3.16.

Table 3.16. Grouted vs. non-grouted maximum stresses

	Shear Stress (psi)			Effective Stress (psi)		
	Non-Grouted	Grouted	Difference	Non-Grouted	Grouted	Difference
5x3	265	266	0.9	646	780	135
5x5	282	280	2.2	671	870	199
5x7	265	289	24	646	833	187
5x10	282	294	12	671	839	168
7x3	254	280	27	635	799	164
7x5	259	284	25	646	717	71.2
7x7	253	289	36	657	717	59.5
7x10	253	282	29	664	726	62.1
10x3	265	268	3.8	657	897	240
10x5	265	277	13	659	827	168
10x7	265	281	17	665	751	86.6
10x10	265	277	13	659	783	124
12x3	259	266	7.0	669	847	177
12x5	265	276	11	661	823	162
12x7	265	276	12	664	788	124
12x10	265	277	12	659	774	115
15x3	265	267	2.2	645	702	56.8
15x5	265	293	28	636	720	84.5
15x7	265	277	12	645	714	68.2
15x10	265	299	34	645	726	80.5

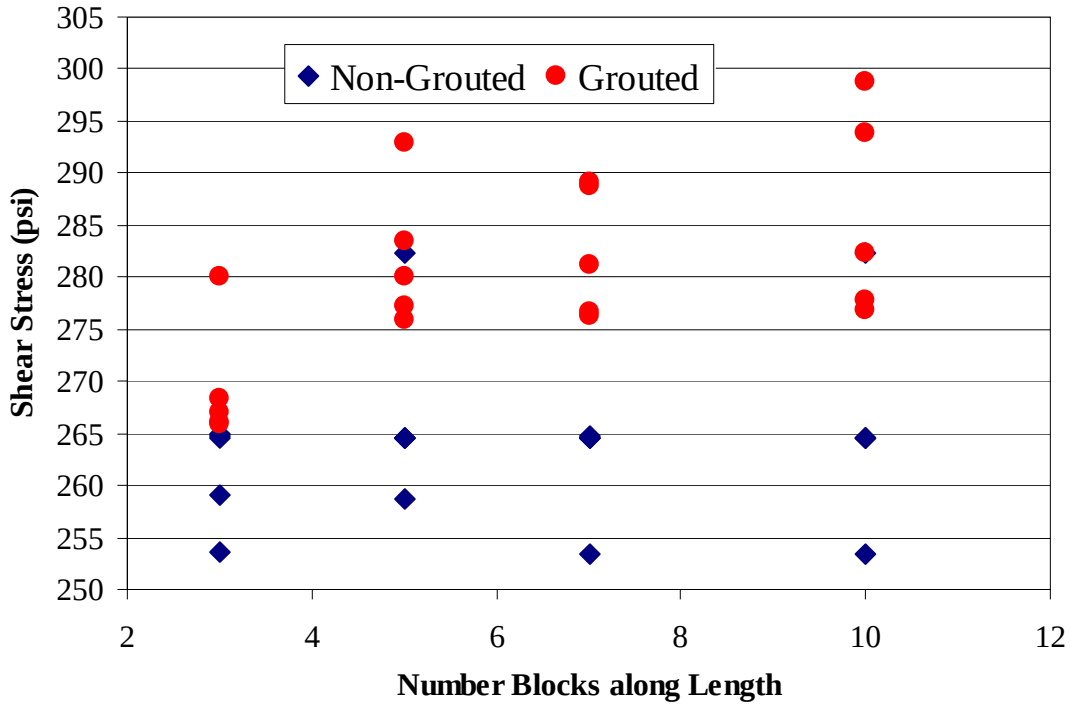

Figure 3.45. Out-of-plane shear stresses for grouted and non-grouted walls

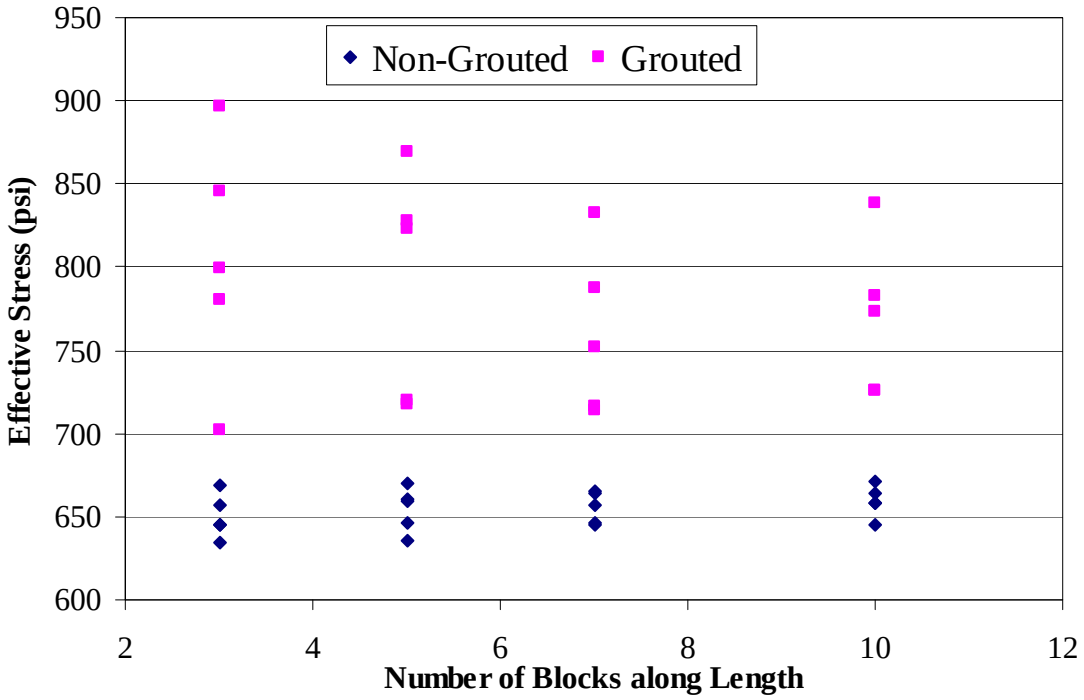

Figure 3.46. Effective stresses for grouted and non-grouted walls

As can be seen from the above graph, the grouted sections resulted in higher shear stresses; this was because the wall sections around the grouted columns are stiffer and would attract a higher percentage of the load. The models were only grouted in the end cells of the models, so an increase in the number of blocks would increase the distance between grouted cells. There is however no correspondence between the distances between grouted columns and the shear stress values. This indicates that shear stress experience, while not completely independent of the grouting, is independent of where the grout is placed for the breaching shear effect. The grout does cause additional stress in the wall sections, and this was compensated for in Chapter 4.

CHAPTER 4

DESIGN SHEAR RESISTANCE

4.1 Introduction

The point of this chapter is to highlight the steps taken to develop an engineering-level design equation for direct shear in CMU walls subjected to blast loading. This design equation must provide an adequate prediction of the strength of the system without being overly conservative.

Since this system is dynamic, an overview of structural dynamics is given with a focus on approximate modeling towards understanding the breaching phenomenon of CMU walls. The wall dynamics properties of the wall are determined, allowing a single block or a group of blocks to be modeled as quasi-static. This allows the wall to be analyzed in a static state and be conceptualized as a beam. Finally, the structural analysis will allow for the development of a nominal shear force according to the maximum pressure and to eventually develop a shear resistance equation.

4.2 Structural Dynamics

In order to better understand the breaching phenomenon, a structural dynamic analysis of the wall was to be carried out. Most systems are too complicated to have a full structural dynamics analysis performed; this is because the system is made of an infinite number of parts that want to move in an infinite number of ways. This multiple

degree-of-freedom system is out of the scope of most practicing design engineers; therefore, a complicated system needs to be turned to a simplified one-way system. The following section gives an overview of single degree-of-freedom (SDOF) systems plus added simplifications that can be taken for special cases. A full SDOF analysis was not carried out, but parts of the analysis were used to determine dynamics properties of the wall.

4.2.1 Single Degree-of-Freedom Model

A SDOF system is system where there is only one way for the system to move hence a single degree-of-freedom. This is extended to a multiple degree-of-freedom system where predominant motion can be described by a single motion and all other motions can be described by this motion. This degree-of-freedom can be a displacement or a rotation. Figure 4.1 shows free body diagram of a lumped-mass, SDOF system.

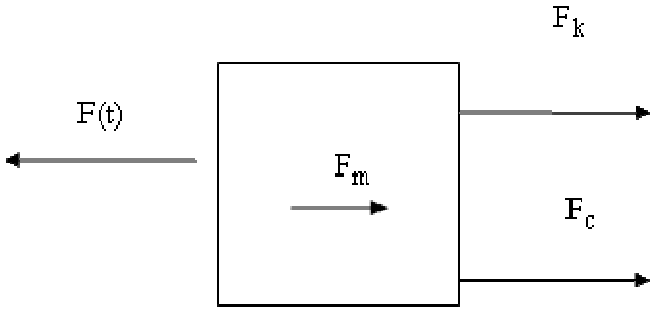

Figure 4.1. Single degree-of-freedom model

With the help of Bigg's *Introduction to Structural Dynamics*, the system has four forces acting on it. These forces are inertia-induced force, stiffness-induced force, damping-induced force, and the applied force. Putting the above system in equilibrium produces

$$F_m + F_k + F_c = F(t) \tag{4-1}$$

where F_m = mass-induced force, F_k = stiffness-induced force, F_c = damping-induced force, and $F(t)$ = forcing function or applied force according to time.

Using Newton's law of motion, mass-induced force is equal to mass times the acceleration given by

$$F_m = ma = m\ddot{y} \tag{4-2}$$

where m = mass of the system and $a = \ddot{y}$ = acceleration of the system. By definition, the acceleration is defined as the second derivative of the displacement according to time.

The resistance-induced force is provided by a resistance or rigidity of the system. This resistance can be conceptualized as a simple elastic spring; an elastic spring has a constant stiffness per unit displacement. This then gives the resistance-induced force as

$$F_k = k\delta = ky \tag{4-3}$$

where k = resistance or stiffness of the system per unit displacement and $\delta = y$ = displacement of the system.

The damping-induced force is provided by friction, cracking, or other energy-absorption mechanism. All these damping effects can be approximated by a viscous damper; this type of damper requires a constant force to move a body through a viscous liquid at a certain speed. The damping-induced force is given by

$$F_c = cv = c\dot{y} \tag{4-4}$$

where c = damping coefficient of the system and $v = \dot{y}$ = velocity of the system. The velocity is defined as the first derivative of the displacement according to time.

Substituting Equation 4-2, 4-3, and 4-4 into Equation 4-1 gives

$$m\ddot{y} + c\dot{y} + ky = F(t) \tag{4-5}$$

which is the governing equation for a SDOF system. This equation can be solved to find the exact solution for a lumped-mass system. With the full dynamic equation known, other properties of the dynamic system can be obtained. The natural frequency of the system ω_n is given by

$$\omega_n = \sqrt{\frac{k}{m}} \tag{4-6}$$

The natural period of the system T_n is given by

$$T_n = \frac{2\pi}{\omega_n} \tag{4-7}$$

The natural period is the amount of time that the system takes to complete a full cycle.

Unlike in the above lumped-mass system, the mass for most structures is distributed over the entire volume. Equation 4-5 can still be used, but the analysis becomes extremely difficult for systems, especially structures with continuous–mass distribution. An approximate method then must be carried out to ease computation. The approximate system is given by

$$m_e \ddot{y} + k_e y = F_e(t) \tag{4-8}$$

where m_e, k_e, and $F_e(t)$ = effective mass, effective resistance, and effective forcing function of the system, respectively. The damping forces are negligible in the blast simulations since the time of interest is small, so this force is assumed to be zero. Equation 4-6 can be expressed in terms of the real system by

$$K_m m\ddot{y} + K_L k y = K_L F(t) \tag{4-9}$$

where K_m and K_L = mass and load factors, respectively. The damping-induced force is assumed to be zero in the equivalent system. Since most of the system's response occurs

in the first mode, the approximation idealizes that all response will occur in a mode close to the first mode. The idealized system assumes the displacement of the system Φ(x) to be the same as that produced in static loading with the exception that the maximum deflection of the system is set to one. This is done to give a better approximation of the effective forces.

The equivalent mass, m_e, resistance, k_e, and force, F_e, of a distributed mass system is given by

$$m_e = \int_L m\Phi(x)^2 \mathrm{d}x \tag{4-10}$$

$$F_e = \int F(t)\Phi(x) \tag{4-11}$$

$$k_e = F_e \tag{4-12}$$

The mass factor K_m and load factors K_L are given by

$$K_m = \frac{m_e}{m} = \frac{\int_L m\Phi(x)^2 \mathrm{d}x}{m} \tag{4-13}$$

$$K_L = \frac{F_e}{F} = \frac{\int_L F\Phi(x) \mathrm{d}x}{F} \tag{4-14}$$

Finally, if Equation 4-6 is divided through by K_L, the equation is given by

$$K_{Lm} m\ddot{y} + ky = F(t) \tag{4-15}$$

where K_{Lm} = the load mass factor (ratio of K_m to K_L). The previous equation will give the idealized SDOF response of a system; this system gives accurate displacement, and this displacement can be related to the internal forces of the system. The natural frequency of the equivalent system is given by

$$\omega_{ne} = \sqrt{\frac{k_e}{m_e}} = \sqrt{\frac{k}{K_{Lm} m}} \tag{4-16}$$

More detail can be found Bigg's *Introduction to Structural Dynamics* or other structural dynamics books.

4.2.2 Pressure-Impulse Simplifications

A SDOF system can be a convenient simplification; another approach is to set up pressure-impulse (P-I) diagrams to define whether the member may be damaged or not. A normal response spectrum highlights the importance of some property of the structure as compared to the response; this property can be duration of loading, natural period, natural frequency, or other like properties. On the other hand, P-I diagrams uses the load and impulse for a given response. Figure 4.2a shows the response of an undamped, perfectly elastic SDOF system. Figure 4.2b shows an equivalent system in a P-I diagram format where P_o is the peak pressure, K is the stiffness, M is the mass, x_{max} is the maximum displacement, I is the impulse, t_d is the loading duration, and T is the natural frequency. Seen in both graphs, there exist three loading regimes: impulsive, dynamic, and quasi-static. P-I diagrams clearly show all three loading regimes and transfer points between the three regimes. The vertical asymptote is the impulsive regime, the horizontal asymptote is the quasi-static regime, and the line that connects these two is the dynamic regime. These are shown on the response spectrum, but the transfer points are not clearly determined because the curve does not have asymptotic properties in the impulsive regime.

Seen from the response spectrum diagram, the period is important. The period is the amount of time it takes for system to complete a full-cycle of vibration. Very high periods are characterized by large, flexible structures; while, very low periods can be deemed to be inflexible or rigid.

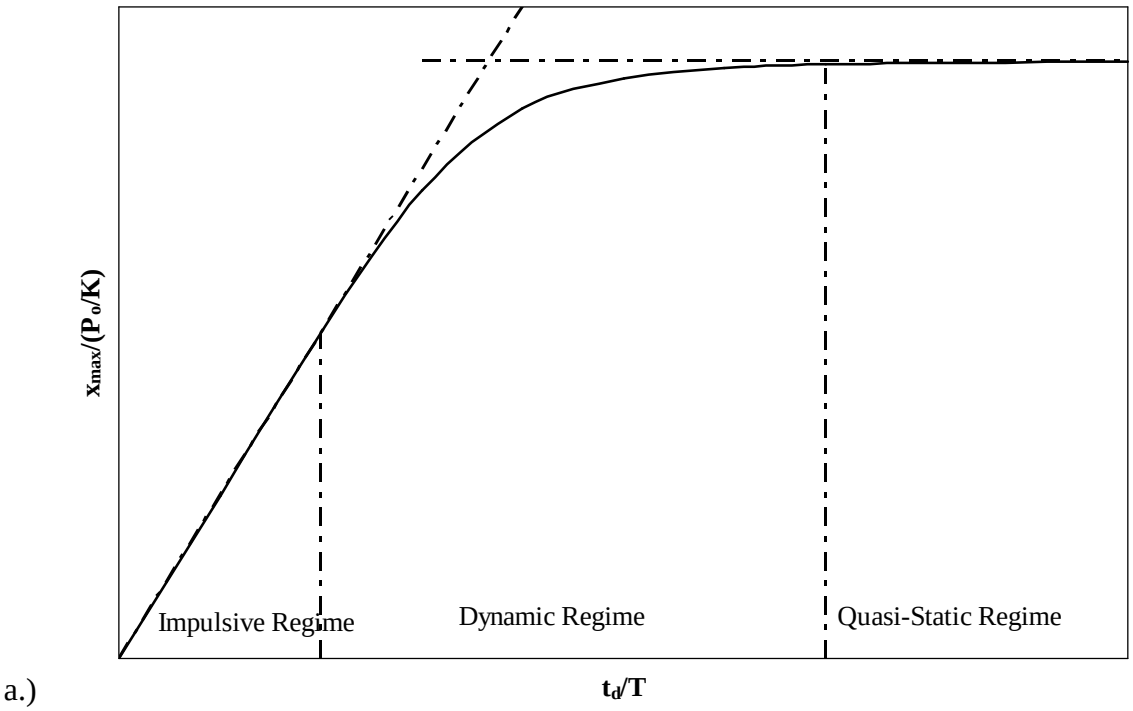

a.)

b.)

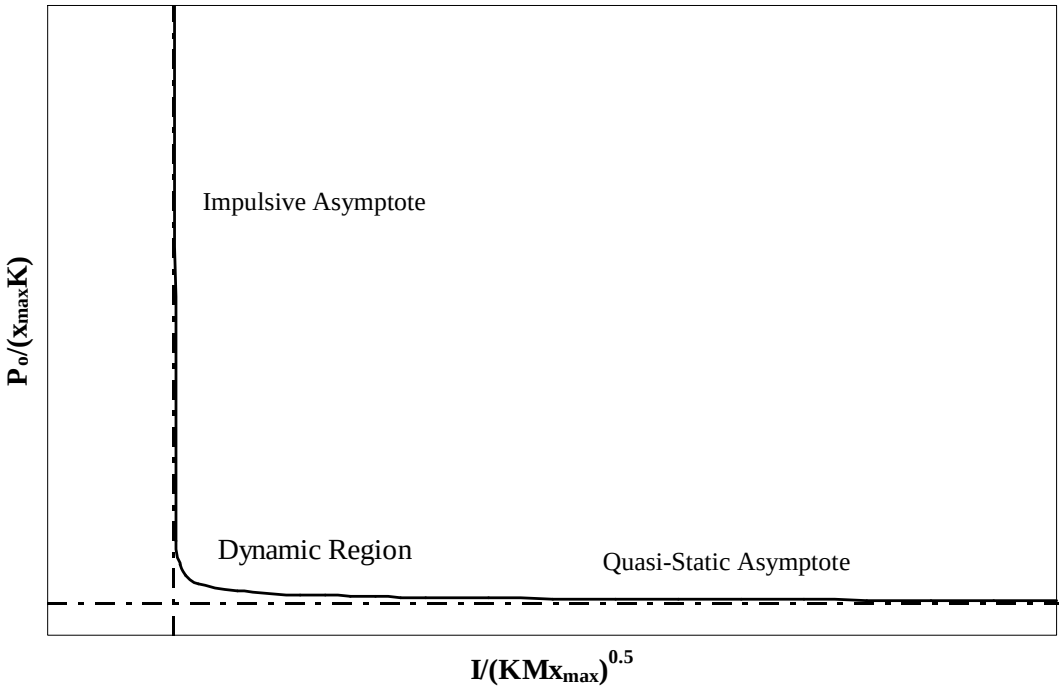

Figure 4.2. a) Typical response spectrum and b) P-I diagram

Some system can be even further simplified. Figure 4.3 displays the quasi-static and impulsive regimes emphasizing the duration of loading, t_d, and time of response, t_m.

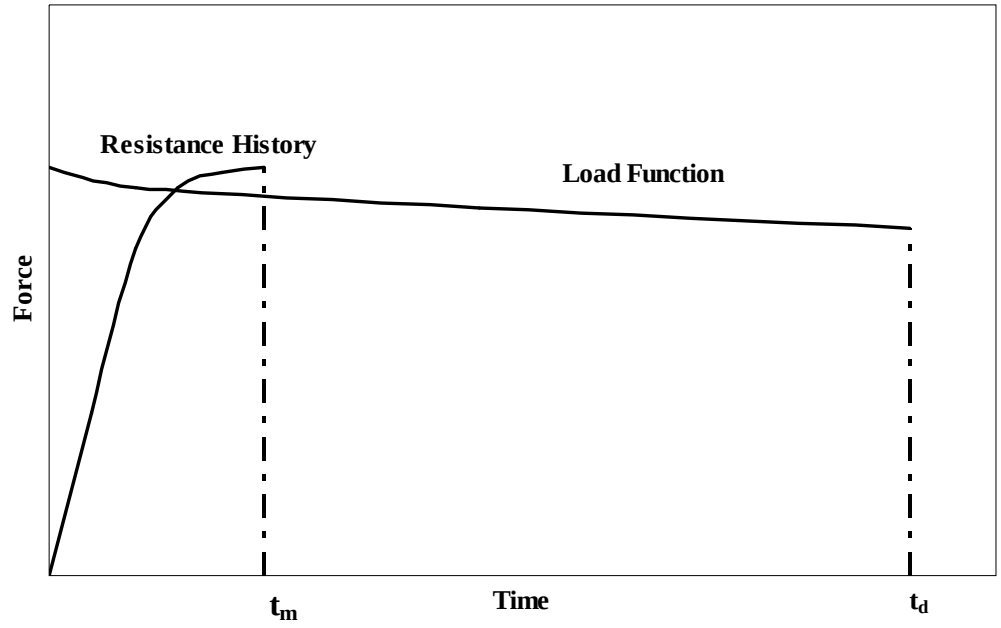

a.)

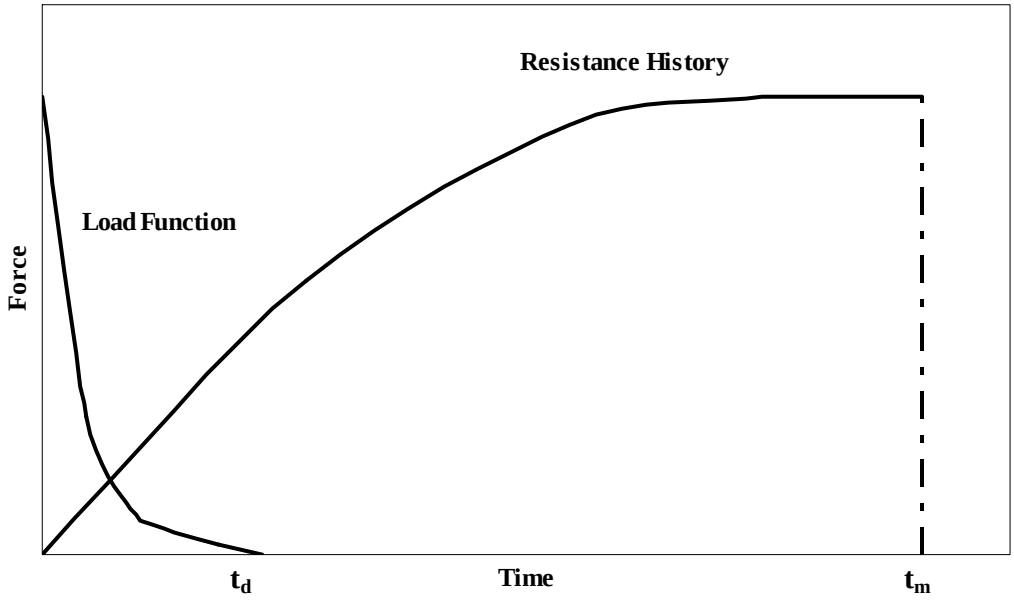

b.)

Figure 4.3. Loading regimes: a) quasi-static case and b) impulse case

The regime shown in Figure 4.3.a is a quasi-static loading case. Quasi-static regime is characterized by the period T being much shorter than the duration of loading t_d. In quasi-static loading regime, the peak resistance is reached before the loading value has had time to dissipate. Therefore, the resistance of a quasi-static system depends on the peak pressure and not on the loading duration.

The regime shown in Figure 4.3.b is an impulsive loading case. This case is characterized by the period of the system being much longer than the duration of loading. In the impulsive loading regime, the load is applied and dissipated before any significant system response has occurred. Therefore, the loading duration has almost very little impact on the system.

A third regime is the dynamic loading regime. The dynamic loading regime is characterized by the loading duration being of the same order as the period of the system. In this regime, the loading duration cannot be uncoupled from the maximum response of the system, and the response is more complex to determine.

4.3 Modeling of Breaching Response

In analyzing the finite element models, there are two structural models that could simulate the breaching response. The first is single-block beam analogy; the other is a beam that runs between grout cells. Both models were investigated to determine the best modeling approach to develop the resistance equation.

4.3.1 Dynamics of the Face Shell Beam Model

The finite element analysis showed that there are high shear stresses near the webs of each block for 2 to 3 ms after the pressure reaches the wall. High stresses existed near the webs even when there was grout present in the model. This indicated that each individual block carries only the shear developed on its face with the mortar not allowing transfer of shear. In addition, the geometry of the wall had no significant influence on the maximum value of shear stress in the non-grouted geometry investigation. Since breaching will not occur at the webs, the beam analogy was modeled with only one cell of the block with the face shell connections to the webs acting as perfectly fixed. Figure 4.4 shows a single cell of a block represented as a beam and a cross section of the representative beam; Figure 4.5 shows a visualization of the beam as fixed-fixed beam. From this model, the natural period can be obtained.

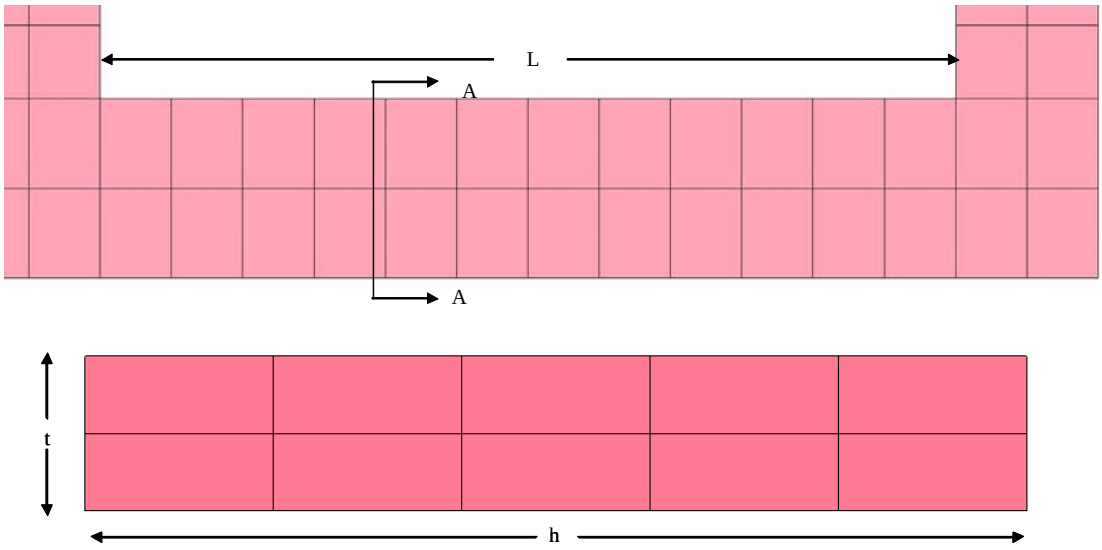

Figure 4.4. Face shell beam and cross section A-A

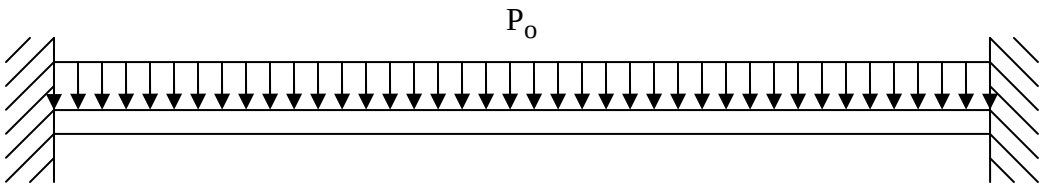

Figure 4.5. Single block beam representation

The beam has a span length L of one cell, a width h of the full height of the wall, and a thickness t of one face shell. The representative beam has a moment of inertia of

$$I = \frac{ht^3}{12} \tag{4-17}$$

The mass and the stiffness of the beam are

$$M = \frac{\gamma}{g} Lht \tag{4-18}$$

$$k = \frac{384EI}{L^3} \tag{4-19}$$

where γ is the unit weight of the block and g is the acceleration due to gravity. For a fixed-fixed beam under a uniformly distributed load, the assumed displacement equation is

$$\Phi(x) = \frac{16}{L^4}(L^2x^2 - 2Lx^3 + x^4) \tag{4-20}$$

With this equation, the equivalent mass factor, equivalent load factor, and equivalent load-mass factor are

$$K_M = 0.4064$$

$$K_L = 0.5333$$

$$K_{LM} = 0.7619$$

This gives the equivalent single degree-of-freedom response equation as

$$0.7619M\ddot{y} + \frac{384EI}{L^3}y = F(t) \tag{4-21}$$

Finally, the natural frequency is given by

$$\omega_n = \sqrt{\frac{k}{K_{LM}M}} = \sqrt{\frac{\frac{384EI}{L^3}}{0.7619M}} = \sqrt{\frac{384\mathrm{E}ht^3\mathrm{g}}{12L^3 \times 0.7619 \times \gamma Lht}} = \sqrt{\frac{16,230Et^2}{\gamma L^4}} \tag{4-22}$$

Table 4.1 shows representative numbers of an 8-in CMU. E is Young's modulus, and f'_m is the ultimate compressive strength of the masonry assemblage.

Table 4.1. Representative numbers for 8-in. CMU

f'_m	1500 psi
E	1400 ksi
t	1.25 in
γ	125 lb/ft^3
L	6.06 in

Substituting the values from Table 4.1, the natural frequency and natural period are

$$\omega_n = 19000/\mathrm{s} = 19\mathrm{kHz}$$

$$T_n = 3.4\times10^{-4}\mathrm{s} = 0.34\mathrm{ms}$$

Table 4.2 gives the following ranges for loading regimes from *Blast Effects on Buildings* (Smith and Cormie, 2009) and from *Modern Protective Structures* (Krauthammer, 2008).

Table 4.2. Loading regime ranges

Regime	Cormie	Krauthammer
Impulsive	$t_d/T_n < 0.1$	$t_d/T_n < 0.0637$
Dynamic	$0.1 < t_d/T_n < 10$	$0.637 < t_d/T_n < 6.37$
Quasi-Static	$t_d/T_n > 10$	$t_d/T_n > 6.37$

The loading duration t_d is assumed to be 0.01 s or 10 ms at its shortest duration. (The shortest duration of the dynamic testing was approximately 14 ms.) The natural period

gives loading duration to natural period ratio of approximately 30, which corresponds to the quasi-static regimes from both books. The quasi-static loading can be assumed for loading duration of 3.4 ms or more. Therefore, the breaching of the walls can be assumed to behave as if quasi-static loading is applied and can be modeled by applying a static pressure over the whole wall. This matches well with the FEM results found in the suitability study presented in Chapter 3, as the shape of the loading did not influence the shear stress but the peak pressure did.

4.3.2 Dynamics of Between Grout Cells Beam

The finite element analysis showed that there were high stresses at the interface between grouted and non-grouted cells in the models with grout present; this showed that there could be a beam analog that runs between grout cells with the columns idealized as perfectly fixed supports. Figure 4.6 shows the representative beam and cross section of the between grout cell beam (BGC beam). The same approach as used for the single block beam was used with the exception that the beam had a length L of the distance between grout cells, a thickness t of one face shell, width w of the block, and a height h of the height of one block. This model used only the face shells because the breaching will occur in the faceshell, not at the web. In addition, the webs have sufficient stiffness to ensure that the face shells have composite action.

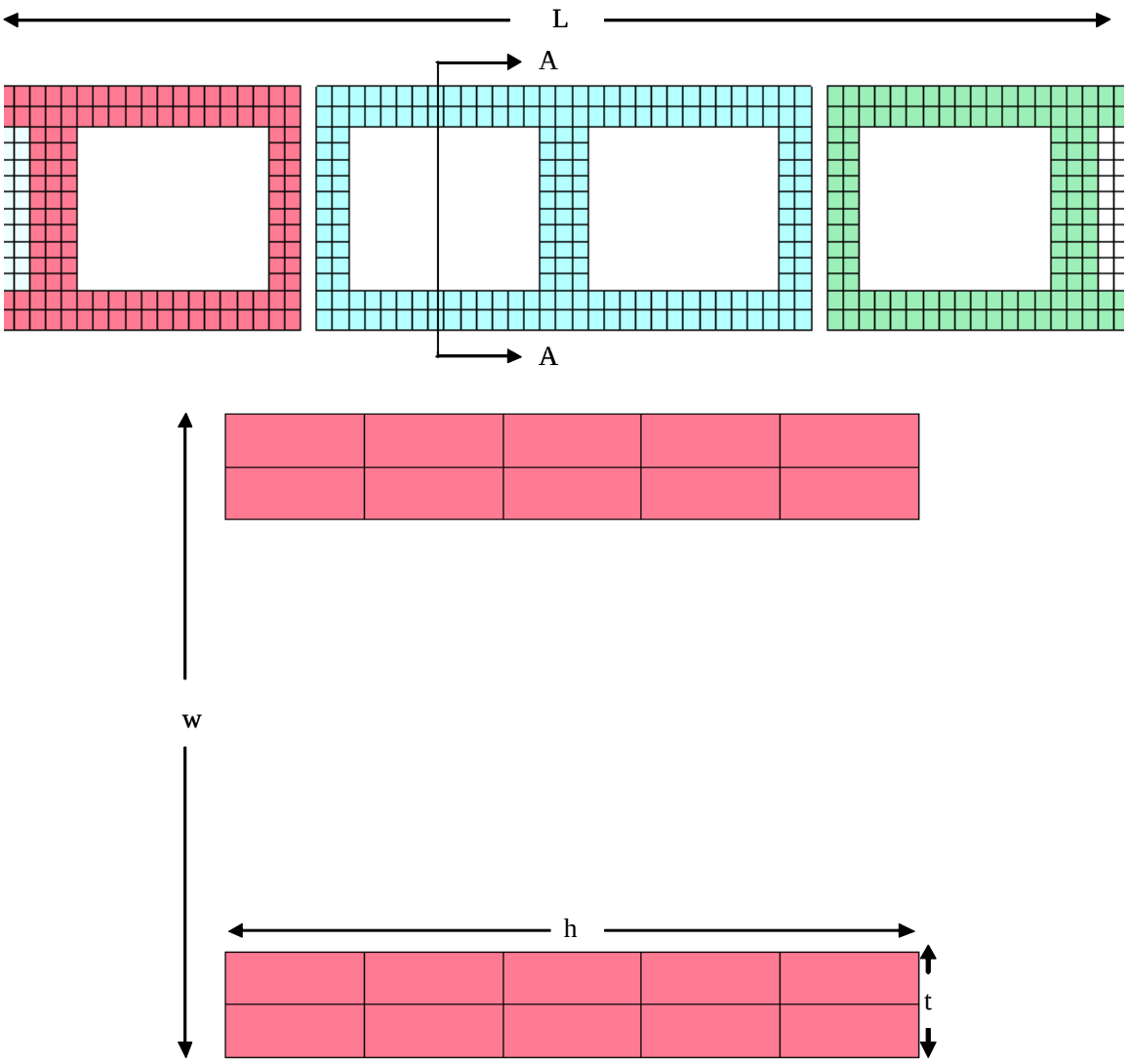

Figure 4.6. BGC beam and cross section A-A

The moment of inertia contributing to stiffness of the section was only the two face shells of the sections assuming composite action; it is represented by

$$I = 2(1/12ht^3 + th(w/2 - t/2)^2) \tag{4-23}$$

All other properties are the same for BGC breaching; the effects of reinforcing in the grout cells were assumed to be negligible because the shearing happens between columns. Then, the natural frequency is

$$\omega_{\mathrm{n}} = \sqrt{\frac{\frac{384EI}{L^3}}{0.7619M}} = \sqrt{\frac{389,500E(1/12t^2 + w^2/4)}{\gamma L^4}} \tag{4-24}$$

These values are given for CMU ranging from 6-in. to 16-in. in Table 4.3 with corresponding natural frequencies, and natural periods; in addition, the table shows the minimum loading duration in which quasi-static analysis can be used. The length is based on maximum bar spacing of 6 times the block's width subtracting the grouted parts of the length.

Table 4.3. Quasi-static details for between grouted cells beam

Size of CMU	w (in)	L (in)	ω_n (10^3/s)	T_n (ms)	$T_{d,min}$ (ms)
6-in	5.625	27.69	11.5	0.547	5.47
8-in	7.625	39.69	83.2	0.832	8.32
10-in	9.625	51.69	5.62	1.12	11.2
12-in	11.625	63.69	4.47	1.41	14.1
14-in	13.625	75.69	3.71	1.70	17.0
16-in	15.625	87.69	3.17	1.99	19.9

In the table above, the minimum loading duration for which the quasi-static response can be used. Since the blasts considered in this study are at least 15 ms long, 6-in to 12-in CMU can be analyzed using quasi-static for almost all cases. When wider blocks are being used, the loading duration must be found and checked against values determined for natural period. Figure 4.7 through Figure 4.11 show the effect that different parameters can have on the minimum load duration. The data was generated using inputs for an 8-in CMU block with a unit weight of 125 lb/ft^3 only varying the parameter of interest. Theses graphs cannot be used to determine the minimum load duration; they are only used to show the general effects the parameters have on the minimum load duration.

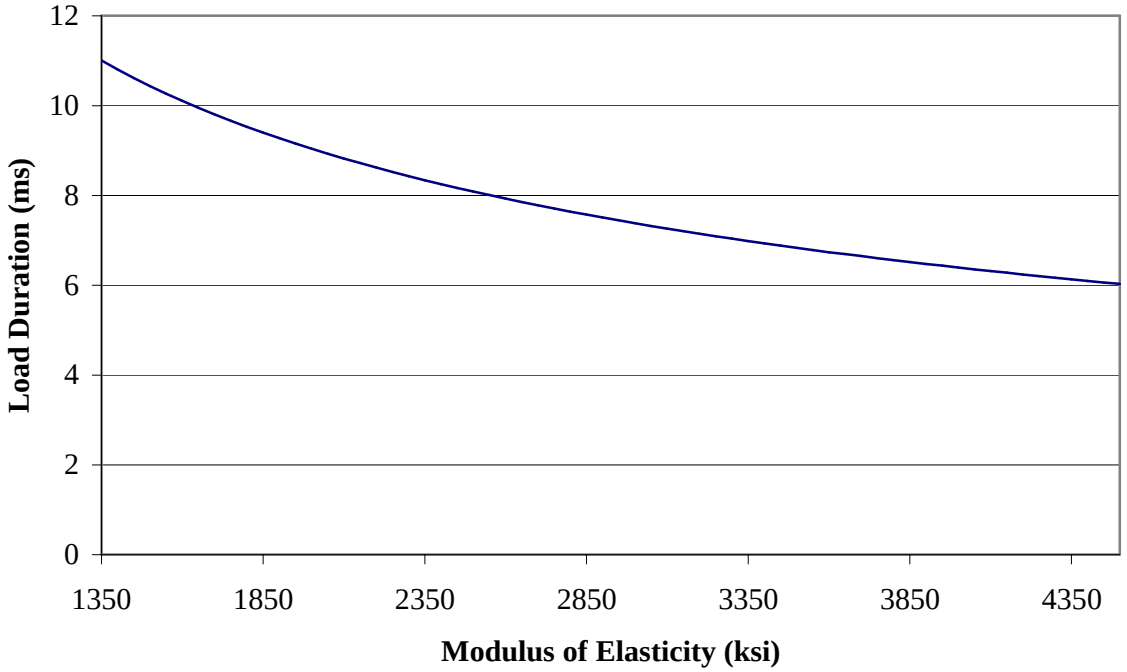

Figure 4.7. Minimum load duration vs. modulus of elasticity

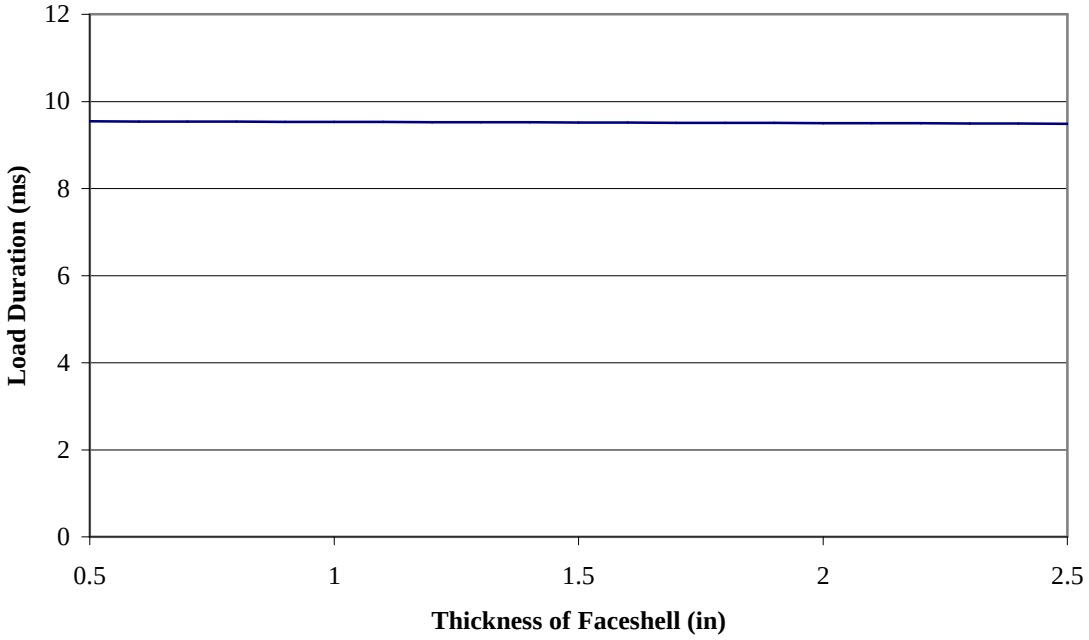

Figure 4.8. Minimum load duration vs. thickness of face shell

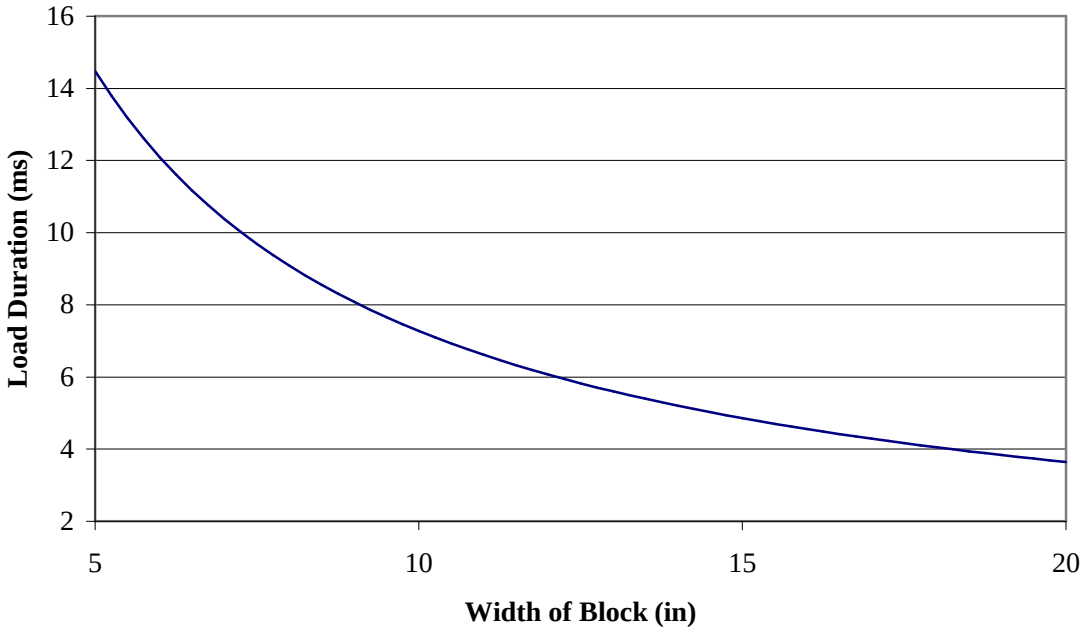

Figure 4.9. Minimum load duration vs. width of block

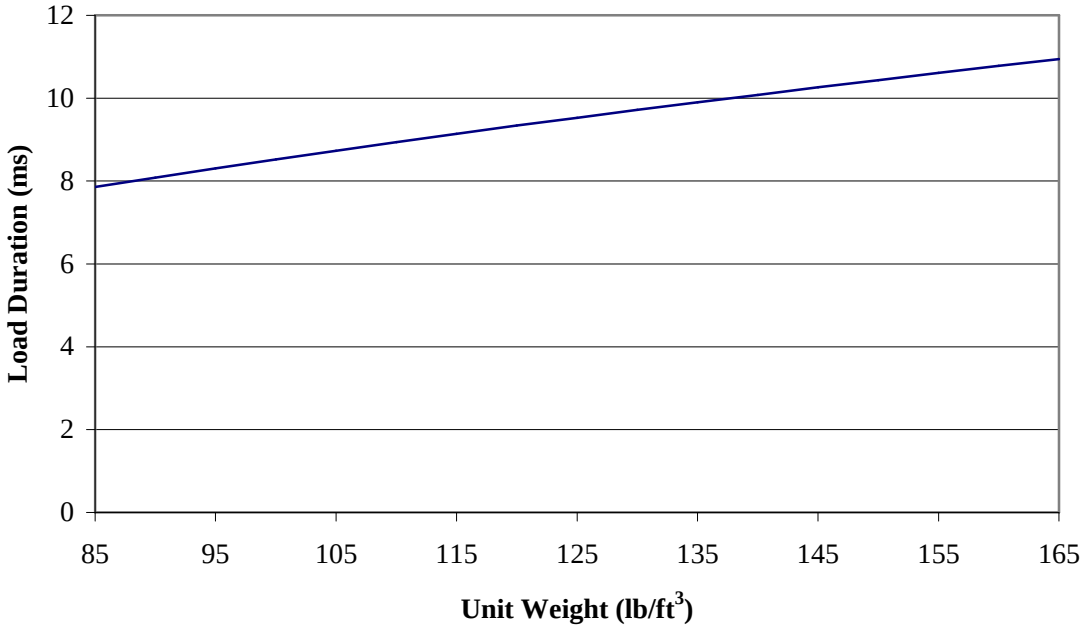

Figure 4.10. Minimum load duration vs. unit weight

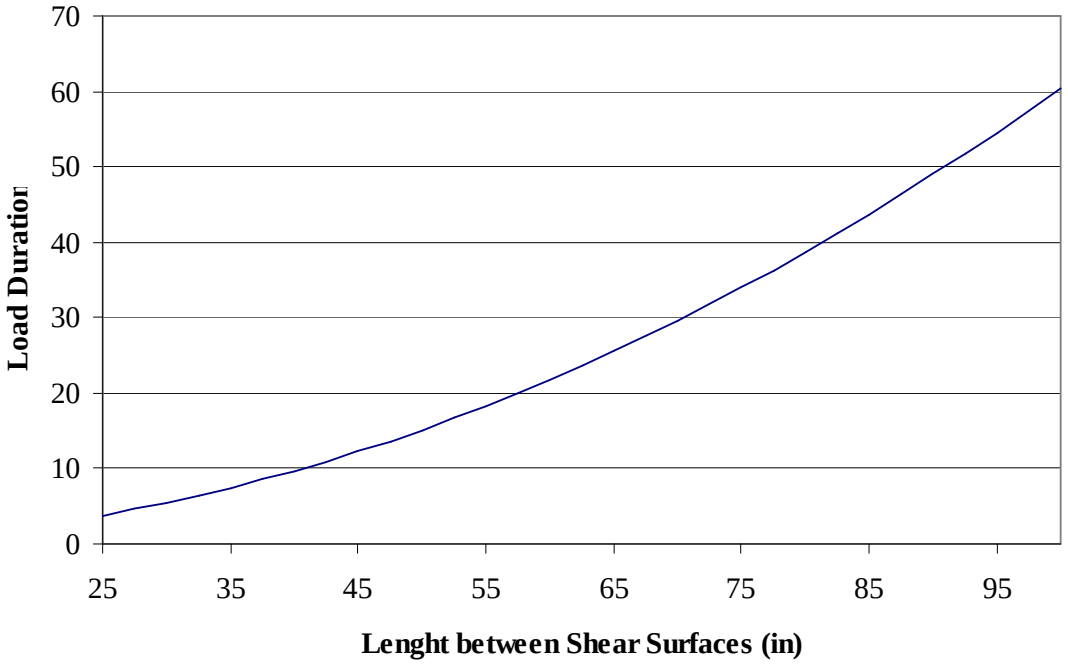

Figure 4.11. Minimum load duration vs. length between grout cells

The charts above show that the minimum load duration will change less than 5 ms for the variable ranges considered. This is especially true for the thickness of the face shells, *t*, which caused less than a 1 ms difference over its range of values. For modulus of elasticity, *E*, and the unit weight, γ, the variation was small as well. The width did change more rapidly with a variation of 10 ms over the data; however, the width of block would change along with the distance between grouted columns giving a lower variation. This leaves only the distance between shear planes as a major variable; the graph shows that the minimum duration load changes rapidly with length. Therefore, if a load duration is too small to assume quasi-static response for a given wall geometry, the length between grouted columns could be reduced until the quasi-static analysis can be used.

4.3.3 Direct Shear Modeling

Since both beam approximations are quasi-static, the complex wall is simply modeled as a one-way beam with fixed supports at both ends. Because of similarities between the models, the beams can be modeled the same with slight variations. The loading area of the beams A_L are given by

$$A_L = hL \tag{4-25}$$

where h = the full height of a single block and L = the length of the member. The total force of the pressure loading F_P is given by

$$F_P = PhL \tag{4-26}$$

where P = the peak pressure resulting from the blast loading. When the pressure is applied to the loading area, the shear force at the supports V_u become

$$V_u = \frac{PhL}{2} = \frac{PA_L}{2} \tag{4-27}$$

The reaction can quickly be determined to be the shear forces acting at the supports. Therefore, the shear force on the each beam model depends on the height of the wall, the length of the wall, and the peak pressure on the wall.

4.4 Resistance Equation Derivation

The next step is to develop each beam's nominal resistance. These resistance equations will be based on mechanics and design standards.

4.4.1 Development of Resistance Equation

In cementitious materials there are three ways that shear force is resisted. These are the strength attributed to masonry, the strength attributed to gravity loading, and the strength attributed to steel. Therefore, the nominal shear V_n resistance is given by

$$V_n = V_m + V_p + V_s \tag{4-28}$$

where V_m = the shear resistance of the masonry, V_p = the shear resistance of the overburden, and V_s = the shear resistance of the steel. Since breaching will occur at sections of lowest resistance, the wall will breach at cells without grout. Therefore, the breaching shear is not affected by the steel reinforcement and is negligible giving

$$Vs = 0 \tag{4-29}$$

Also, the effects of axial overburden may contribute to the breaching shear. However, the resistance mechanism does not occur where there is any significant frictional force because the breaching occurs on a vertical axis, and the nominal shear resistance of the axial loading is

$$V_p = 0 \tag{4-30}$$

This leaves only the shear resistance contributed by the masonry. In the masonry design codes, the masonry shear resistance is given by a variation of

$$V_n = V_m = CA_n f_{vm} \tag{4-31}$$

where C = coefficient to account for safety factors or dynamic increase factors or to fit data, A_n = the nominal resisting area, and f_{vm} = the ultimate shear stress of masonry. The equation can be further simplified to

$$V_n = Chtf_{vm} \tag{4-32}$$

This equation was derived for the face shell beam. The equation for the between grout cells beam is

$$V_n = 2Chtf_{vm} \tag{4-33}$$

4.5 Comparison between FEM Stress and Analytical Stress

In order to account for the differences between the actual breaching shear stress and the FEM shear stress, an equation for the shear stress on the face shell of the CMU needs to be found. For rectangular sections, the stress caused by shear loading τ is

$$\tau = \frac{V}{A} \tag{4-34}$$

where Q = first moment area and V = shear force at the section of interest.

4.5.1 Face Shell Beam Comparison

Even though the model assumes beam action, the breaching shear develops in a punching shear pattern. Therefore, the shear stress is given by

$$\tau = \frac{PhL}{2ht} = \frac{PL}{2t} \tag{4-34}$$

The shear stress resulting from this equation is compared to shear stresses collected on a single block subjected to varying peak pressure with 0.25 in. by 0.25 in. by 0.25 in. element size with fully-integrated element formulation. Table 4.4 gives a comparison of finite element results compared to calculated value only for a face shell beam. In this table, there are also values for the finite element stresses divided by the calculated values. Figure 4.12 shows the last three columns of Table 4.4 versus the peak pressure.

Table 4.4. Shear stress comparison for single block beam

Pressure (psi)	FEM Stress (psi)	Calc. Stress (psi)	FEM/Calc.
5	42	13	3.3
10	83	25	3.3
15	127	38	3.4
20	173	51	3.4
25	220	63	3.5
30	267	76	3.5
35	314	88	3.6
40	361	101	3.6
45	403	114	3.5
50	439	126	3.5

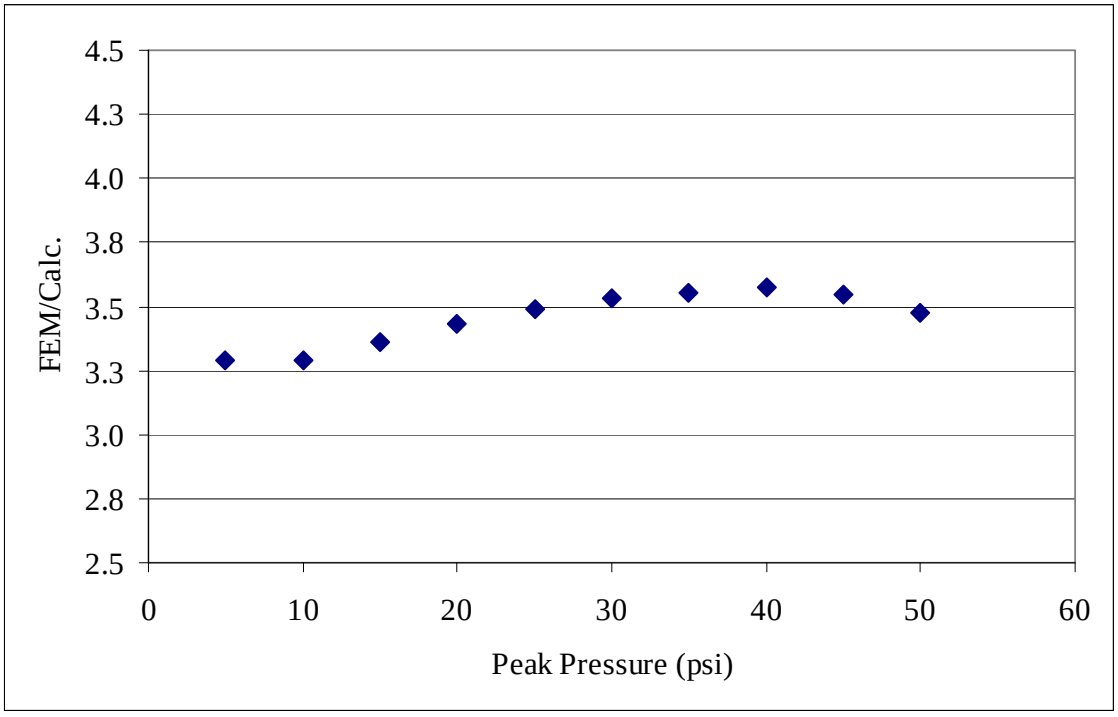

Figure 4.12. Comparison between FEM and calculated shear stress for face shell beam

In looking at the data, the comparison shows that ratio of FEM to calculated stress has some variation; however, the variation is small with a standard deviation of 0.11 and average of 3.5. There are several reasons the FEM and analytical model do not match more closely; these are discussed in a later section.

4.5.2 Between Grout Cells Beam Comparison

The BGC beam has similar mechanics as the face shell beam. The difference is in the cross section. The shear stress is given by

$$\tau = \frac{PhL}{2ht} = \frac{PL}{2t} \tag{4-34}$$

The comparison of the FEM and the calculated shear stress is seen in Table 4.5. Figure 4.13 show a graphical version of the data.

Table 4.5. Shear stress comparison for BGC beam

	Shear Stresses (psi)						FE Stresses /Calc. Stresses		
Pres.	**5x5**	**Calc.**	**10x3**	**Calc.**	**3x10**	**Calc.**	**5x5**	**10x3**	**3x10**
5	86.4	63.0	72.2	143.0	73.9	31.0	1.37	0.50	2.38
10	124	126.0	106.8	286.0	108.8	62.0	0.98	0.37	1.75
15	134.5	189.0	129.7	429.0	122.1	93.0	0.71	0.30	1.31
20	143.7	252.0	146.5	572.0	141.6	124.0	0.57	0.26	1.14
25	167	315.0	155.5	715.0	161.5	155.0	0.53	0.22	1.04
30	194.4	378.0	201.4	858.0	206.1	186.0	0.51	0.23	1.11
35	235.5	441.0	236.9	1001.0	228.2	217.0	0.53	0.24	1.05
40	267.3	504.0	262.3	1144.0	248.4	248.0	0.53	0.23	1.00
45	277.9	567.0	280.1	1287.0	264.4	279.0	0.49	0.22	0.95
50	280.1	630.0	268.4	1430.0	261.8	310.0	0.44	0.19	0.84

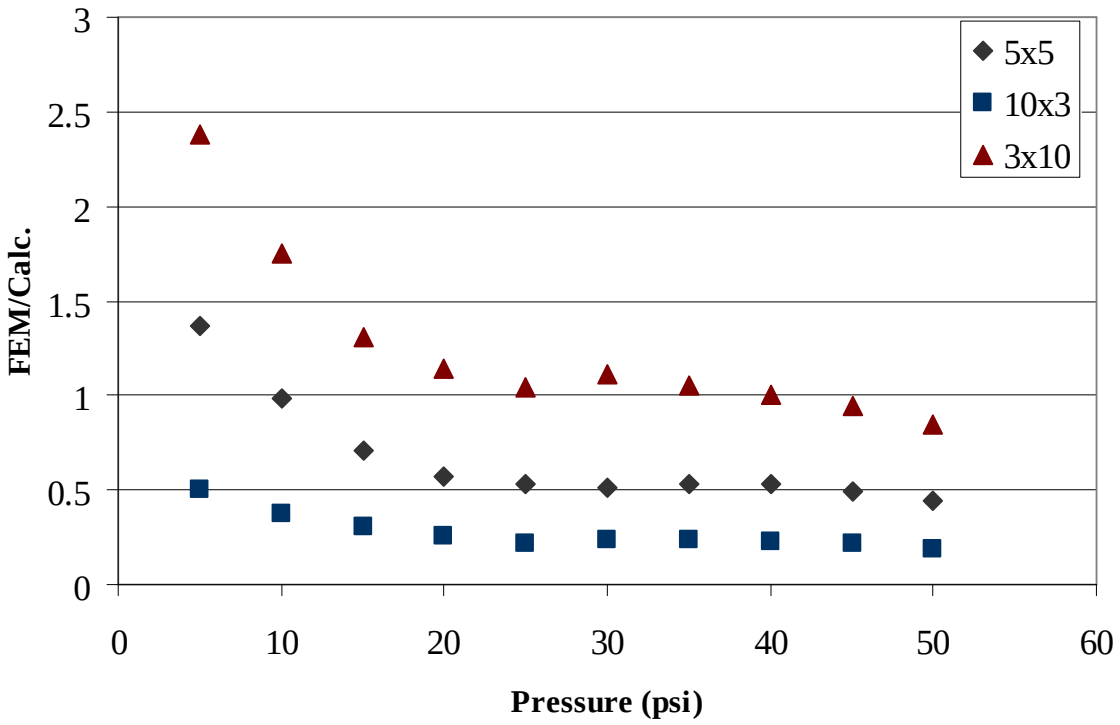

Figure 4.13. Comparison of FEM vs. calculated shear stress for between grouted cell beam

The figure shows that the comparison is length dependent. It shows that the smaller the distance between the grout columns the greater the ratio of FEM to calculated shear stress. Figure 4.14 shows a graph of correction factor versus length for the geometry data acquired on grouted models.

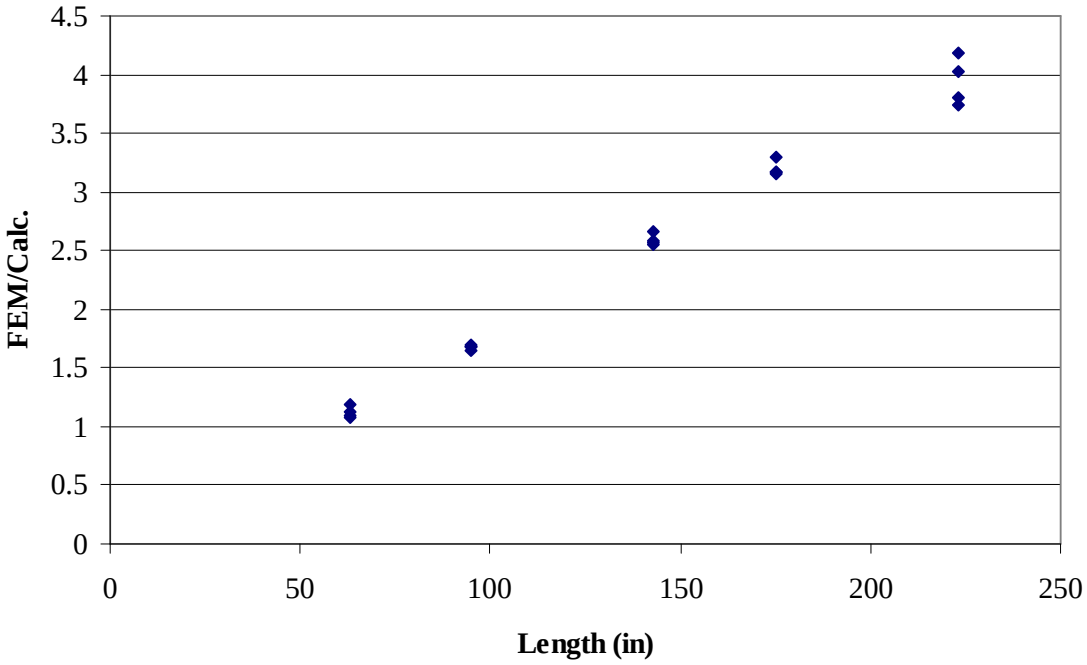

Figure 4.14. Ratio of FEM to calculated shear stress vs. length

The figure shows that the ratio is linear for length. This is evident looking at the Equation 4-34 and the data on the geometry suitability study; since the values for the suitability were almost constant, the correction factor differed only by the length.

4.5.3 Differences between FEM and Analytical Shear Stress

In both models, there are major differences between the shear stress calculated by FEM and calculated using beam models. The differences exist for a few different reasons. These reasons are (1) a lack of testing data on shear stresses in full-scale blast testing, (2) a lack of understanding of the mechanics in the breaching, (3) a lack of understanding of the concrete model used in FEM, (4) a lack of understanding in how to properly model mortar-block bond in highly dynamic loading, and (5) a lack of static testing to validate FEM modeling. More research is needed to understand most of the

reasons the FEM and analytical models are not the same. However, there is a lack of testing data on shear stresses during blast loading which is almost impossible to obtain. The rest can be found using static testing or dynamic testing.

4.6 Breaching Shear Design Equation

Finally, the shear strength required by both models is

$$V_u = \frac{PL}{2} \tag{4-43}$$

The shear resistance is given by

$$V_n = Ctf_{vm} \tag{4-44}$$

In order to prevent breaching, the nominal strength needs to be equal to or greater that the ultimate shear demand; this is given by

$$V_u \leq V_{\mathrm{n}} \tag{4-45}$$

or

$$\frac{PL}{2} \leq Ctf_{vm} \tag{4-46}$$

Solving for pressure results in

$$P \leq \frac{2Ctf_{vm}}{L} \tag{4-47}$$

Using ACI 530.1 (ACI, 2011) and assuming that most building use type N mortar, the minimum compressive strength of the concrete block f'_b is 2150 psi for a masonry assemblage compressive strength f'_m of 1500 psi with Type N mortar. ACI 318 (ACI, 2011) gives the ultimate shear stress of concrete by

$$f_{vm} = 4/3\lambda\sqrt{f'_b} = 46\text{psi} \tag{4-49}$$

where λ = a correction factor for lightweight concrete (0.75). The shear stress strength is for plain concrete instead of masonry; this is because the masonry shear stress is built around masonry-mortar bond and frictional sliding, not on the shear strength of concrete. Plugging Equation 4-38 into Equation 4-37 and solving for pressure gives

$$P \le \frac{2 \times Ct \times 46\text{psi}}{L} \tag{4-50}$$

With Equation 4-39, a maximum pressure can be found for each block or section. Table 4.6 shows the maximum pressure for a single block beam; Table 4.5 shows the maximum for the BGC beams with length being based on maximum steel reinforcement spacing. For now since the stress gradient in the FEM has not been calibrated with data from full-scale testing stress data, the correction factor is taken as 1 for now.

Table 4.6. Maximum pressure for single block beam

Single Block Beam		
L (in)	*t* (in)	*P* (psi)
6.0625	1.25	19

Table 4.7. Maximum pressure for BGC beams

Between Grout Cells Beam			
Nominal Block Size	*L* (in)	*t* (in)	*P* (psi)
6-in	28	2.5	8.3
8-in	40	2.5	5.8
10-in	52	2.5	4.4
12-in	64	2.5	3.6
14-in	76	2.5	3.0
16-in	88	2.5	2.6

Only the single block beam provides a pressure that is independent of length between grout cells, geometry of the wall, and material properties of the blocks which is seen in

the suitability study; the BGC beam is not independent of these. In addition, using the full-scale tests the single block beam pressure matches closer to the results in the tests. Test 1 did breach but not to fully indicating the pressure was around the cutoff between breaching and flexure. Test 2 and Test 3 had a more severe breaching response, and the peak pressure was much higher than the single block beam and BGC beam pressures. Therefore, all masonry walls must be fully grouted if a pressure exceeding 19 psi is expected. Using UFC 3-340-02's Figure 2-7, a minimum scaled standoff for a free air blast at sea level was obtained. This cutoff scaled standoff is 10 $lb/ft^{1/3}$.

CHAPTER 5

CONCLUSION AND RECOMMENDATIONS

5.1 Conclusions

A full-scale dynamic test was conducted on several partially grouted walls. These walls were made of either 6-in. or 8-in. CMU blocks and either had a veneer or not. These walls failed in a breaching pattern. A finite element model was created to analyze the failure of the breaching phenomenon.

The finite element methodology involved a number of steps: (1) creation of a FEM representing a partially grouted, reinforced wall CMU wall, (2) validation of the FEM against the full-scale dynamic test, and (3) a brief parametric study.

With the FEM analysis, the dynamics of CMU breaching was explored, and the system was found to be quasi-static. The parametric study supported all the assumptions made in finding the natural frequency of the system; it also showed that the shear stresses were independent of wall geometry, material properties, grouting geometry, and loading shape. It was found that the shear stresses were only dependent on the peak pressure and were only based on a single cell of a single block.

Finally, two engineering-level design equations were created to find the shear resistance provided a wall. It was determined that the shear resistance is only provided by the masonry without any addition due to overburden or steel. A design resistance

versus design load required was developed. The design ratio was found to independent of wall geometry and only dependent on the block's clear span between webs, block's thickness of faceshell, peak pressure of the blast, and the block shear strength.

5.2 Recommendations

It is recommended that all walls that are expected to have pressures greater than 19 psi or a scaled standoff less than 10 $lb/ft^{1/3}$ need to be fully grouted. In addition, it is recommended that more full-scale static and dynamic testing be used to better understand CMU response; this testing should focus on how to establish a better understanding of the breaching. This dynamic testing should look into both the flexural capacity and shear capacity of the wall with stress monitoring.

References

American Concrete Institute (ACI) (2008). Building Code Requirements for Structural Concrete and Commentary, ACI 318-08, Farmington Hills, MI.

ACI (2011). Building Code Requirements and Specification for Masonry Structures, ACI 530-11, Farmington Hills, MI.

Atkinson R. H., Amadei, B. P., Saeb, S., and Sture, S. (1989). "Response of masonry bed joints in direct shear." Journal of Structural Engineering, vol. 115 no. 9, pp. 2276-2296.

Biggs, J. M. (1964). "Introduction to Structural Dynamics," McGraw-Hill, New York.

Browning IV, R. S. (2008). Resistance of multi-wythe insulated masonry subjected to impulse loads." M.S. thesis, Auburn University, Auburn, AL.

Burnett, S., Gilbert, M., Molyneaus, T., Beattie, G., and Hobbs, B. (2006). "The performance of unreinforced masonry walls subjected to low velocity: finite element analysis." International Journal of Impact Engineering, vol. 34, pp. 1433-1450.

Davidson, J. S., Moradi, L., and Dinan, R. J. (2006). "Selection of a material model for simulating concrete masonry walls subjected to blast." AFRL-ML-TY-TR-2006-4521.

Davidson, J. S., Hoemann, J. M., Salim, H. H., and Shull, J. S. (2010). "Full-scale experimental evaluation of partially grouted, minimally reinforced CMU walls against blast demands." AFRL-RX-TY-TR-2010-00.

Dennis, S. T., Baylot, J. T., and Woodson, S. C. (2002). "Response of 1/4-scale concrete masonry unit walls to blast." Journal of Engineering Mechanics, vol. 128, no. 2, pp. 134-142.

Department of Defense (2008). "Structures to Resist the Effects of Accidental Explosions," UFC 3-340-02, Whole Building Design Guide, http://dod.wbdg.org/ (accessed Feb. 2011).

Drysdale, R. G., and Hamid, A. A. (2008). *Masonry Structures Behavior and Design*, 2nd Ed., The Masonry Society, Boulder, CO.

Eamon, C. D., Baylot, J. T., and O'Daniel, J. L. (2004). "Modeling concrete masonry walls subjected to explosive load." Journal of Engineering Mechanics, vol. 130, no. 9, pp. 1098-1106.

Gilbert, M., Hobbs, B., and Molyneaux, T. C. K. (2002). "The performance of unreinforced masonry walls subjected to low-velocity impacts: mechanism analysis." International Journal of Impact Engineering, vol. 27, pp. 253-275.

Hamid, A. A. and Drysdale, R. G. (1988). "Flexural tensile strength of concrete block masonry." Journal of Structural Engineering. vol. 114, no. 1, pp. 50-66.

Krauthammer, T. (2008). "Pressure-impulse diagrams and their applications." *Modern Protective Structures*. CRC Press, Boca Raton, FL, pp. 325-371.

Livermore Software Technology Corporation (LSTC) (2009). LS-DYNA Keyword User's Manual.

Magallanes, J. M., Wu, Y., Malvar, L. J., and Crawford, J. E. (2010). "Recent Improvements to release III of the K&C concrete model." *11th International LS-DYNA Users Conference*. Livermore Software Technology Corporation, Livermore, CA, 3-37 - 3-48.

Martini, K. (1996). "Research in the out-of-plane behavior of unreinforced masonry." Ancient Reconstruction of the Pompeii Forum, School of Architecture, University of Virginia.

Martini, K. (1998). "Finite element studies in the two-way out-of-plane failure of unreinforced masonry." Ancient Reconstruction of the Pompeii Forum, School of Architecture, University of Virginia.

Moradi, L. G., Davidson, J. S., and Dinan, R. J. (2008). "Resistance of membrane retrofit concrete masonry walls to lateral pressure." Journal of Performance of Constructed Facilities, vol. 22, no. 3, pp. 131-142.

Psilla, N. and Tassios, T. (2009). "Design of reinforced masonry walls under monotonic and cyclic loading." Engineering Structures, vol. 31, pp. 935-945.

Salim H., Saucier A., Bell B, Hoemann J., Bewick B, Davidson J., Shull J. "Experimental Evaluation of Full-Scale NCMA Walls Under Uniform Pressure Using Vacuum," draft report submitted to the Air Force Research Laboratory, July 2011.

Schwer, L. (2001) Draft, "Laboratory Tests for Characterizing Geomaterials" Livermore Software Technology Corporation, Livermore, California.

Schwer, L. (2005). "Simplified concrete modeling with Mat_Concrete_Damage_Rel3." JRI LS-DYNA User Week. LSTC, Livermore, CA.

Smith, P. and Cormie, D. (2009) "Structural response to blast loading." *Blast Effects on Buildings*. D. Cormie, G. Mays, and P. Smith, eds., Thomas Telford Limited, London, UK, pp. 80-102

Sudame, S. (2004). "Development of computational models and input sensitive study of polymer reinforced concrete masonry walls subjected to blast." M.S. thesis, University of Alabama at Birmingham, Birmingham, AL.

APPENDIX

LS-DYNA INPUT

```
*KEYWORD
*TITLE
*CONTROL_TERMINATION
$#              endtim    endcyc    dtmin     endeng    endmas
                0.01      0         0         0         0
*CONTROL_TIMESTEP
$#              dtinit    tssfac    isdo      tslimt    dt2ms     lctm      erode     ms1st
                0         0.5       0         0         0         0         0         0
$#              dt2msf    dt2mslc   imscl
                0         0         0
*DATABASE_ELOUT
$#              dt        binary    lcur      ioopt
                2.50E-05  3         0         1
*DATABASE_BINARY_D3PLOT
$#              dt        lcdt      beam      npltc     psetid
                5.00E-04  0         0         0         0
$#              ioopt
                0
*DATABASE_HISTORY_SOLID_SET
$#              id1       id2       id3       id4       id5       id6       id7       id8
                1         2         3         0         0         0         0         0
*BOUNDARY_SPC_SET
$#              nsid      cid       dofx      dofy      dofz      dofrx     dofry     dofrz
                1         0         1         1         1         1         1         1
*SET_NODE_LIST_TITLE
NODESET(SPC) 1
$#              sid       da1       da2       da3       da4
                1         0         0         0         0
$#              nid1      nid2      nid3      nid4      nid5      nid6      nid7      nid8
                82645     82646     82647     82648     82649     82650     82651     82652
                82653     82654     82655     82656     82657     82658     82659     82660
                82661     82662     82663     82664     82665     82666     82667     82668
                .
                .
                .
                82621     82622     82623     82624     82625     82626     82627     82628
                82629     82630     82631     82632     82633     82634     82635     82636
```

```
                82637   82638   82639   82640   82641   82642   82643   82644
                .
                .
                .
*LOAD_BODY_Z
                lcid    sf      lciddr  xc      yc      zc      cid
                1       1       0       0       0       0       0
*LOAD_SEGMENT_SET_ID
$#              id      heading
                1
$#              ssid    lcid    sf      at
                101     2       1       0
*CONTACT_AUTOMATIC_SURFACE_TO_SURFACE_ID
$#              cid     title
                1
$#              ssid    msid    sstyp   mstyp   sboxid  mboxid  spr     mpr
                2       1       0       0       0       0       0       0
$#              fs      fd      dc      vc      vdc     penchk  bt      dt
                0       0       0       0       0       0       0.0001.0000E+20
$#              sfs     sfm     sst     mst     sfst    sfmt    fsf     vsf
                1       1       0       0       1       1       1       1
*SET_SEGMENT_TITLE
BCB
$#              sid     da1     da2     da3     da4
                2       0       0       0       0
$#              n1      n2      n3      n4      a1      a2      a3      a4
                61777   61810   61811   61778   0       0       0       0
                49784   49817   49818   49785   0       0       0       0
                3831    3870    3871    3832    0       0       0       0
                .
                .
                .
                2623    2632    3551    3512    0       0       0       0
                3830    3869    3870    3831    0       0       0       0
                2631    2640    2641    2632    0       0       0       0
                .
                .
                .
*PART
$#              title
CMU
$#              pid     secid   mid     eosid   hgid    grav    adpopt  tmid
                1       1       1       0       0       0       0       0
*SECTION_SOLID
$#              secid   elform  aet
                1       1       0
*MAT_BRITTLE_DAMAGE_TITLE
CMU
```

$#	mid	ro	e	pr	tlimit	slimit	ftough	sreten
	1	1.79E-04	1.80E+06	0.2	224.7	67.08	0.8	0.03
$#	visc	fra_rf	e_rf	ys_rf	eh_rf	fs_rf	sigy	
	104	0	0	0	0	0	0	
	.							
	.							
	.							

*MAT_BRITTLE_DAMAGE_TITLE
Mortar

$#	mid	ro	e	pr	tlimit	slimit	ftough	sreten
	2	1.87E-04	1.80E+06	0.15	224.7	67.08	0.8	0.03
$#	visc	fra_rf	e_rf	ys_rf	eh_rf	fs_rf	sigy	
	104	0	0	0	0	0	0	

*PART

$#	title							
HJ								
$#	pid	secid	mid	eosid	hgid	grav	adpopt	tmid
	202	1	2	0	0	0	0	0
	.							
	.							
	.							

*PART

$#	title							
Boundary								
$#	pid	secid	mid	eosid	hgid	grav	adpopt	tmid
	501	1	5	0	0	0	0	0

*MAT_RIGID_TITLE
Boundary

$#	mid	ro	e	pr	n	couple	m	alias
	5	7.34E-04	2.90E+07	0.3	0	0	0	
$#	cmo	con1	con2					
	0	0	0					
$#	lco	or	a1	a2	a3	v1	v2	v3
	0	0	0	0	0	0		
	.							
	.							
	.							

*MAT_BRITTLE_DAMAGE_TITLE
Grout

$#	mid	ro	e	pr	tlimit	slimit	ftough	sreten
	3	1.87E-04	2.00E+06	0.2	317.8	94.87	0.8	0.03
$#	visc	fra_rf	e_rf	ys_rf	eh_rf	fs_rf	sigy	
	104	0	0	0	0	0	0	

*MAT_PLASTIC_KINEMATIC_TITLE
Rebar

$#	mid	ro	e	pr	sigy	etan	beta
	4	7.34E-04	2.90E+07	0.3	60000	0	0
$#	src	srp	fs	vp			

```
                0       0       0       0
                .
                .
                .
*DEFINE_CURVE_TITLE
Triangular
$#              lcid    sidr    sfa     sfo     offa    offo    dattyp
                1       0       1       1       0       0       0
$#              a1      o1
                0       0
                0.001   0
                0.00101 50
                0.0061  0
                0.01    0
                .
                .
                .
*SET_SEGMENT_TITLE
Blast
$#              sid     da1     da2     da3     da4
                101     0       0       0       0
$#              n1      n2      n3      n4      a1      a2      a3      a4
                51733   51766   51765   51732   0       0       0       0
                48510   48543   48542   48509   0       0       0       0
                18064   18076   18242   18209   0       0       0       0
                .
                .
                .
                5097    5145    5144    5096    0       0       0       0
                2050    2059    2058    2049    0       0       0       0
                268     307     306     267     0       0       0       0
*ELEMENT_SOLID
$#              eid     pid     n1      n2      n3      n4      n5      n6      n7      n8
                1       1       1       2       5       4       10      11      14      13
                2       1       2       3       6       5       11      12      15      14
                3       1       4       5       8       7       13      14      17      16
                .
                .
                .
                10138   502     82743   82744   82846   82845   82947   82948   83050   83049
                10139   502     82744   82745   82847   82846   82948   82949   83051   83050
                10140   502     82745   82746   82848   82847   82949   82950   83052   83051
*NODE
$#              nid     x       y       z       tc      rc
                1       0       0       0       0       0
                2       0.5     0       0       0       0
                3       1       0       0       0       0
                .
```

.
.

83050	48	8.13	23.625	0	0
83051	48.5	8.13	23.625	0	0
83052	49	8.13	23.625	0	0